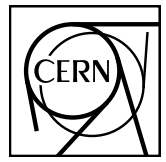


EUROPEAN ORGANIZATION FOR NUCLEAR RESEARCH



June 15, 2017

D-hadron correlations in p-Pb collisions at $\sqrt{s_{\text{NN}}} = 5.02 \text{ TeV}$

F. Colamaria, S. Kumar, M. Mazzilli

Abstract

In this note, we present the analysis of azimuthal correlations of D mesons and primary charged particles performed in the ALICE central barrel in p-Pb collisions at $\sqrt{s_{\text{NN}}} = 5.02 \text{ TeV}$, from 2016 data taking. The analysis is performed in an extended p_T range and with additional observables with respect to p-Pb 2013 data analysis. After a description of the analysis strategy, corrections and systematic uncertainties, the results obtained for prompt D^0 , D^{*+} and D^+ mesons in different ranges of transverse momentum of the D meson and of the associated particles are presented. The results are then compared to Monte Carlo models and also with published 2013 p-Pb analysis results for the common p_T ranges.

1 **Contents**

2	1	Introduction and Motivation	3
3	2	Data/Monte Carlo samples and event selection	4
4	3	Analysis strategy	7
5	3.1	Mass plots and cut optimization	10
6	3.2	Code used for the analysis	14
7	3.3	Further details on corrections	14
8	3.3.1	Event Mixing	14
9	3.3.2	Tracking and D-meson trigger efficiency	18
10	3.3.3	Correction for bias on B to D decay topologies	23
11	3.3.4	Secondary track contamination	28
12	3.3.5	Beauty feed-down	32
13	4	Systematic uncertainties on $\Delta\phi$ correlation distributions	36
14	4.1	Uncertainty on S and B extraction	36
15	4.2	Uncertainty on background correlation shape	36
16	4.3	Uncertainty on D-meson cut stability	40
17	4.4	Uncertainty on tracking efficiency evaluation	40
18	4.5	Uncertainty on secondary particle contamination	44
19	4.6	Uncertainty on feed-down subtraction	45
20	4.7	Uncertainty on correction for the bias on B to D decay topologies	49
21	4.8	Summary table	50
22	5	Results	51
23	5.1	Comparing the three D meson correlation distributions	51
24	5.2	Average of D^0 , D^+ and D^{*+} results	64
25	5.3	Fit observable p_T trends and uncertainties	67
26	5.3.1	Results for near-side yield and width, away-side yield and width, and baseline .	68
27	5.4	Comparison of 2016 p-Pb and 2013 p-Pb results	84
28	5.5	Comparison of 2016 p-Pb and 2010 pp results	84
29	5.6	Comparison of 2016 p-Pb and model expectations	84
30	5.7	Planned results for SQM approvals	84

³¹	6	Bibliography	95
---------------	----------	---------------------	-----------

32 1 Introduction and Motivation

33 The study of the azimuthal correlations of heavy-flavour particles and charged particles at the LHC
 34 energies provides a way to characterize charm production and fragmentation processes in pp collisions.
 35 The measurement also provide a way to probe our understanding of QCD in the perturbative regime,
 36 accessible in a large kinematic range given the large mass of heavy quarks. Flavour conservation in
 37 QCD implies that charm quarks are always produced as pairs of quarks and anti-quarks. The azimuthal
 38 correlations obtained using a meson carrying a heavy quark as trigger particle with the other charged
 39 particles in the same event give the possibility to study the underlying charm production mechanism in
 40 detail. In particular, prompt charm quark-antiquark pair production is back to back in azimuth at first
 41 order in leading-order perturbative-QCD (pQCD). If an hadron from the quark hadronization is taken as
 42 trigger particle, a near-side (at $\Delta\phi = 0$) and an away-side (at $\Delta\phi = \pi$) peak would appear in the azimuthal
 43 correlation distributions, coming from the fragmentation of the quark pair. Heavy quarks produced from
 44 the splitting of a massless gluon can be rather collimated and may generate sprays of hadrons at small
 45 $\Delta\phi$. Finally, for hard-scattering topologies classified as “flavour-excitation”, a charm quark undergoes a
 46 hard interaction from an initial splitting ($g \rightarrow c\bar{c}$), leading to a big separation in rapidity of the hadrons
 47 originating from the antiquark (quark) with respect to the trigger D meson and contribute to a rather flat
 48 term to the $\Delta\phi$ -correlation distribution.

49 Heavy-flavour correlation studies in more complex collision systems, like Pb-Pb, play a crucial role in
 50 studying the modification of the fragmentation of charmed jets due to in-medium (or cold nuclear matter,
 51 in case of p-Pb collisions) effects, in a similar way as it was done for di-hadron correlation studies in
 52 heavy-ion collisions (see for example). Furthermore, the recent observation of long range correlations
 53 in p-Pb for light flavour hadrons ([3], [4]) and for heavy-flavour decay electrons (ALICE preliminary re-
 54 sults) points to possible collective effects or effects originating from gluon saturation in the initial state.
 55 More information could be extracted by the eventual observation of the same effect with D mesons.

56

57 In the following note, we first describe the analysis strategy for the p-Pb 2016 data sample in all its steps,
 58 followed by the list of analysis corrections and the estimation of systematic uncertainties. Finally the
 59 results of $\Delta\phi$ correlations, and quantitative observable extracted to fits to those distributions, obtained for
 60 prompt D^0 , D^+ and D^{*+} in different ranges of transverse momentum for the D-meson (trigger particle)
 61 and the associated particles are presented.

62 The extension of the momentum ranges (both for D mesons and associated particles) with respect to the
 63 2013 p-Pb dataset, as well as the improved precision in the common ranges allow a more thorough inves-
 64 tigation of the charm quark fragmentation properties (multiplicity of tracks as a function of momentum,
 65 geometrical profile of charm jets, p_T distribution of the tracks inside the jet). This can also allow us to
 66 put better constraints on the description of charm fragmentation and charm jet properties provided by
 67 models. In addition, the new measurements can be used as solid and precise references in view of an
 68 analysis on a Pb-Pb sample at the same energy (hopefully already in 2018 data taking, otherwise after
 69 the ALICE upgrade).

70 2 Data/Monte Carlo samples and event selection

71 The data samples used for the analyses were the FAST and CENT_woSDD samples from periods LHC16q
 72 and LHC16t (AOD samples). The reason of choosing different types of data samples is explained later
 73 on, in this section. It was verified, by looking at D-meson and associated charged track η and φ distribu-
 74 tions, and at the mixed-event correlation distributions for each subsamples, that no visible differences is
 75 present for the four periods, hence it was possible to perform the analysis directly on the merged samples
 76 without any bias.

77 The Monte Carlo productions adopted for this study were:

- 78 1. LHC17d2a_fast_new, a HIJING production with enrichment of heavy quarks (charm and beauty)
 79 and their decay products in each of the event, performed by PYTHIA6 with Perugia2011 tune,
 80 and with forced hadronic decays of the charmed hadrons. This production was used for D-meson
 81 efficiency evaluation, purity estimation and Monte Carlo closure test.
- 82 2. LHC17f2b_cent_woSDD and LHC17f2b_fast, minimum-bias samples produced with DPMJET
 83 generator, are used for the evaluation of the tracking efficiencies.

84 Table 1 shows the list of runs used for the analysis, for each of the data taking periods, and of the Monte
 85 Carlo productions used to evaluate the corrections:

86 The trigger mask request for the event selection is kINT7. Only events with a reconstructed primary
 87 vertex within 10 cm from the centre of the detector along the beam line are considered. This choice max-
 88 imises the detector coverage of the selected events, considering the longitudinal size of the interaction
 89 region, and the detector pseudorapidity acceptances. In the analysis, the center-of-mass reference frame
 90 of the nucleon-nucleon collision is shifted in rapidity by $y_{NN} = 0.465$ in the proton direction with re-
 91 spect to the laboratory frame, due to the different per-nucleon energies of the proton and the lead beams.
 92 Beam-gas events are removed by offline selections based on the timing information provided by the V0
 93 and the Zero Degree Calorimeters, and the correlation between the number of hits and track segments in
 94 the SPD detector. This is automatically performed in the Physic Selection, a positive outcome of which
 95 is required during our event selection. The pile-up cuts for out-of-bunch pile-up protection are also in-
 96 volved when calling the Physics Selection task. The minimum-bias trigger efficiency is 100% for events
 97 with D mesons with $p_T > 1 \text{ GeV}/c$. For the analyzed data samples, the probability of pile-up from col-
 98 lisions in the same bunch crossing is below 2% per triggered event (in most of the runs, well below 1%).
 99 Events in which more than one primary interaction vertex is reconstructed with the SPD detector (with
 100 minimum of 5 contributors, and a z distance greater than 0.8 cm) are rejected, which effectively removes
 101 the impact of in-bunch pile-up events on the analysis. Out-of-bunch tracks are effectively rejected by the
 102 Physics Selection pile-up cuts, and also by the request of at least one point in the SPD, which has a very
 103 limited time acquisition window (300 ns). Indeed, though the default associated track selection requires
 104 a minimum of 2 points in the ITS, as it will be shown later on full compatibility of the corrected results
 105 with 2 and 3 minimum ITS clusters are obtained. For FAST and CENT_woSDD samples, the latter case
 106 indirectly forces the presence of a point in the SPD.

107 Since data collected during p-Pb 2016 data taking are distinguished into two categories - one including
 108 SDD detector (CENT_wSDD sample) and the second one without the SDD in the reconstruction, or
 109 in the acquisition (CENT_woSDD and FAST samples, respectively), a study of performance of the D-
 110 hadron correlation analysis with respect to the data samples employed has been carried out for D^{*+} and
 111 D^+ mesons (more sensitive to the presence of the SDD w.r.t. the D^0 , due to their reconstruction from
 112 three decay tracks).

113 For this reason, the D-hadron correlation distribution has been compared on LHC16q_pass1_CENT_wSDD
 114 and LHC16q_pass1_CENT_woSDD and the relative statistical uncertainty has been estimated in order to

Type	Production	Run list	nEvents
Monte-Carlo	LHC17d2a_fast_new (c/b enriched), LHC17f2b_fast (MB), LHC17f2b_cent_woSDD (MB)	267166, 267165, 267164, 267163, 265525, 265521, 265501, 265500, 265499, 265435, 265427, 265426, 265425, 265424, 265422, 265421, 265420, 265419, 265388, 265387, 265385, 265384, 265383, 265381, 265378, 265377, 265344, 265343, 265342, 265339, 265338, 265336, 265335, 265334, 265332, 265309 = [36 runs]	50M
Data	LHC16q, pass1_CENT_woSDD	265525, 265521, 265501, 265500, 265499, 265435, 265427, 265426, 265425, 265424, 265422, 265421, 265420, 265419, 265388, 265387, 265385, 265384, 265383, 265381, 265378, 265377, 265344, 265343, 265342, 265339, 265338, 265336, 265335, 265334, 265332, 265309 = [32 runs]	261M total
	LHC16q, pass1_FAST	265525, 265521, 265501, 265500, 265499, 265435, 265427, 265426, 265425, 265424, 265422, 265421, 265420, 265419, 265388, 265387, 265385, 265384, 265383, 265381, 265378, 265377, 265344, 265343, 265342, 265339, 265338, 265336, 265335, 265334, 265332, 265309 = [32 runs]	260M
	LHC16t, pass1_CENT_woSDD	267166, 267165, 267164, 267163 = [4 runs]	40M
	LHC16t, pass1_FAST	267166, 267165, 267164, 267163 = [4 runs]	41M

Table 1: Data Set and Run list

understand if it was better to perform the analysis separately on the two data sample, applying in this case different corrections, or not. In particular, it was crucial for the correlation analysis involving the D^{*+} meson because the track reconstruction efficiency of the soft pion is $\approx 10\%$ higher employing also the SDD information. Figure 1 shows the normalized azimuthal correlation distribution for low, mid and high p_T for D^{*+} meson. Blue points are referred to the woSDD sample while red points represents wSDD data. Figure 2 shows the relative statistical uncertainty extracted from the azimuthal correlation distributions for the D^{*+} in different kinematic ranges.

It can be observed that the data sample that includes the SDD information is characterized by $\approx 10 - 15\%$ more statistics in each p_T ranges analyzed. This difference is related to the larger efficiency in track reconstruction with the wSDD sample - a larger number of tracks survives to the selection request of 3 points in the ITS, which is part of the selection requests applied on the previous D-h analysis.

As a result, the wSDD sample is also affected by a slightly lower relative statistical uncertainty (about 12-15%) due to several reasons: the larger tracking efficiency, the larger number of signal entries in the invariant mass distributions (again an effect of the larger tracking efficiency) and a slight increase of S/B, which reflects in a slight decrease of uncertainty from the sideband subtraction. It has also to be considered that, on the full sample including also the FAST cluster, the increase in performance would be further reduced. The overall statistical uncertainty difference resulting from the comparison is not

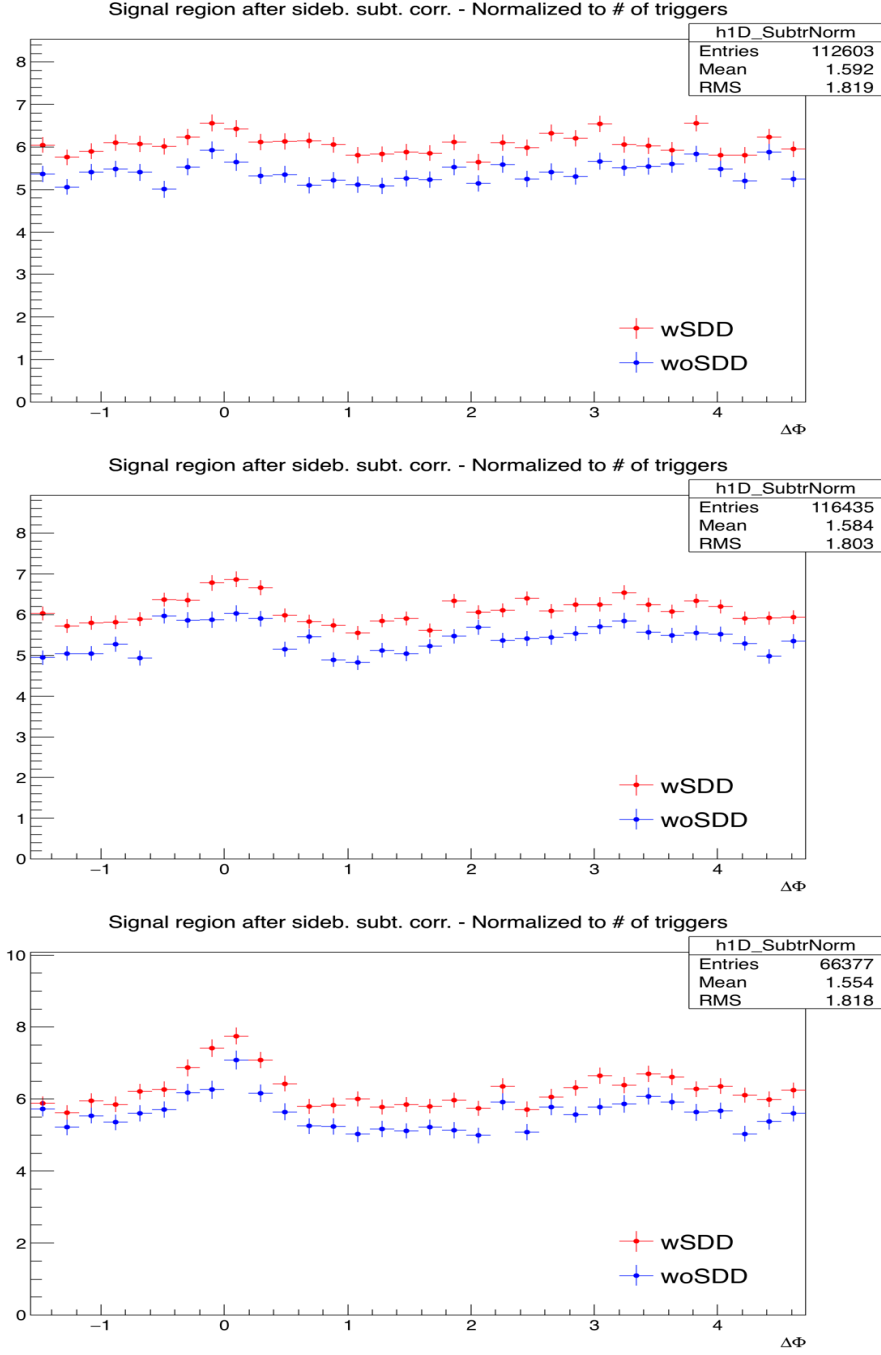


Figure 1: Normalized azimuthal correlation distribution of D^{*+} for low p_T ($3 < p_T(D^{*+}) < 5 \text{ GeV}/c$) on the top panel, mid p_T ($5 < p_T(D^{*+}) < 8 \text{ GeV}/c$) on the middle panel and high p_T ($8 < p_T(D^{*+}) < 16 \text{ GeV}/c$) on the bottom panel with a p_T threshold for associated tracks of $p_T(\text{assoc}) > 0.3 \text{ GeV}/c$. Blue points are referred to the woSDD sample while red points represent wSDD data.

enough to justify the implementation of two different analysis and two subsequent different corrections either for D^{*+} and D^+ .

In order to, to cope with the lower tracking efficiency w.r.t. 2013 data sample, after this study, it was decided to reduce the ITS request for the associated tracks from 3 (used on 2013 data) to 2 ITS clusters as default selection criterion.

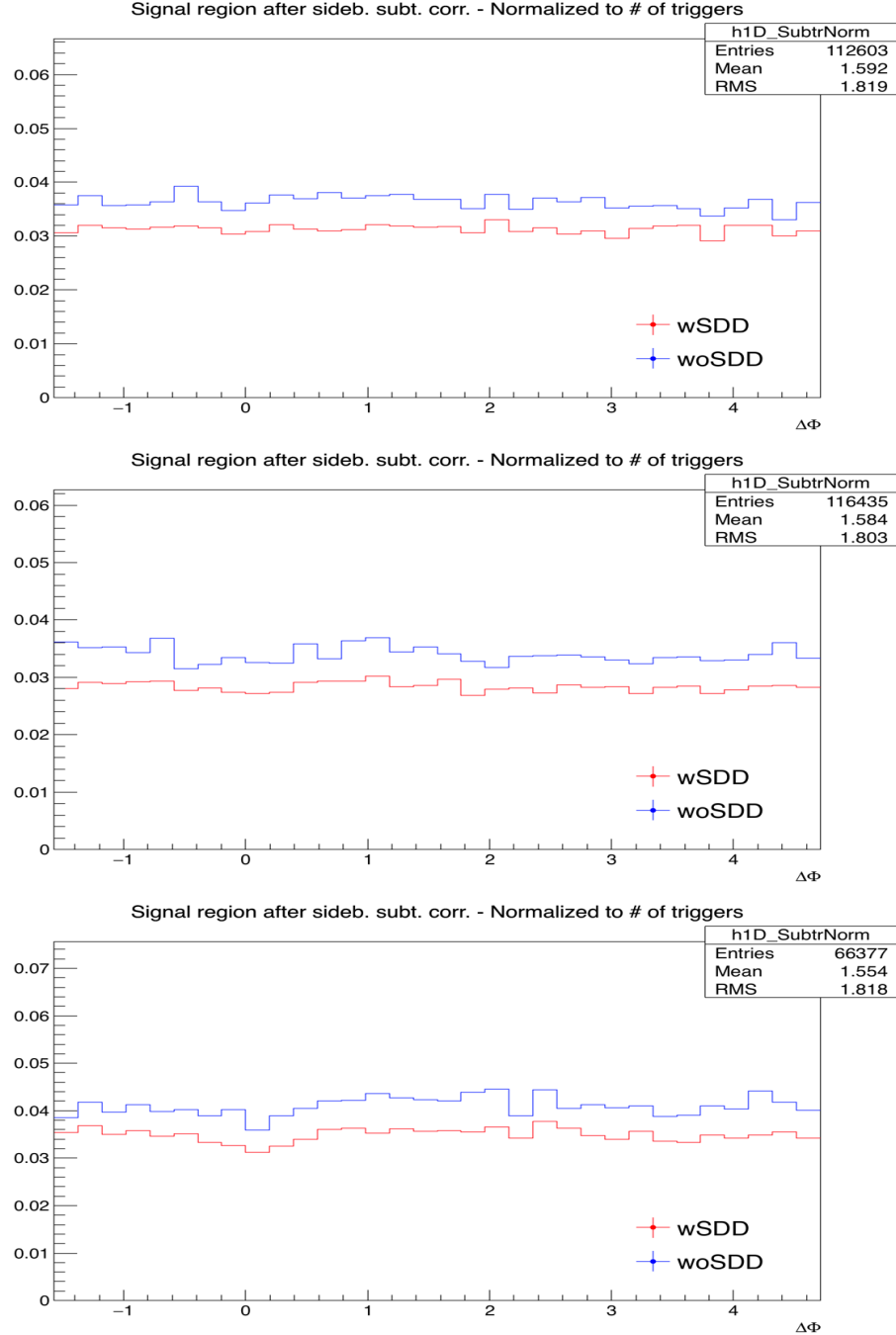


Figure 2: Statistical uncertainty extracted from the azimuthal correlation distribution of D^{*+} with associated charged particles. Top panel: $3 < p_T(D^{*+}) < 5 \text{ GeV}/c$. Mid panel: $5 < p_T(D^{*+}) < 8 \text{ GeV}/c$. Bottom panel: $8 < p_T(D^{*+}) < 16 \text{ GeV}/c$. Blue line is referred to the woSDD sample while the red line represents wSDD data.

137 3 Analysis strategy

138 The analysis follows the same strategy one used in 2013 p-Pb data sample (see published paper [2])
 139 and analysis notes [6], [5]). Correlation pairs are formed by trigger particles (D mesons) reconstructed
 140 and selected in the following p_T^{trig} ranges: $3 < p_T^{\text{trig}} < 5 \text{ GeV}/c$, $5 < p_T^{\text{trig}} < 8 \text{ GeV}/c$, $8 < p_T^{\text{trig}} < 16$
 141 GeV/c , $16 < p_T^{\text{trig}} < 24 \text{ GeV}/c$, and associated particles (charged tracks) for the following p_T^{assoc} re-
 142 gions: $p_T^{\text{assoc}} > 0.3 \text{ GeV}/c$, $0.3 < p_T^{\text{assoc}} < 1 \text{ GeV}/c$, $1 < p_T^{\text{assoc}} < 2 \text{ GeV}/c$, $2 < p_T^{\text{assoc}} < 3 \text{ GeV}/c$,
 143 $p_T^{\text{assoc}} > 3 \text{ GeV}/c$ (with the addition of $p_T^{\text{assoc}} > 1 \text{ GeV}/c$ for comparison with p-Pb 2013 results). In this

analysis, the particle identification defines the trigger particle rather than a momentum cut and therefore the momentum range of the associated particles is not constrained by that of the trigger particle. Our definition of associated particle includes any charged particle coming from the primary vertex of interaction, including those coming from strong and electromagnetic decay of unstable particles, and particles deriving from the decay of hadrons with charm or beauty. We therefore include any charged particle except those coming from weak decays of strange particles and particles produced in the interaction with the detector material. This definition corresponds to that used in the method AliAODMCParticle::IsPyphysicalPrimary(). All associated particles surviving the selection cuts and not matching the adopted criterion are considered as a contamination whose contribution has to be corrected for.

153

154 The analysis is performed through the following steps:

- 155 1. **D meson selection and signal extraction.** For each single event, “trigger” particles are defined
156 as the selected D meson candidates (D^0 , D^+ and D^{*+}) within a given p_T^{trig} range. The detection
157 strategy for D mesons at central rapidity is the same performed for the analyses of the D-meson
158 production at central rapidity [1], and also applied for the D-h analysis on 2010 pp and 2013 p-Pb
159 samples [2]. It is based on the reconstruction of decay vertices displayed from the primary vertex
160 by a few hundred μm and on the identification of the decay-particle species. The identification
161 of the charged kaon and pion in the TPC and TOF detectors is also used, to further reduce the
162 background at low p_T . An invariant-mass analysis is then used to extract the raw signal yield,
163 using the same fit functions described in [2]. The D mesons are selected in the rapidity range
164 varying from $|y| < 0.5$ at low p_T to $|y| < 0.8$ for $p_T > 5 \text{ GeV}/c$.
- 165 2. **Correlation of D candidates with associated tracks.** Particle pairs are formed by correlating each
166 trigger particle with the charged primary particles passing the track selection (excluding those
167 coming from the decay of the D-meson candidate) in a specified p_T^{assoc} interval (which can overlap
168 with the p_T^{trig} range) and in the pseudo-rapidity range $|\eta| < 0.8$. For the D^0 meson, also the low-
169 momentum pion tracks from feed-down of D^{*+} mesons are removed via 3σ invariant mass cut on
170 the $M(K\pi\pi) - M(K\pi)$ difference. This because these soft pion are not related to the charm quark
171 fragmentation chain. For D meson candidates in the invariant mass signal region, defined by a \pm
172 2σ interval around the D meson mass peak, the azimuthal angle difference $\varphi^{\text{assoc}} - \varphi^{\text{trigg}} \equiv \Delta\varphi$ and
173 the pseudorapidity difference $\eta^{\text{assoc}} - \eta^{\text{trig}} \equiv \Delta\eta$ are evaluated and stored to build two-dimensional
174 correlation distribution.
- 175 3. **Correction for limited acceptance and detector inhomogeneities with Event Mixing** The angular
176 correlation distribution may be affected, even for uncorrelated pair of particles, by structures
177 not due to physical effects, but originating from the limited detector acceptance, as well as from
178 angular inhomogeneities in the trigger and track reconstruction efficiencies as a function of $\Delta\varphi$
179 and $\Delta\eta$. Effects of this kind are removed using the Event Mixing technique. In this technique, the
180 analysis is executed on the same data sample of the standard one (called “same event” analysis,
181 SE), but the trigger particles found in each event are correlated to charged particles reconstructed
182 in different events (“Mixed Events” analysis, ME) with similar characteristic, in particular con-
183 cerning the event multiplicity and z position of the primary vertex (see Section 3.3.1).

184

185 The differential yield of associated particles per trigger particle is obtained by

$$\frac{1}{N_{\text{trig}}} \frac{d^2N^{\text{pair}}}{d\Delta\eta d\Delta\varphi} = B_{\text{ME}}(0, 0) \times \frac{S(\Delta\eta, \Delta\varphi)}{B_{\text{ME}}(\Delta\eta, \Delta\varphi)}, \quad (1)$$

186 where N^{pair} is the total number of correlated D-hadron pairs. The functions $S(\Delta\eta, \Delta\varphi)$ and $B_{\text{ME}}(\Delta\eta, \Delta\varphi)$
187 are the signal and the mixed event background distributions, respectively. The later is normalized

188 to its value in $(\Delta\eta, \Delta\phi) = (0, 0)$, i.e. $(B(0, 0))$. Further details on the mixed-event correction are
189 provided in the next section.

190 **4. Subtraction of background correlation from signal distribution.** The invariant mass signal re-
191 gion also includes background D-meson candidates. Their contribution to the raw correlation
192 distribution is subtracted as follows. For each p_T bin, the mean and the sigma of the invariant mass
193 spectrum are extracted. For D^0 and D^+ , a “background” region is defined in the sidebands of the
194 mass distribution as the interval $4 \text{ GeV}/c^2 < |m - m^{\text{pdg}}| < 8 \text{ GeV}/c^2$ (for the D^{*+} meson, only
195 the right sideband is used). The angular correlation distribution for background candidates in this
196 region is extracted and normalized with respect to the background in the signal region estimated
197 from the mass fit. This normalized background correlation distribution is then subtracted from
198 the raw signal one to obtain the signal correlation distribution. The normalization factor is the
199 ratio of the number of background candidates under the signal peak (obtained by integrating the
200 background of the fit function within the signal region) over the number of background candidates
201 in the sidebands (obtained via bin-counting in the sideband region). An example of the signal re-
202 gion, sideband and sideband-subtracted 1D correlation distributions (along $\Delta\phi$) is shown in figure
203 3, together with the comparison of the three distributions after the normalization to the number of
204 triggers.

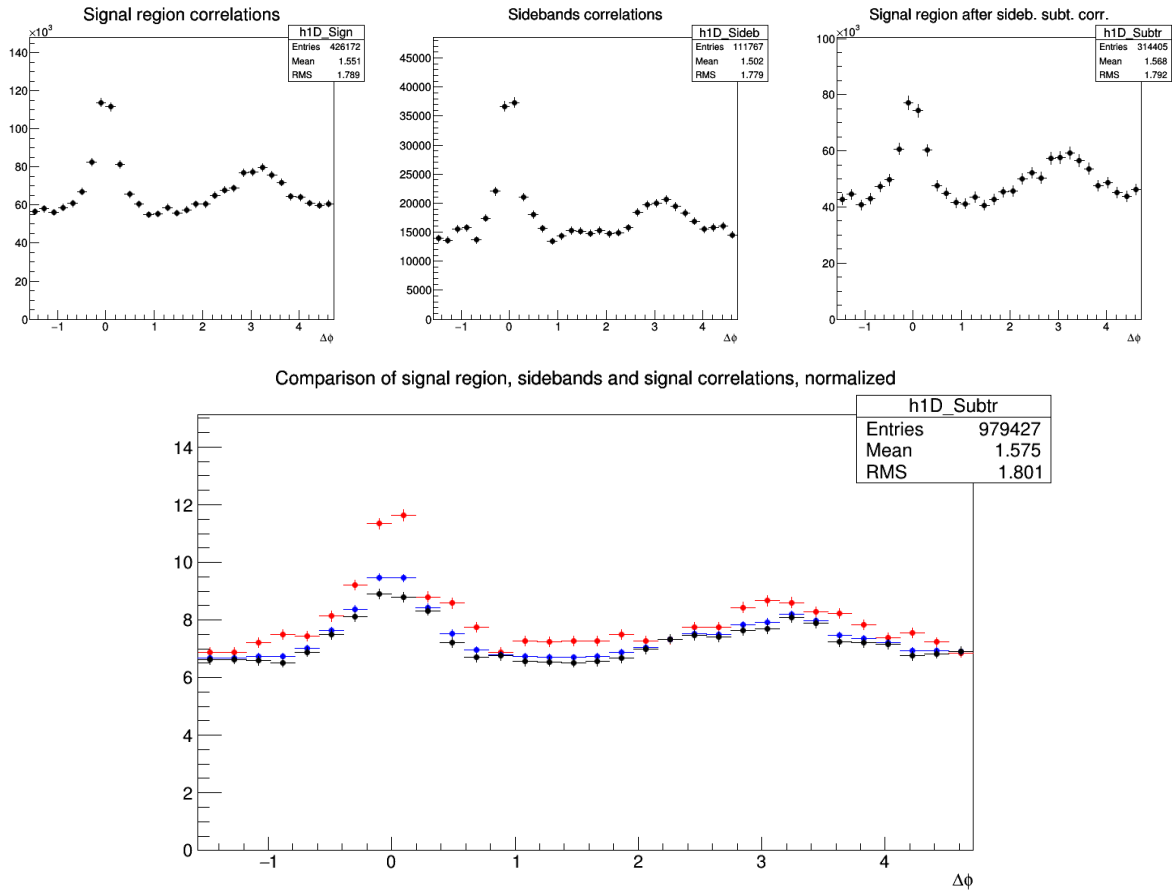


Figure 3: Top: Example of D^0 -h signal region (left), sideband (middle), and signal minus sideband (right) correlation distributions. Bottom: signal region per-trigger normalized correlation distribution (blue), sideband region per-trigger normalized correlation distribution (red), background-subtracted per-trigger normalized correlation distribution (black).

205 **5. Correction for D meson efficiency and associated track efficiency.** After filling the signal and
206 background correlation distributions, it is necessary to take into account also for the correlations

with tracks, those are not reconstructed, or not passing the quality selection due to poor reconstruction. In the same way, the loss of D-mesons which are not reconstructed, or do not pass the selection, impacts the correlation distribution shape. Hence, each pair is weighted by the inverse of the product of the associated track and D meson reconstruction efficiency, ε_{trk} and ε_{trig} . Further details are provided later on in this section.

6. **Projection in $\Delta\varphi$.** The limited statistics available does not allow to study the two dimensional $(\Delta\eta, \Delta\varphi)$ distribution, which is therefore projected to the $\Delta\varphi$ axis by integrating on $|\Delta\eta| < 1$. Despite, in principle, our maximum $\Delta\eta$ acceptance is of $|\Delta\eta| < 1.6$, removing the large $|\Delta\eta|$ regions allow us to reject angular regions with very low statistics, where fluctuations would be amplified by a large mixed-event correction, and avoid the so-called wings effect.

As the difference in the azimuthal angle is periodic ($\Delta\varphi = 0 = 2\pi$), the $\Delta\varphi$ -range is limited to the essential range of 2π . The $\Delta\varphi$ -limits are chosen to be $[-\pi/2, 3\pi/2]$ in order to provide a good visibility of the correlation pattern, which peaks around 0 and π .

7. **Correction for the contamination of secondary particles** The DCA to primary vertex cut, applied during the associated track selection, has the role of removing the secondary particles from the associated track sample. Secondary particles are indeed produced either from long-lived strange hadrons or from interaction of particles with the detector material. A residual contamination from secondary tracks is hence expected in the correlation distributions. This contamination is estimated from Monte Carlo simulation based on Pythia as described more in detail in the next section. The background-subtracted event-mixing corrected correlations are multiplied by a purity factor to encounter this contribution.

8. **Correction for bias on B to D decay topologies** The presence of the topological cuts for the D-meson selection indirectly induce a bias on the topology of the B to D decay topologies, favouring cases with a small opening angle between the D-meson and the other tracks from the B decay. This affects the feed-down component of the data correlation distributions. This effect is corrected for with a procedure described in the subsection 3.3.3. Note that this correction is a novelty with respect to the previous analyses, where only a quite conservative systematic uncertainty was applied to take into account this effect.

9. **Correction for feed-down of D meson from b-hadron decay** The selection strategy employed for the D meson candidates selection enhances the fraction of reconstructed D mesons coming from the decay of a b-hadron. Typical values, with the cuts used for the D-meson selection, are of the order of 10% or less. The correlation distribution of these secondary D mesons will be sensitive to the properties of beauty jets and beauty hadron decay, which in general differ from those relative to charm jets and hadrons. The procedure used to subtract this contribution is described in the next paragraphs of this section.

10. **Study of correlation properties.** The properties of the azimuthal correlation distribution are quantified by fitting the distribution with a function composed of two Gaussian functions, modelling the near and the away side peaks, and a constant term describing the baseline. The mean of the Gaussian are fixed at $\Delta\varphi = 0$ and $\Delta\varphi = \pi$. To accomplish the 2π periodicity of the $\Delta\varphi$ variable, the Gaussian functions are “duplicated” with mean at $\Delta\varphi = 2\pi$ and $\Delta\varphi = -\pi$. The fitting procedure is described in details in Section 5.

3.1 Mass plots and cut optimization

The invariant mass distributions of D^0 , D^{*+} and D^+ in the various pt ranges are shown in Figure 4, 5 and 6 respectively. Note that the distributions are weighted by the D-meson selection and reconstruction efficiency, to allow a correct normalization of the correlation distributions, which have also these weights.

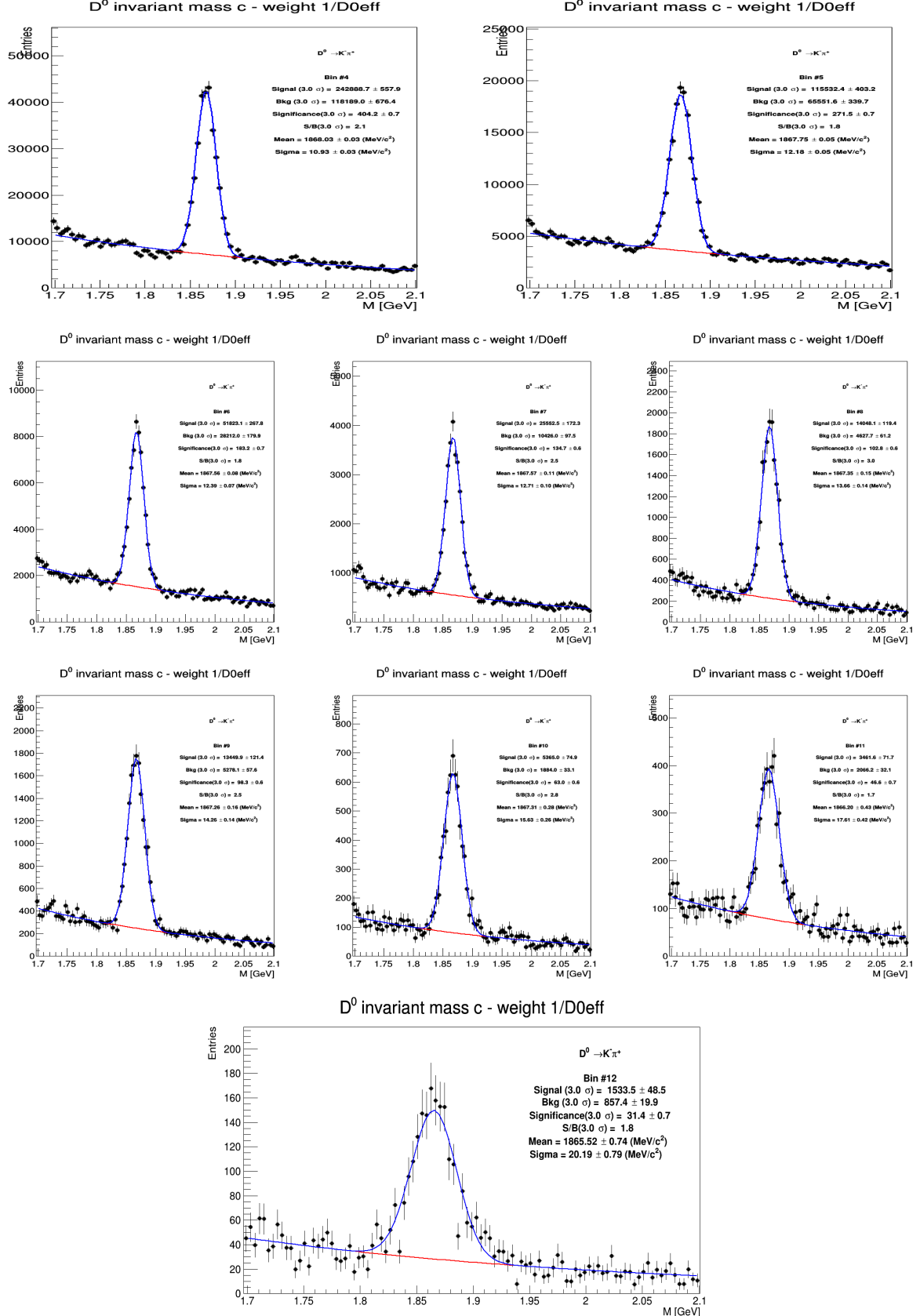


Figure 4: Invariant mass distributions of D^0 corrected with efficiency in different p_T regions. Top: $3 < p_T^D < 4 \text{ GeV}/c$ (left), $4 < p_T^D < 5 \text{ GeV}/c$ right), Mid 1: $5 < p_T^D < 6 \text{ GeV}/c$ (left), $6 < p_T^D < 7 \text{ GeV}/c$ (middle), $7 < p_T^D < 8 \text{ GeV}/c$ (right); Mid2: $8 < p_T^D < 10 \text{ GeV}/c$, $10 < p_T^D < 12 \text{ GeV}/c$ (middle), $12 < p_T^D < 16 \text{ GeV}/c$ (right) and Bottom: $16 < p_T^D < 24 \text{ GeV}/c$.

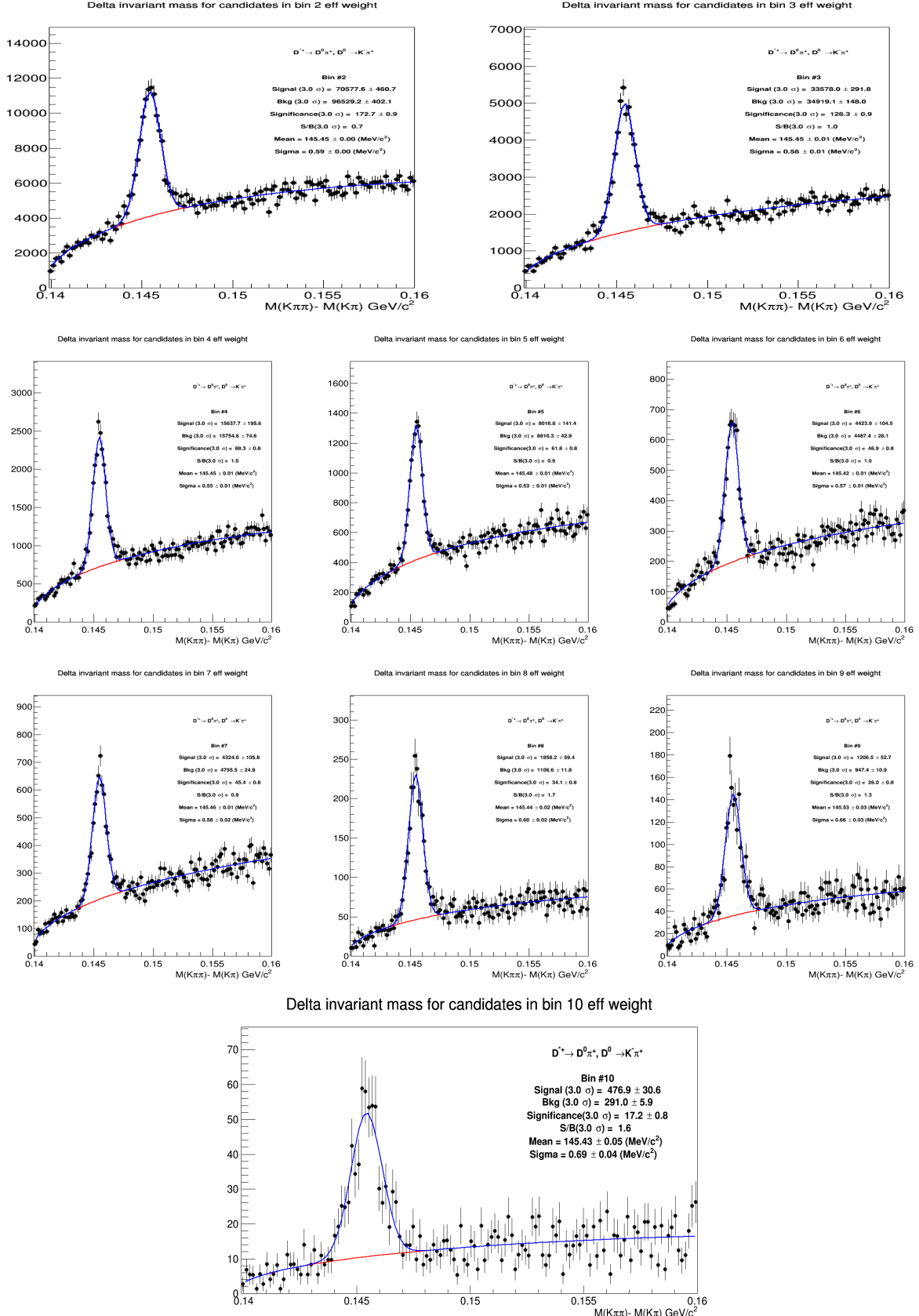


Figure 5: Invariant mass distributions of D^{*+} corrected with efficiency in different p_T^D regions. Top: $3 < p_T^D < 4$ GeV/c (left), $4 < p_T^D < 5$ GeV/c (right), Mid 1: $5 < p_T^D < 6$ GeV/c (left), $6 < p_T^D < 7$ GeV/c (middle), $7 < p_T^D < 8$ GeV/c (right); Mid 2: $8 < p_T^D < 10$ GeV/c, $10 < p_T^D < 12$ GeV/c (middle), $12 < p_T^D < 16$ GeV/c (right) and Bottom: $16 < p_T^D < 24$ GeV/c .

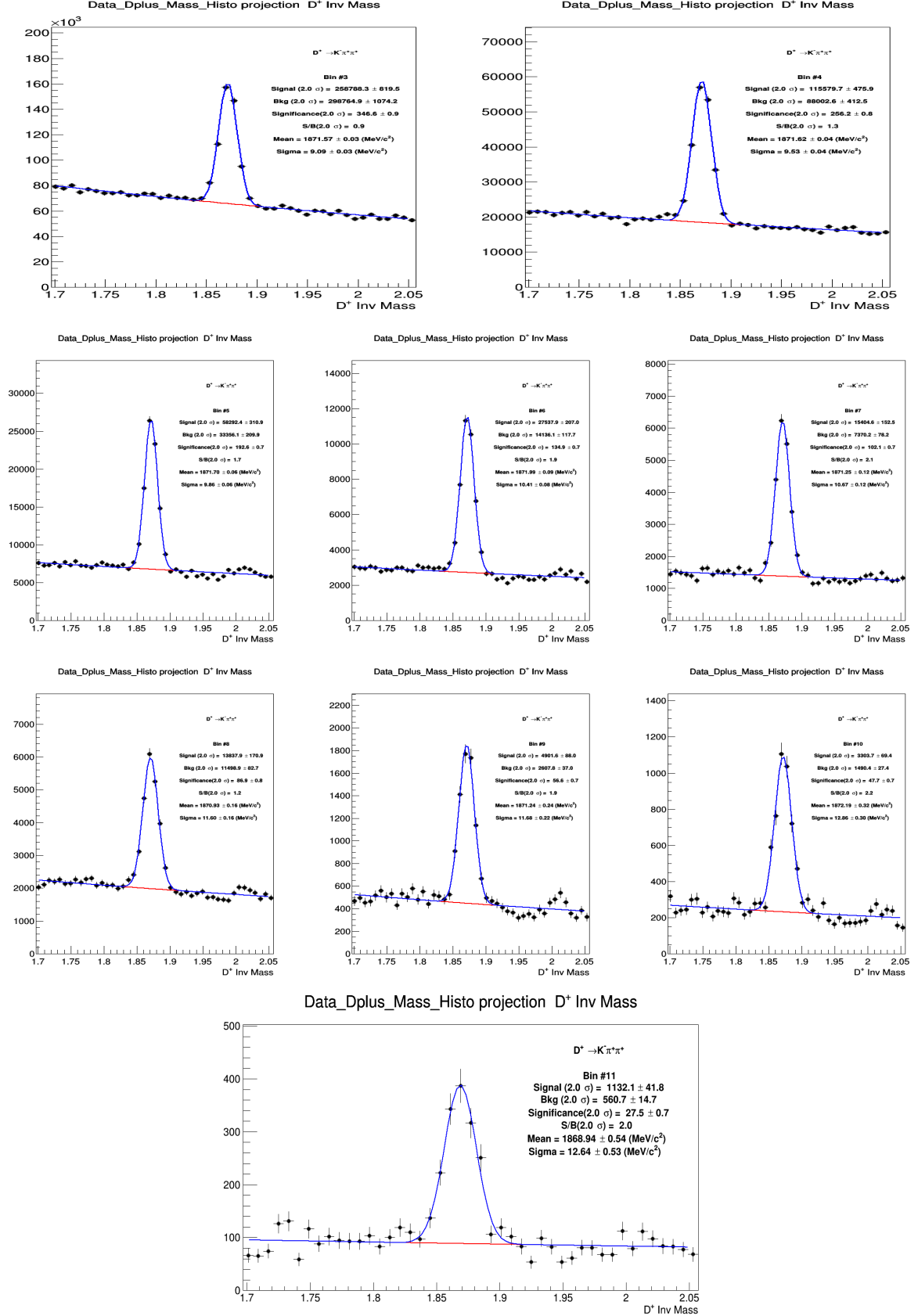


Figure 6: Invariant mass distribution of D^+ corrected with efficiency in different p_T regions. Top: $3 < p_T^D < 4$ GeV/c (left), $4 < p_T^D < 5$ GeV/c (right), Mid 1: $5 < p_T^D < 6$ GeV/c (left), $6 < p_T^D < 7$ GeV/c (middle), $7 < p_T^D < 8$ GeV/c (right); Mid2: $8 < p_T^D < 10$ GeV/c, $10 < p_T^D < 12$ GeV/c (middle), $12 < p_T^D < 16$ GeV/c (right) and Bottom: $16 < p_T^D < 24$ GeV/c .

For D^{*+} , the standard D2H p-Pb cuts (for the 2013 cross section analysis, [7]) were used. The same holds for the D^+ , but with the addition of cuts on the normalized decay length in xy plane and of the normalized difference between measured and expected daughter track impact parameters (topomatic cut). A particular cut optimization was instead performed for the D^0 meson. Twelve cut sets were tried, with the goal of increasing the S/B factor, in order to reduce fluctuations induced by the sideband subtraction (the limiting factor for the analysis performance). In Figure 7 the D^0 -h correlation distributions are shown for the different cut sets, in exemplary kinematic regions (left column), together with the bin-by-bin relative statistical uncertainty on the data points (right column). The best cut set (option G) was defined from the standard cuts used for the p-Pb 2013 cross section analysis, with a tightened selection on the cosine of the pointing angle, and with the addition of a cut on the normalized decay length in xy plane and of a selection on the normalized difference between measured and expected daughter track impact parameters (topomatic cut).

3.2 Code used for the analysis

The code used for D meson-hadron correlation analysis is fully committed in AliPhysics. The analysis classes can be found in `$ALICE_ROOT/PWGHF/correlationHF/`. The D meson specific classes where the aforementioned steps are carried out are `AliAnalysisTaskDStarCorrelations`, `AliAnalysisTaskSED0Correlations` and `AliAnalysisTaskDplusCorrelations`. The classes which are common to the D meson specific analysis which includes the associated particle cuts and the correlation observables are `AliHFAssociatedTrackCuts`, `AliHFCorrelator`, `AliHFOfflineCorrelator`, `AliReducedParticle` and `AliDhCorrelationExtraction`. Several additional classes and macros in the same folder deal with the correction steps.

The final results presented here are extracted are the HFCJ pPb (n. 88) train runs 254-257 (for D^0 and D^+) and 268-271 (for D^{*+}).

3.3 Further details on corrections

3.3.1 Event Mixing

The event-mixing technique is used for correcting the raw correlation distribution for effects arising from the detector limited acceptance in rapidity and detector spatial inhomogeneities. The calculation of the Event Mixing correlation distribution is performed online. An event pool is created, where events preceding the one containing a D candidate are stored based on their properties (position of the vertex along the z axis and multiplicity). Each time a D meson candidate is found in an event, only the events contained in the same pool as the event under analysis is used to evaluate the correlations for the event mixing correction.

For D^0 and D^+ , an offline approach for the mixed-event correction has been developed. In this approach, D-meson triggers and associated tracks from every analyzed event are stored in dedicated TTree, together with the needed kinematic information to build correlation distributions, and with identifiers of the events to which they belong. In this way, it is possible to correlate each D meson with all the tracks belonging to the same pool over the full event sample, and not being limited to the same subjob as for the online analysis. This allows to increase the statistics of the mixed-event correlation distributions. It was verified that online and offline approaches are fully compatible within the statistical uncertainties.

The multiplicity and z vertex position bins for the pools used in the p-Pb analysis (for both approaches) are the following:

- Multiplicity bins: $(0, 35); (35, 55); (55, +\infty)$
- Vertex z (cm) = $(-10, -1.5); (-1.5, 3.5); (3.5, 10)$

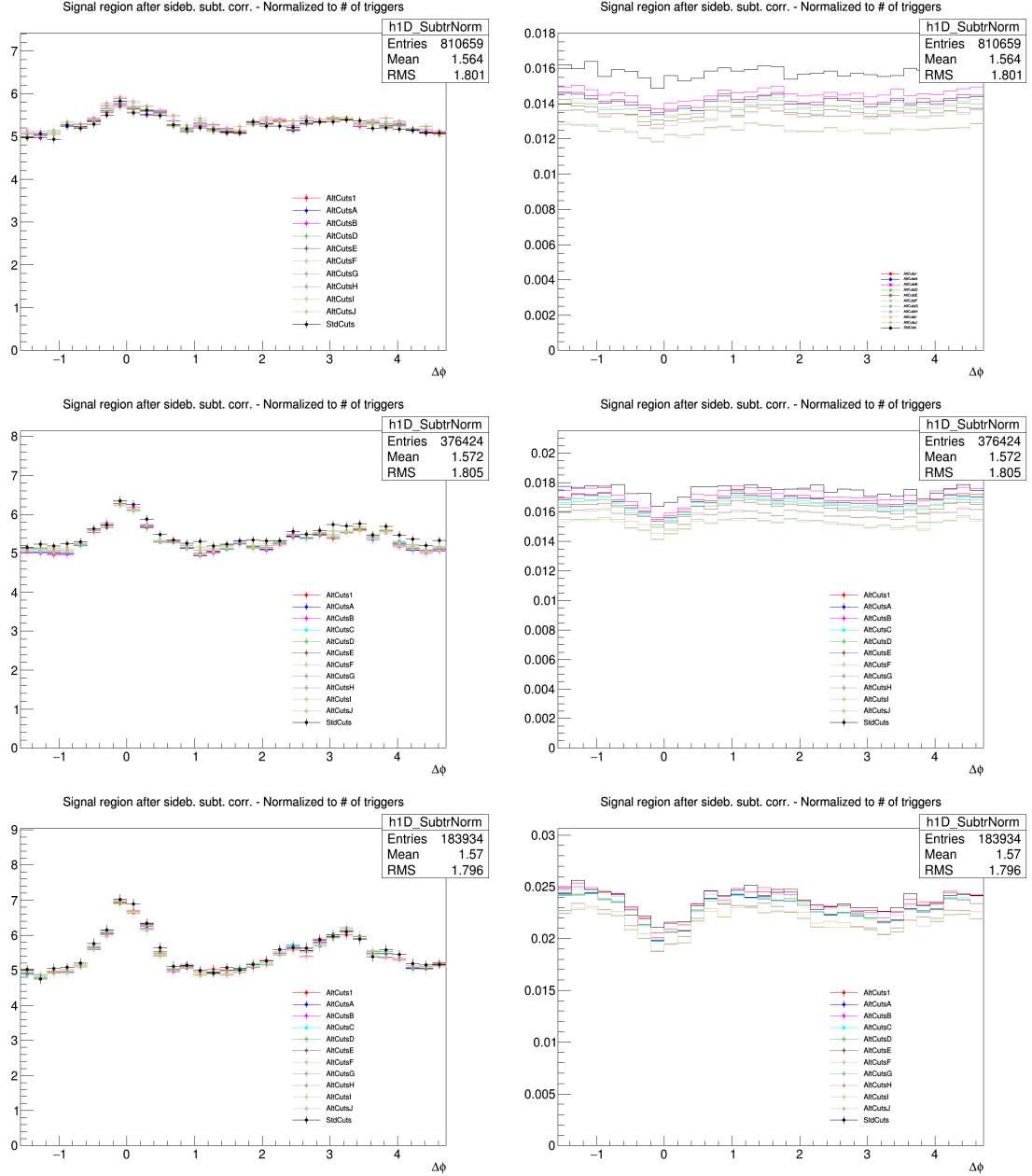


Figure 7: D^0 - h correlation distributions with different cut options (left) and point-by-point relative statistical uncertainty (right) for $3 < p_T^D < 5 \text{ GeV}/c$ (top), $5 < p_T^D < 8 \text{ GeV}/c$ (middle), $8 < p_T^D < 16 \text{ GeV}/c$ (bottom), in all cases with associated track $p_T > 0.3 \text{ GeV}/c$.

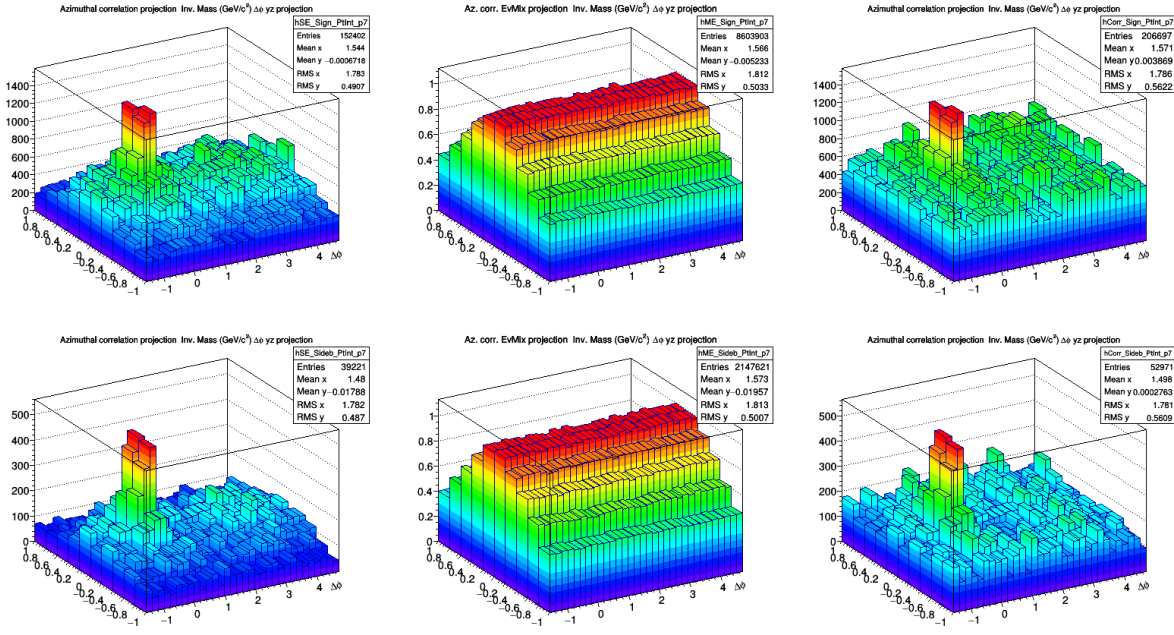


Figure 8: D^0 meson ($\Delta\phi$, $\Delta\eta$) correlation for in the signal region (top row) and sidebands (bottom row) from Single Event (left) and Mixed Event analysis (center) for high p_T : $8 < p_T < 16 \text{ GeV}/c$ with associated $p_T > 0.3 \text{ GeV}/c$. The right column shows the SE/ME corrected distributions.

295 In an ideal case, the mixed event distribution is expected to have a constant flat distribution as function
 296 of $\Delta\phi$ and a triangular shaped distribution in $\Delta\eta$ deriving from the limited η acceptance of the detector.
 297 In case, instead of detector inefficient regions, or holes, in the same angular position for D meson and
 298 associated tracks, these structures produce an excess of correlations at $\Delta\phi = 0$ in the $\Delta\phi$ distribution. The
 299 obtained distribution is used as a weight in each correlation bin, i.e, the corrected correlation distribution
 300 is calculated as follows:

$$\frac{dN^{corr}(\Delta\phi\Delta\eta)}{d\Delta\phi d\Delta\eta} = \frac{\frac{dN^{SE}(\Delta\phi\Delta\eta)}{d\Delta\phi d\Delta\eta}}{\frac{dN^{ME}(\Delta\phi\Delta\eta)}{d\Delta\phi d\Delta\eta}} \frac{dN^{ME}(0,0)}{d\Delta\phi d\Delta\eta} \quad (2)$$

301 In Eq.2, the last term stands for the average of the bins in the region $-0.2 < \Delta\eta < 0.2$, $-0.2 < \Delta\phi < 0.2$
 302 (multiple bins are used to minimize the effect of statistical fluctuations on the normalization of the mixed-
 303 event plots). This kind of normalization, adopted in the analysis of hadron-hadron correlations, relies
 304 on the fact that at $(\Delta\eta, \Delta\phi) = (0,0)$ the trigger and associated particle experience the same detector
 305 effects. In the D meson case this is true only on average and not at very low p_T , since D mesons are
 306 reconstructed from particles that can go in different detector region. However, $(\Delta\eta, \Delta\phi) = (0,0)$ is in
 307 any case the region with maximum efficiency for the pairs (both correlated and uncorrelated). Thus the
 308 same convention was adopted.

309 The mixed-event correlation distributions are built in both D meson signal and sideband regions. Both
 310 are corrected with the relative distributions. An example of the mixed-event distributions, and of the
 311 outcome of the mixed-event correction, is provided in Figures 8 and 9. The expected triangular shape
 312 in $\Delta\eta$, for the mixed-event distributions, addresses the effect of the limited detector pseudo-rapidity
 313 acceptance. Note that the mixed-event distribution is limited to the interval $|\Delta\eta| < 1$: the decision to
 314 limit the mixed-event correction, and thus the whole analysis, to this range was taken in order to avoid
 315 the so-called “wing effect”, i.e. the wing-like structures arising in the correlation distribution at large $\Delta\eta$
 316 due to the limited filling of the correlation bins in that region.

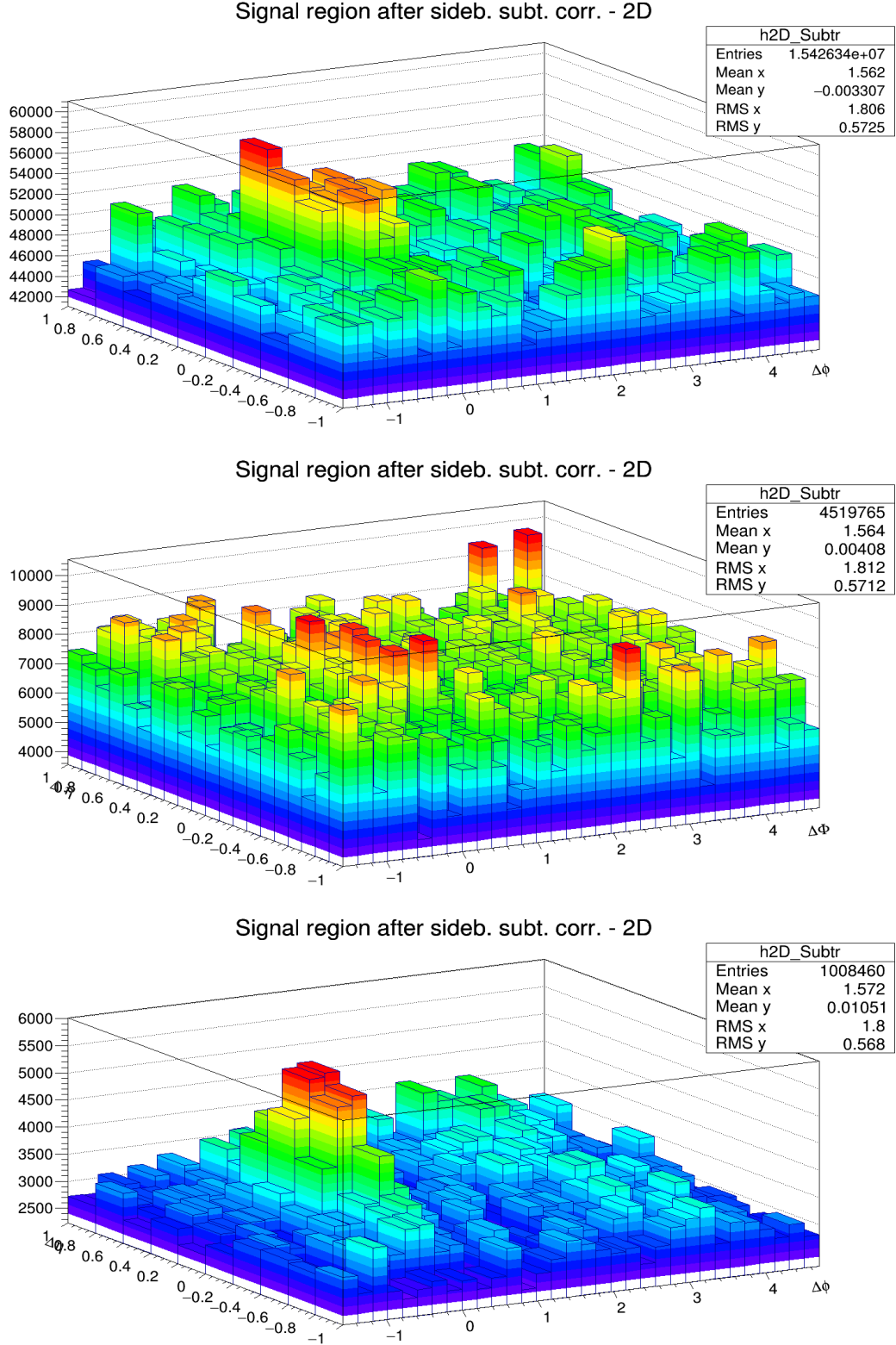


Figure 9: Top: $(\Delta\phi, \Delta\eta)$ correlation distribution of D^0 -h with $3 < p_T < 5$ GeV/c and associated track kinematic range: $0.3 < p_T < 1.0$ GeV/c Mid: $(\Delta\phi, \Delta\eta)$ correlation distribution of D^{*+} -h with $3 < p_T < 5$ GeV/c and associated track p_T Threshold: $p_T > 0.3$ GeV/c Bottom: $(\Delta\phi, \Delta\eta)$ correlation distribution of D^+ -h with $8 < p_T < 16$ GeV/c and associated track p_T threshold: $p_T > 0.3$ GeV/c. All the plots are shown after the mixed-event correction and the sideband subtraction.

317 **3.3.2 Tracking and D-meson trigger efficiency**

318 **(i) Tracking efficiency** - The tracking efficiency was calculated by obtaining the ratio between the yield
 319 at the reconstructed level and generated level, for a defined “type” of particles (in our case non-identified
 320 particles) and it is estimated differentially in p_T , η , and z_{vtx} of the charged particles.

321

322 Tracking efficiency maps were produced as TH3D histograms (p_T , η , z_{vtx}) obtained from MC analysis on
 323 the minimum-bias samples LHC17f2b_fast and LHC17f2b_cent_woSDD, and applying at reconstructed
 324 level the track selections (summarized in Table. 2). These efficiency maps were used in the analysis
 325 tasks to extract single track efficiencies; each correlation pairs found in the data analysis was inserted in
 326 correlation plots with a weight of **1/efficiency value**. Example plots of the p_T dependence of the tracking
 327 efficiency for two different track selections (the standard on top, a tighter selection used for systematics
 328 on bottom) are shown in Fig. 10.

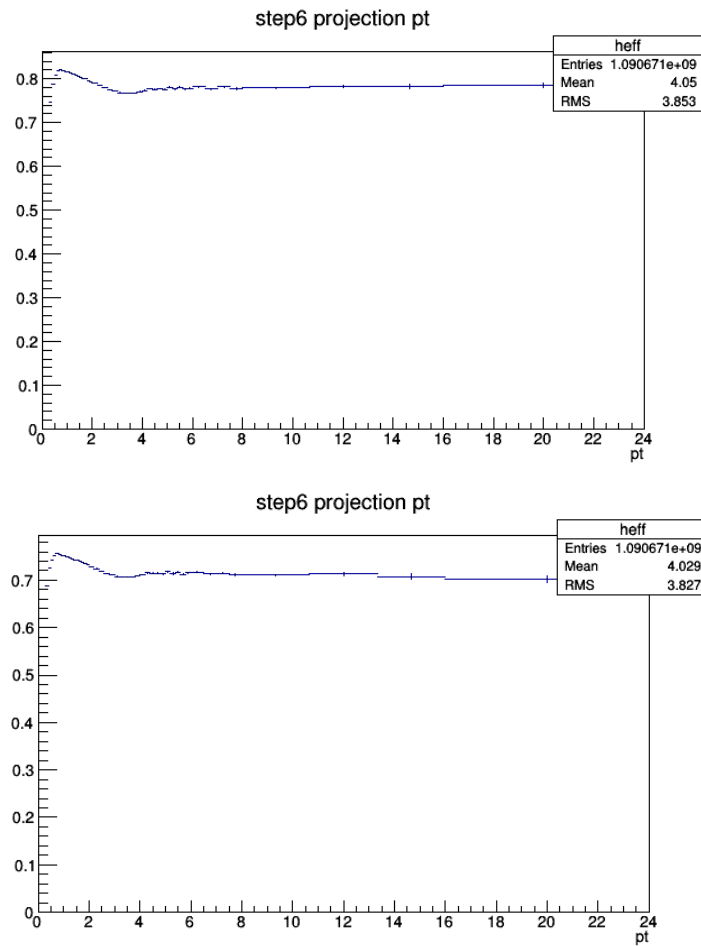


Figure 10: p_T efficiency map for standard track selection (2 ITS clusters) on top panel, and alternate track selection, used for systematics (3 ITS clusters, filterbit4, ITS refit) on bottom panel.

³²⁹ Details of cuts at event level and particle/track selection at different steps are listed in Table 2 .

MC Generated	
Stages	Cuts
1. MC Part with Generated Cuts	After Event Selection Charge PDG Code Physical Primary Kinematics Cuts $-0.8 < \eta < 0.8$ $p_T > 0.3$ (GeV/c)
2. MC Part with Kine Cuts	
MC Reconstructed	
4. Reco tracks	After Event Selection Physical Primary Kinematics Cuts $-0.8 < \eta < 0.8$ $p_T > 0.3$ (GeV/c)
5. Reco tracks with Kine Cuts	
6. MC true with Quality Cuts	Quality Cuts SetRequireSigmaToVertex(kFALSE) SetDCAToVertex2D(kFALSE) SetMinNCrossedRowsTPC(70) SetMinRatioCrossedRowsOverFindableClustersTPC(0.8) SetMinNClustersITS(2) SetMaxChi2PerClusterTPC(4) SetMaxDCAToVertexZ(1) SetMaxDCAToVertexXY(1) SetRequireTPCRefit(TRUE) SetRequireITSRefit(FALSE) Same as step 6
7. Reco tracks with Quality Cuts	

Table 2: The list of event and particle/track selection cuts used in the estimation of single track efficiency

³³⁰

³³¹ **(ii) D meson efficiency** - Due to limited statistics, the correlation analysis is performed in quite wide p_T bins and in each of them the reconstruction and selection efficiency of D mesons is not flat, in particular in the lower p_T region. We correct for the p_T dependence of the trigger efficiency within each p_T -bin.

³³⁴ This correction is applied online, by using a map of D meson efficiency as a function of p_T and event multiplicity (in terms of SPD tracklets in $|\eta| < 1$) extracted from the enriched Monte Carlo sample LHC17d2a_fast_new. The η dependence was neglected due to the statistics of the available Monte Carlo sample, which rule out the possibility of performing a 3D study.

³³⁸ To properly count the number of trigger particles used to normalize the correlation distributions, N_{trig} , each D meson is weighted with the inverse of its efficiency in the invariant mass distribution. The main role of the correction for the D meson efficiency is to account for the p_T dependence of the correlation distribution within a given D meson p_T interval. Indeed, only the p_T shape of the D meson efficiency within the correlation p_T^{trig} ranges is relevant while the average value in the p_T range is simplified due to the normalization of the correlation distribution to the number of trigger particles.

344 Efficiency plots for D^0 , D^+ and D^{*+} mesons are shown in Figs. 11 and 12.

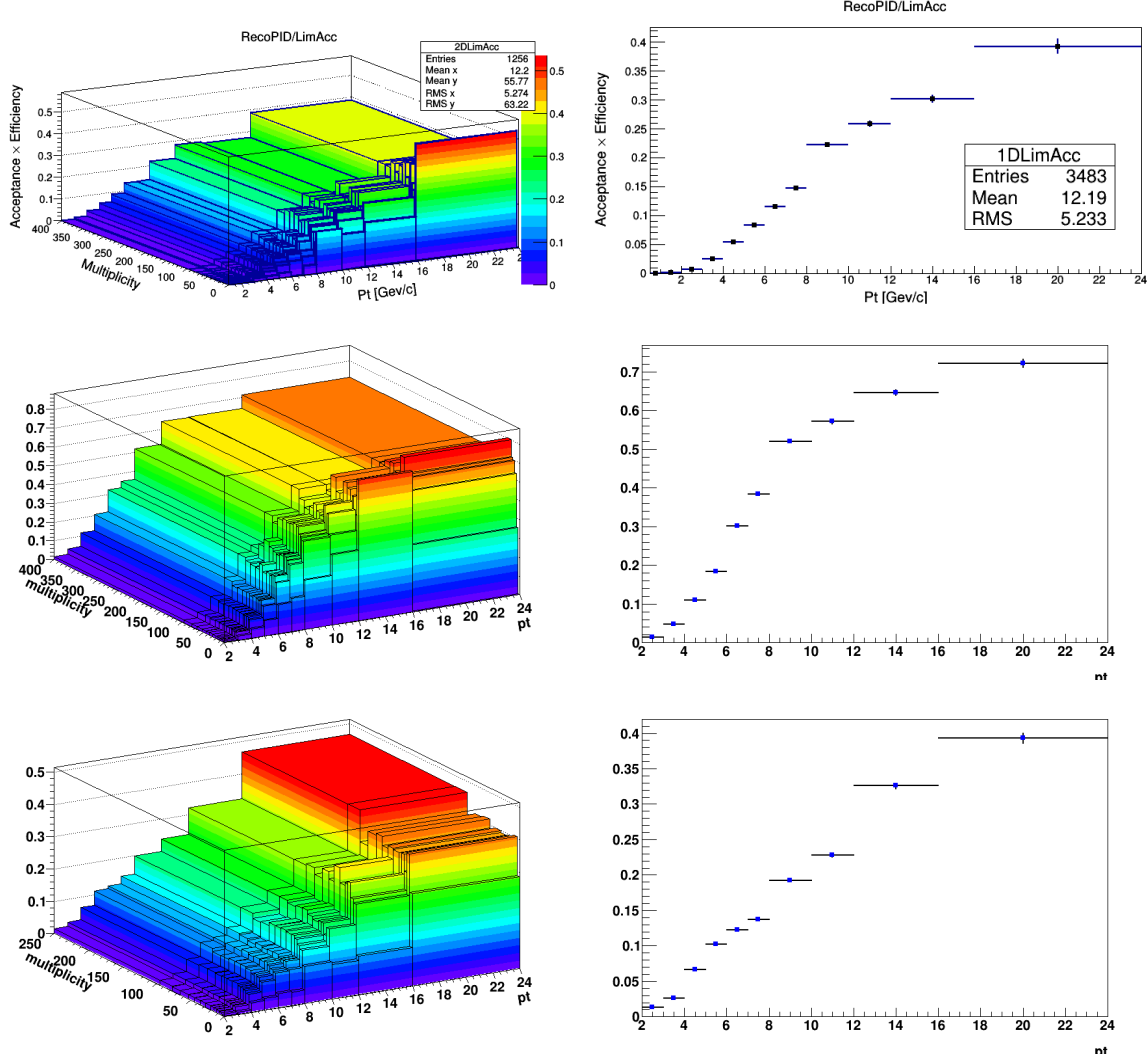


Figure 11: Top panel: (p_T , multiplicity) dependence (left) and p_T dependence (right) of prompt D^+ meson efficiency. Mid panel: (p_T , multiplicity) dependence (left) and p_T dependence (right) of prompt D^{*+} meson efficiency. Bottom panel: (p_T , multiplicity) dependence (left) and p_T dependence (right) of prompt D^0 meson efficiency.

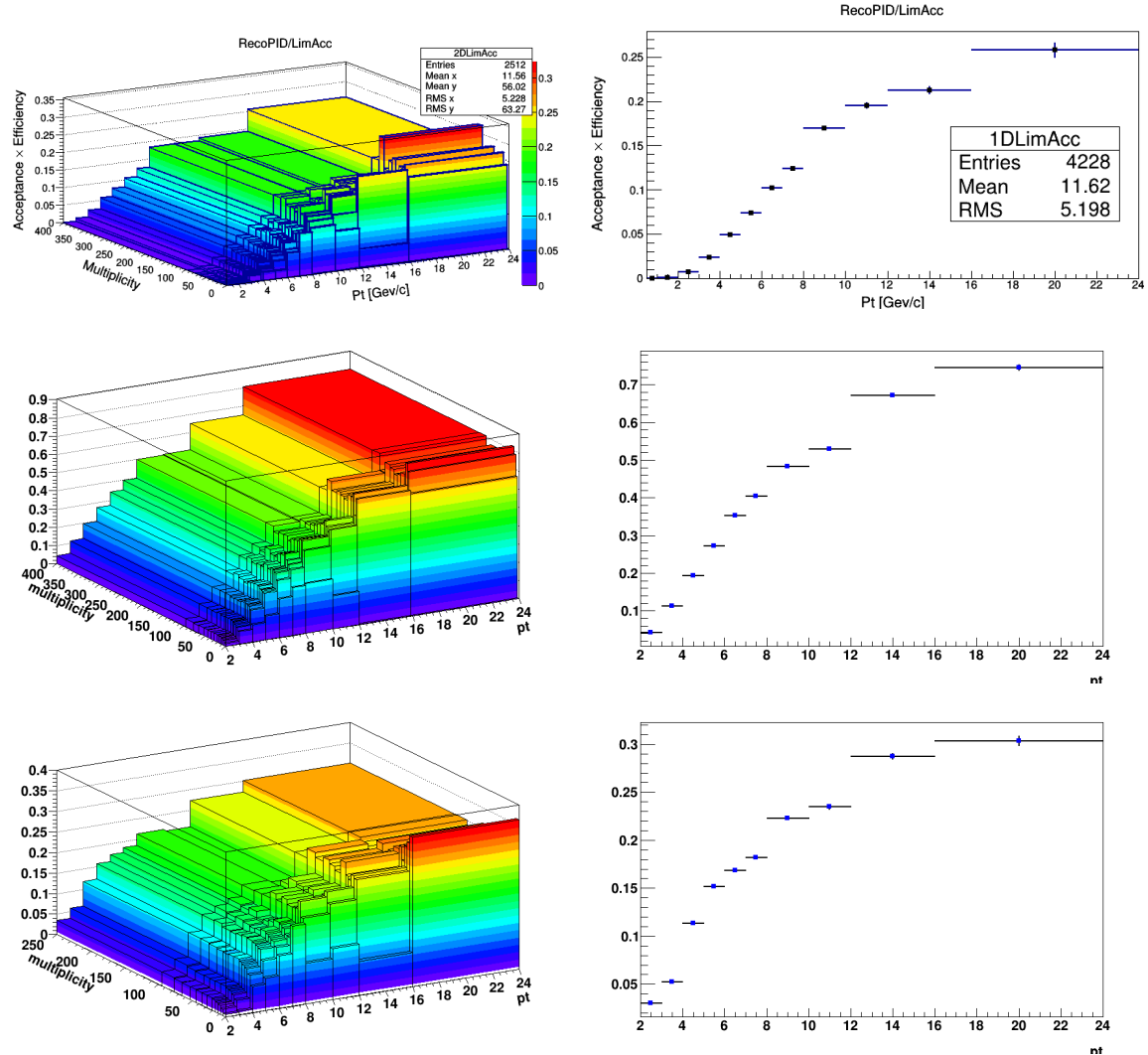


Figure 12: Top panel: (p_T , multiplicity) dependence (left) and p_T dependence (right) of feed-down D^+ meson efficiency. Mid panel: (p_T , multiplicity) dependence (left) and p_T dependence (right) of feed-down D^{*+} meson efficiency. Bottom panel: (p_T , multiplicity) dependence (left) and p_T dependence (right) of feed-down D^0 meson efficiency.

345 It was observed that multiplicity dependence of the efficiency does not bias the extraction of the signal
 346 yield from the invariant mass distributions (which, as anticipated, are also weighted in the same manner).
 347 In addition, the multiplicity dependence of the efficiencies (shown for the D^0 , in integrated p_T range, in
 348 Fig. 13) is rather flat in the range 20-80 tracklets, where about 90% of the reconstructed D -mesons are
 found, which explains why it has a negligible effect on the correlation distributions on this data sample.

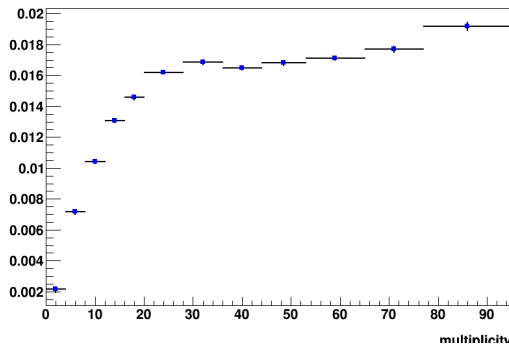


Figure 13: Prompt D^0 meson efficiency as a function of multiplicity (SPD tracklet in $|\eta| < 1$.

350 3.3.3 Correction for bias on B to D decay topologies

- 351 To verify the consistency of the analysis chain and of the corrections applied to the correlation distribu-
352 tions extracted from data, a Monte Carlo closure test was setup and tried on the D^0 -h analysis.
- 353 On the Monte Carlo enriched with charm and beauty quarks (LHC17d2a_fast_new), the correlation analy-
354 sis was performed both at kinematic level and at reconstructed level. At kinematic level, only acceptance
355 cuts were applied on the D mesons and the associated particles, using the Monte Carlo information for
356 the identification of the D mesons and the hadrons in the event and rejecting the non-primary particles.
357 At reconstructed level, the analysis was performed as if it were executed on data, applying the event se-
358 lection, the acceptance cuts for D mesons and the associated particles, selecting the D meson candidates
359 with filtering cuts on their daughters, topological cuts and PID selection, and then keeping only the true
360 D mesons by matching with the Monte Carlo truth; non-primary particles were rejected by means of
361 the DCA selection. Event mixing correction was applied both at reconstructed and at kinematic level,
362 where it takes into account just the effects of the acceptance cuts. In addition, at reconstructed level, the
363 efficiency corrections for D mesons and associated tracks were also applied.
- 364 Examples of correlation plots at both steps are shown in Figures 14 and 15, separating the correlation
365 contribution of associated tracks and D mesons from different origins, as described in the legend of the
366 plots.

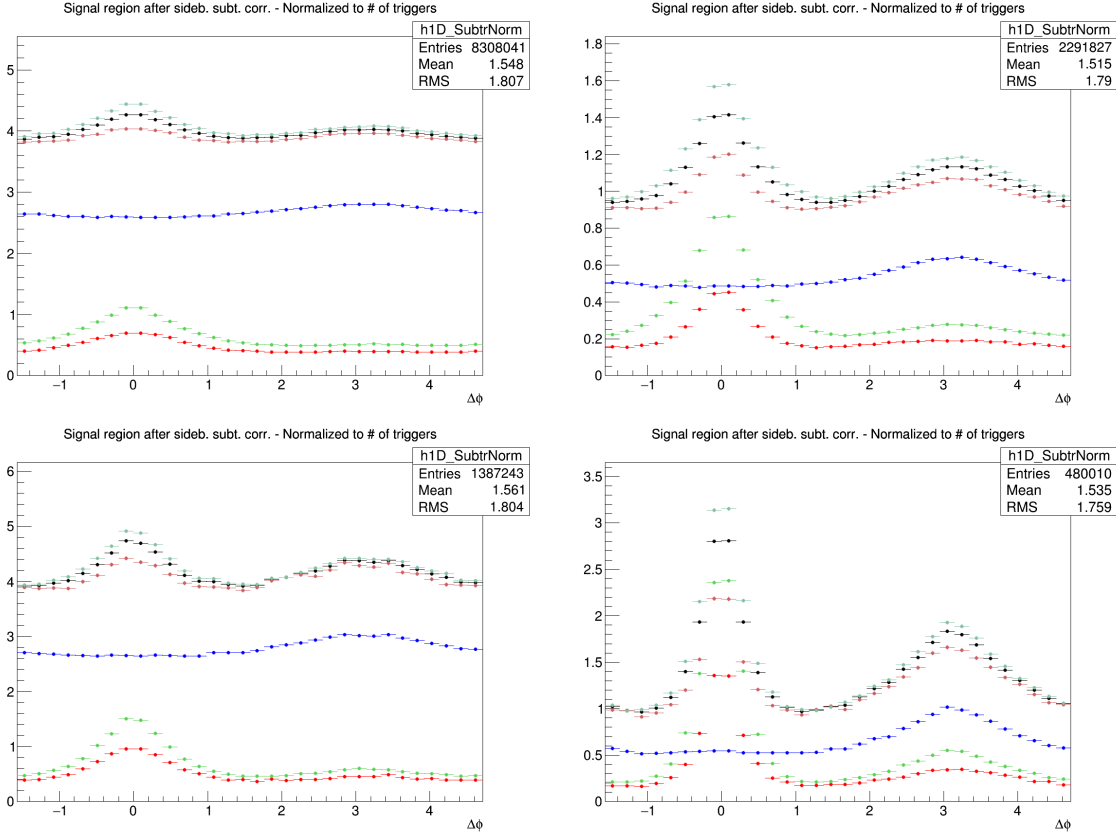


Figure 14: D^0 -hadrons azimuthal correlation distribution obtained from Monte Carlo, at kinematic step. Black points: All D^0 -all hadrons, normalized by all D^0 triggers; light red points: D^0 from c-hadrons from c, normalized by c- D^0 triggers; dark red points: D^0 from c-all hadrons, normalized by c- D^0 triggers; light green points: D^0 from b-hadrons from b, normalized by b- D^0 triggers; dark green points: D^0 from b-all hadrons, normalized by b- D^0 triggers; blue points: All D^0 -hadrons from light quarks, normalized by all D^0 triggers. The panels show the ranges: $3 < p_T(D) < 5 \text{ GeV}/c$, $0.3 < p_T(\text{assoc}) < 1 \text{ GeV}/c$ (top-left); $3 < p_T(D) < 5 \text{ GeV}/c$, $p_T(\text{assoc}) > 1 \text{ GeV}/c$ (top-right); $8 < p_T(D) < 16 \text{ GeV}/c$, $0.3 < p_T(\text{assoc}) < 1 \text{ GeV}/c$ (bottom-left); $8 < p_T(D) < 16 \text{ GeV}/c$, $p_T(\text{assoc}) > 1 \text{ GeV}/c$ (bottom-right).

367 The consistency check was performed to verify whether, after having applied all the corrections to the
 368 azimuthal correlation plots at reconstructed level, the results were compatible with the ones at kinematic
 369 level. Hence, the ratios of fully corrected reconstructed plots over kinematic plots were evaluated in all
 370 the D^0 p_T bins and for the various p_T thresholds for the associated tracks, separating the contributions for
 371 the different origins of particles and triggers. The ratios, shown in Figure 16, denote a good compatibility
 372 with 1, within the uncertainties, with the only exception being due to some structures in the near side
 373 region for the beauty origin case. These structures were already found in the pp 2010 and p-Pb 2013
 374 analysis, and it was verified that they are induced by our topological selection for the D mesons. Indeed,
 375 in cases in which the D meson triggers come from B hadrons, applying the topological cuts (especially
 376 the cosine of the pointing angle) tends to favour cases with a small angular opening between the products
 377 of the B hadron decay (i.e. the D meson trigger itself and other particles), with respect to cases where
 378 the B decay particles are less collinear.

379 In the Monte Carlo closure test, this situation is reflected in the correlation distributions at reconstructed
 380 level, where the topological selection is applied, while it does not occur at kinematic level. Hence, in
 381 the reconstructed/kinematic ratio, the distribution would show an excess for $\Delta\phi = 0$ (due to the favoured
 382 decays with small opening angle), which is then compensated by a depletion for larger values of $\Delta\phi = 0$

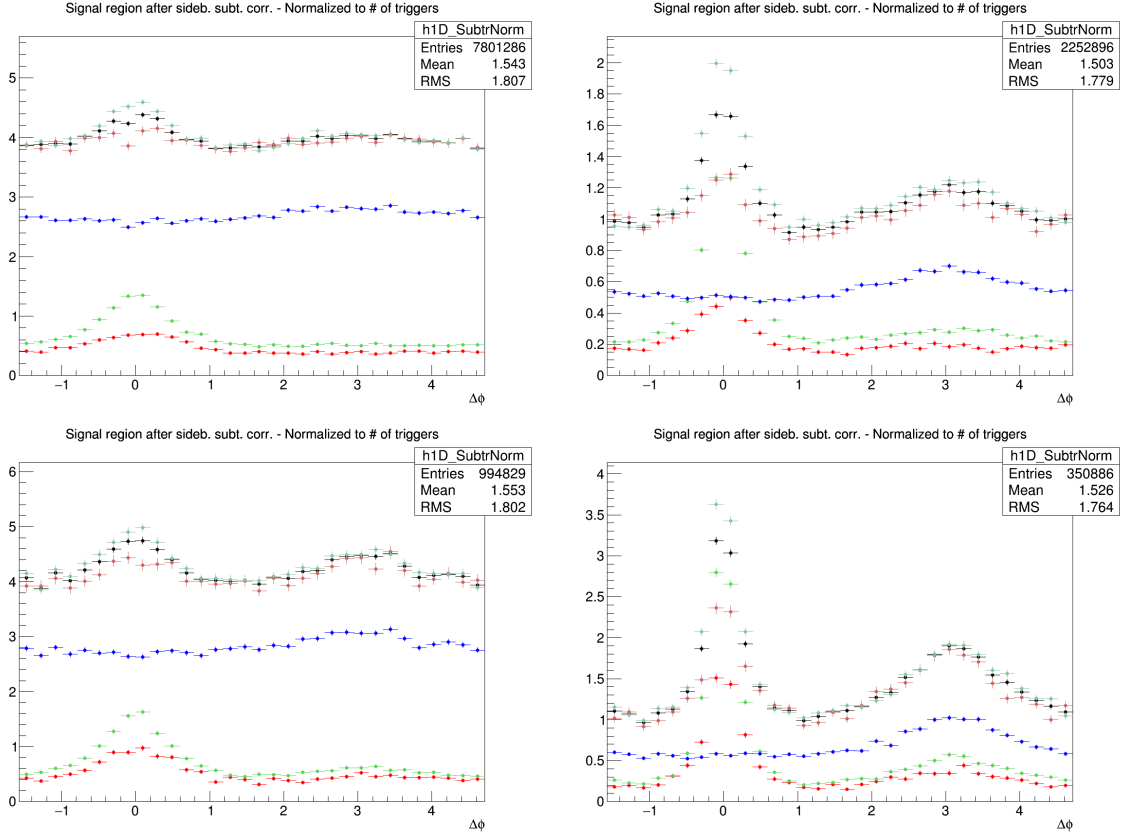


Figure 15: D^0 -hadrons azimuthal correlation distribution obtained from Monte Carlo, at reconstructed step. Black points: All D^0 -all hadrons, normalized by all D^0 triggers; light red points: D^0 from c-hadrons from c, normalized by c- D^0 triggers; dark red points: D^0 from c-all hadrons, normalized by c- D^0 triggers; light green points: D^0 from b-hadrons from b, normalized by b- D^0 triggers; dark green points: D^0 from b-all hadrons, normalized by b- D^0 triggers; blue points: All D^0 -hadrons from light quarks, normalized by all D^0 triggers. The panels show the ranges: $3 < p_T(D) < 5 \text{ GeV}/c$, $0.3 < p_T(\text{assoc}) < 1 \text{ GeV}/c$ (top-left); $3 < p_T(D) < 5 \text{ GeV}/c$, $p_T(\text{assoc}) > 1 \text{ GeV}/c$ (top-right); $8 < p_T(D) < 16 \text{ GeV}/c$, $0.3 < p_T(\text{assoc}) < 1 \text{ GeV}/c$ (bottom-left); $8 < p_T(D) < 16 \text{ GeV}/c$, $p_T(\text{assoc}) > 1 \text{ GeV}/c$ (bottom-right).

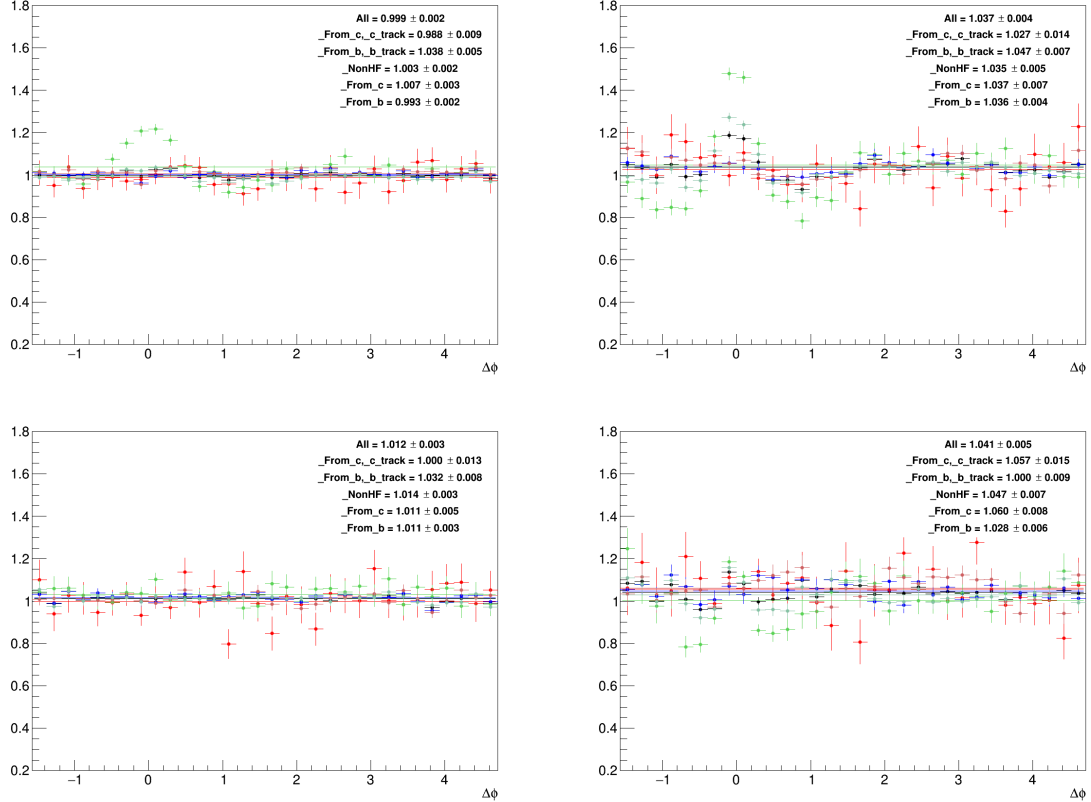


Figure 16: Ratios of fully corrected azimuthal correlation plots at reconstructed level over azimuthal correlation plots at kinematic level, in the two D^0 p_T bins, for the different associated p_T ranges. Black points: All D^0 -all hadrons, normalized by all D^0 triggers; light red points: D^0 from c-hadrons from c, normalized by c- D^0 triggers; dark red points: D^0 from c-all hadrons, normalized by c- D^0 triggers; light green points: D^0 from b-hadrons from b, normalized by b- D^0 triggers; dark green points: D^0 from b-all hadrons, normalized by b- D^0 triggers; blue points: All D^0 -hadrons from light quarks, normalized by all D^0 triggers. The panels show the ranges: $3 < p_T(D) < 5 \text{ GeV}/c$, $0.3 < p_T(\text{assoc}) < 1 \text{ GeV}/c$ (top-left); $3 < p_T(D) < 5 \text{ GeV}/c$, $p_T(\text{assoc}) > 1 \text{ GeV}/c$ (top-right); $8 < p_T(D) < 16 \text{ GeV}/c$, $0.3 < p_T(\text{assoc}) < 1 \text{ GeV}/c$ (bottom-left); $8 < p_T(D) < 16 \text{ GeV}/c$, $p_T(\text{assoc}) > 1 \text{ GeV}/c$ (bottom-right).

(corresponding to B decays with larger angles, which are disfavoured). These structures are prominent at low $D^0 p_T$, where the topological cuts are tighter, and tend to disappear at higher p_T , where the selections are released. They are also larger in the higher associated track p_T ranges, where the fraction of B-hadron decay tracks dominate the overall correlation distributions.

The data correlation distribution need to be corrected for this bias, and in particular for the enhancement of b-origin correlation pairs at the centre of the near side region, which would influence the near-side peak features. In order to do this, the amount of the b-origin excess is evaluated from the Reco/Kine ratio, by considering the b- D^0 -all tracks case (dark green points). The excess at Reco level (affecting data) is quantified as a $\Delta\varphi$ modulation **modul** for the five points an each side of the $\Delta\varphi = 0$ value (or, equivalently, on the first five points of the reflected distributions, which start from $\Delta\varphi = 0$). This is done separately in each p_T range. Then, the correction is done by applying this modulation to the data correlation distributions, but taking into account that only the correlation entries from $B \rightarrow D$ are affected, while the $c \rightarrow D$ correlations need to be left unaltered. In particular, it has to be considered that:

- On data, the $B \rightarrow D$ correlation pairs are only a fraction ($1 - f_{\text{prompt}}$) of the total.
- The amplitude of $B \rightarrow D|_{\text{amplit}}$ correlation pattern is different (greater) than the amplitude of the $c \rightarrow D|_{\text{amplit}}$ correlation pattern:

Thus, the following equation is applied to get the corrected $C(\Delta\varphi)_{\text{corr}}$ data points starting from the raw ones, $C(\Delta\varphi)_{\text{raw}}$:

$$C(\Delta\varphi)_{\text{corr}} = C(\Delta\varphi)_{\text{raw}} \cdot \left[\frac{c \rightarrow D|_{\text{amplit}}}{(B + c) \rightarrow D|_{\text{amplit}}} \cdot f_{\text{prompt}} + \frac{B \rightarrow D|_{\text{amplit}}}{(B + c) \rightarrow D|_{\text{amplit}}} \cdot (1 - f_{\text{prompt}}) \cdot \frac{1}{\mathbf{modul}} \right] \quad (3)$$

where $(B + c) \rightarrow D|_{\text{amplit}} = c \rightarrow D|_{\text{amplit}} \cdot f_{\text{prompt}} + B \rightarrow D|_{\text{amplit}} \cdot (1 - f_{\text{prompt}})$, and where the two amplitudes are evaluated from the Monte Carlo distributions of Figure 15 at reconstructed level (so, including the bias), and f_{prompt} with the procedure described in 3.3.5. Applying the **modul** factor to the beauty part of the data correlation distributions brings its value back to the generated level case, effectively removing the bias. The effect of the correction is a shift of the data points in the near-side region (in general, downward in the first and second points, the upward in the others). The maximum value of the shift is of about 5%, at the centre of the near-side peak, for the lowest D-meson p_T range ($3 < p_T < 5 \text{ GeV}/c$) and the highest associated track p_T range ($p_T > 3 \text{ GeV}/c$). The typical values are instead of a couple of percentage points. The correction is zero in the highest D-meson p_T range. To take into account for possible inaccuracies in the definition of the modulations, or in their rescaling, a systematic uncertainty is applied on the corrected data points, with value $|C(\Delta\varphi)_{\text{corr}} - C(\Delta\varphi)_{\text{raw}}| / \sqrt{12}$, on each side of the data points affected by the bias (symmetric uncertainty).

413 **3.3.4 Secondary track contamination**

414 The secondary tracks inside the associated track sample, due to interaction of primary track with the de-
 415 tector material or to decays of strange hadrons, are mostly removed by the DCA cuts applied during the
 416 cut selection phase ($DCA(xy) < 1 \text{ cm}$, $DCA(z) < 1 \text{ cm}$). Anyway, a small fraction of secondary tracks
 417 survives this cut, and the data correlation distributions have to be corrected for this residual contami-
 418 nation. The fraction of surviving secondary tracks is evaluated via a study on the LHC17d2a_fast_new
 419 sample, by counting the number of tracks accepted by the selection whose corresponding generated-
 420 level track doesn't satisfy the `IsPhysicalPrimary()` call, and dividing this number by the total number
 421 of accepted tracks. The outcome of the check is reported in Figure 17. As it's visible, no more than
 422 5% secondary tracks pass the selection. Moreover, the fraction of residual secondary tracks is flat along
 423 the $\Delta\varphi$ axis, as shown, for exemplary p_T regions, in Figure 18, where the inhomogeneities are always
 424 below 1%. For this reason, it is possible to directly scale the data correlation distributions by their purity
 425 fraction (i.e. 1 - secondary contamination). This is done with an associated p_T dependence, due to the
 426 increase of the purity with the track p_T , while the purity fraction is taken flat versus the D-meson p_T .
 427 The purity values that were chosen are the following:

- 428 – $p_T(\text{assoc}) > 0.3 \text{ GeV}/c : 0.958$
- 429 – $p_T(\text{assoc}) > 1 \text{ GeV}/c : 0.973$
- 430 – $0.3 < p_T(\text{assoc}) < 1 \text{ GeV}/c : 0.953$
- 431 – $1 < p_T(\text{assoc}) < 2 \text{ GeV}/c : 0.969$
- 432 – $2 < p_T(\text{assoc}) < 3 \text{ GeV}/c : 0.982$
- 433 – $p_T(\text{assoc}) > 3 \text{ GeV}/c : 0.990$

434 It was also verified with the same Monte Carlo study that applying the DCA selection rejects less than
 435 0.2% primary tracks (tagged as false positives) from the associated track sample, again with a flat az-
 436 imuthal distribution, inducing hence a fully negligible bias on the data correlation distributions. This is
 437 shown in Figure 19. This was also verified for specific charm-origin and beauty-origin tracks, due to
 438 their larger DCA with respect to primary tracks from light quarks. In this case, the fraction of rejected
 439 charm and beauty tracks stays below 1% in all the kinematic ranges apart from the associated track p_T
 440 regions 0.3-1 and $> 0.3 \text{ GeV}/c$, where the rejection can be as high as 2%. In these kinematic ranges,
 441 though, the data correlation distributions are dominated by non-heavy-flavour tracks, as it was verified
 442 from the simulations, hence the overall bias is still contained below 1%, thus negligible.

443 These studies were performed on an enriched Monte Carlo sample, which could not fully reproduce
 444 the relative abundancies of the species. Anyway, for events with a reconstructed D-meson, this bias is
 445 expected to be minor, and only these events are used in the data analysis. In any case, the percentages
 446 obtained from the study were found to be consistent within 1% with the outcome of the studies for the
 447 p-Pb 2013 analysis, which reassures us on the full validity of these results.

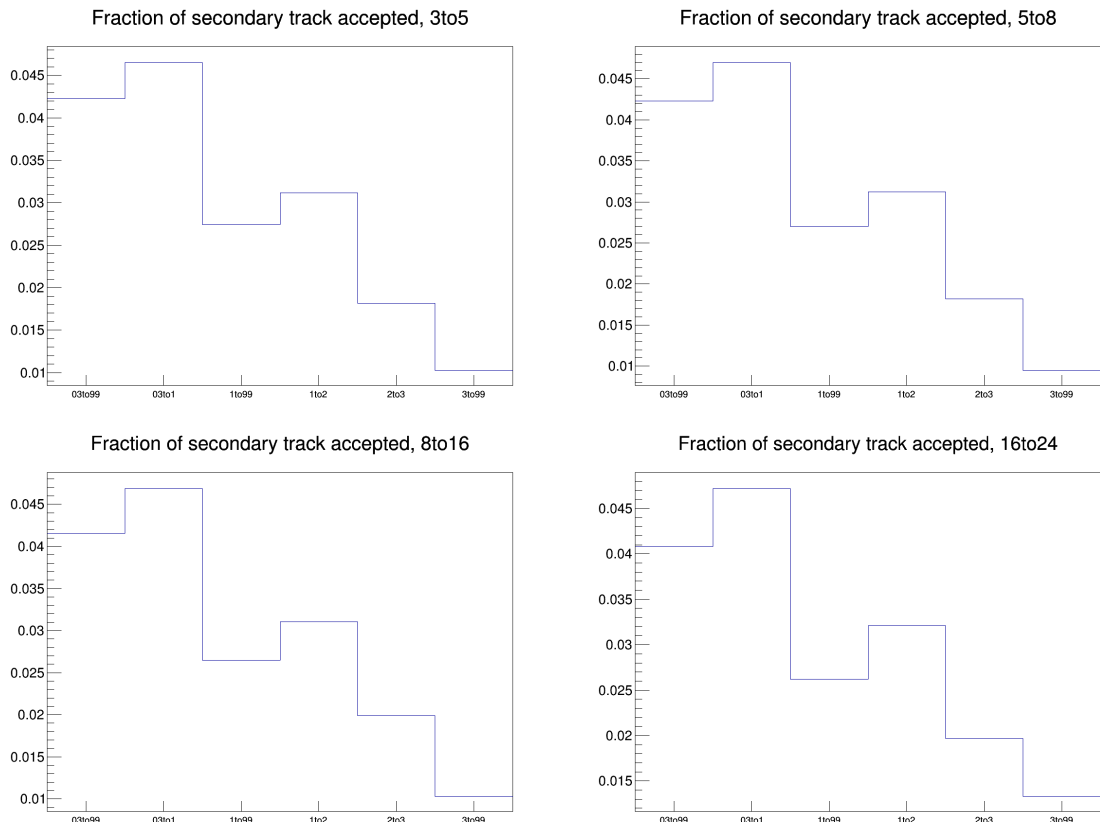


Figure 17: Fraction of secondary tracks over total amount of tracks which pass the DCA selection. The four panel show the fractions for the D-meson p_T ranges: 3-5, 5-8, 8-16, 16-24, respectively. Inside each panel, the associated track p_T ranges are shown on the x -axis.

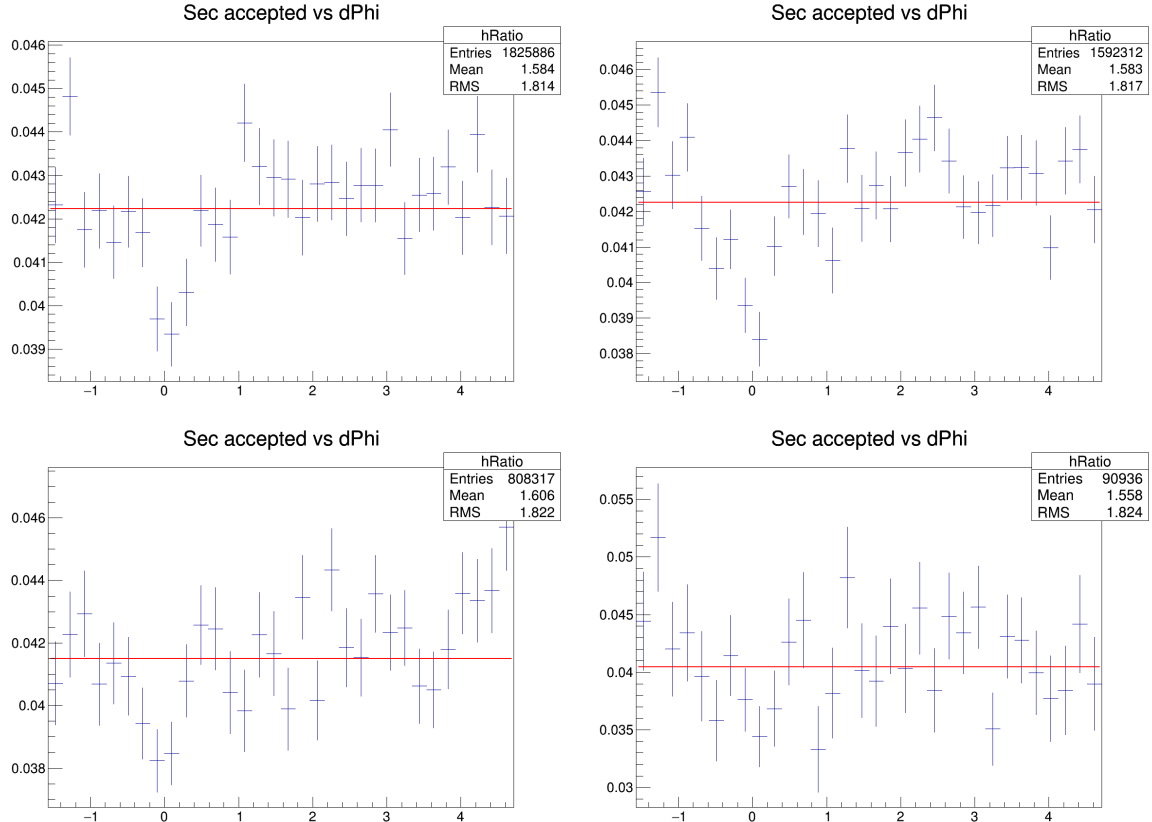


Figure 18: $\Delta\phi$ dependence of the fraction of secondary tracks in the D^0 - h correlation distributions. The four panel show the fractions for the D -meson p_T ranges: 3-5, 5-8, 8-16, 16-24, respectively. The associated track p_T ranges are the integrated one, i.e. $p_T > 0.3 \text{ GeV}/c$.

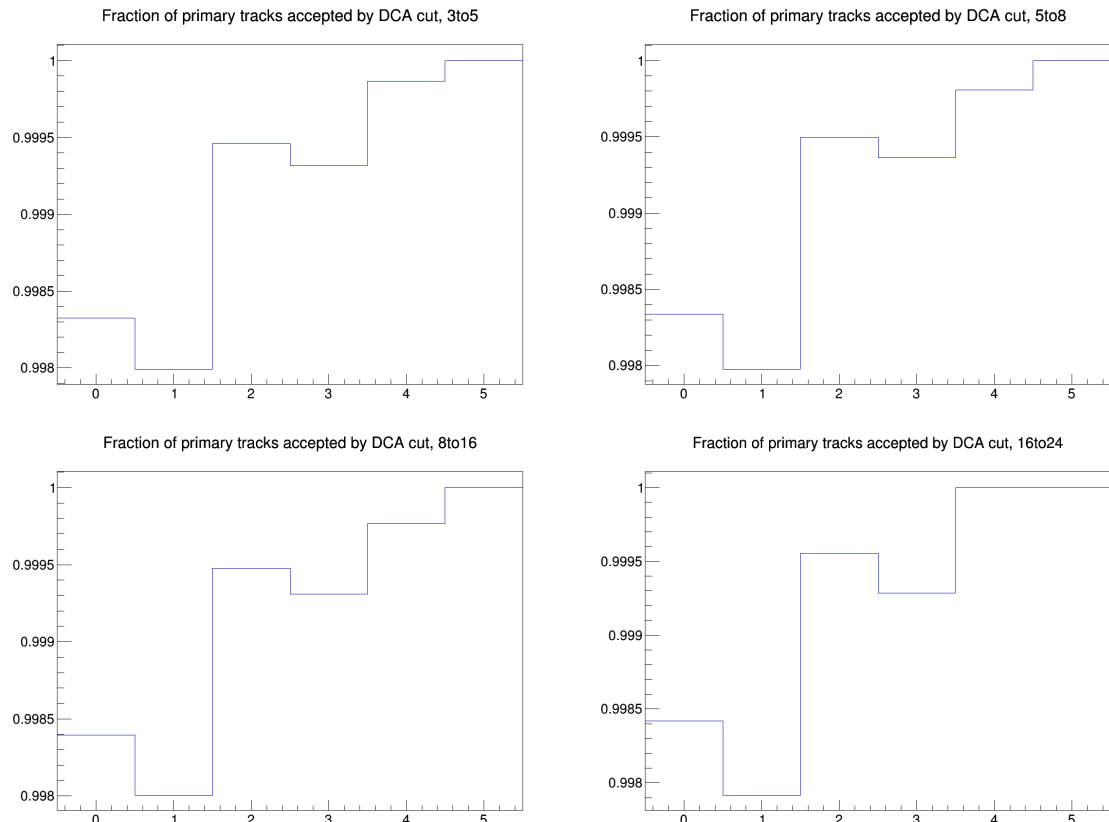


Figure 19: Fraction of primary tracks rejected by the DCA selection. The four panel show the fractions for the D-meson p_T ranges: 3-5, 5-8, 8-16, 16-24, respectively. Inside each panel, the associated track p_T ranges are shown on the x -axis.

448 **3.3.5 Beauty feed-down**

449 The contribution of correlations of D meson from b-hadron decay is subtracted from the data correlation
 450 distributions as:

$$\tilde{C}_{\text{prompt D}}(\Delta\phi) = \frac{1}{f_{\text{prompt}}} \left(\tilde{C}_{\text{inclusive}}(\Delta\phi) - (1 - f_{\text{prompt}}) \tilde{C}_{\text{feed-down}}^{\text{MC templ}}(\Delta\phi) \right). \quad (4)$$

451 In the above equation, $\tilde{C}_{\text{inclusive}}(\Delta\phi)$ and $\tilde{C}_{\text{prompt D}}(\Delta\phi)$ are per-trigger azimuthal correlation distribu-
 452 tions before and after feed-down contribution subtraction, f_{prompt} is the fraction of prompt D meson
 453 and $\tilde{C}_{\text{feed-down}}^{\text{MC templ}}$ is a template of the azimuthal correlation distribution for the feed-down component ob-
 454 tained from home-made Monte Carlo simulation at generated level, using PYTHIA6 with Perugia2011
 455 tune. In order to avoid biases related to the different event multiplicity in real and simulated events,
 456 the correlation distribution was shifted to have its minimum coinciding with the baseline of the data
 457 azimuthal-correlation distribution before feed-down subtraction.

458 The value of f_{prompt} (Figure 20), which depends on D-meson species and varies as a function of the p_T ,
 459 is estimated on the basis of FONLL predictions for the production of feed-down D mesons at central
 460 rapidity, in pp collisions at $\sqrt{(s)} = 5$ TeV, and using the reconstruction efficiency of prompt and feed-
 461 down D mesons, following the so-called N_b approach defined in [1]. Typical values are about 8-10%
 462 for the D^0 , about 4-7% for the D^+ and about 5-8% for the D^{*+} . The procedure adopted is the same
 463 as what done in the past analysis [6]: however, in p-Pb, in order to consider a possible non-zero v_2 -
 464 like modulation of the baseline, a range of $0 < v_2 < 0.2$ values for tracks and for secondary D mesons
 465 is considered for the systematic uncertainty evaluation (using an hypothesis of no modulation for both
 466 cases for central values).

467 Examples of the PYTHIA templates used for the feed-down contribution subtraction are shown in Figures
 468 21 (Figure 22 shows the same templates but for prompt D mesons).

469 The feed-down subtraction was performed after rescaling the data correlation distributions for the purity
 470 fraction, and correcting them by the near-side modulation induced by the bias on the B decay topology.

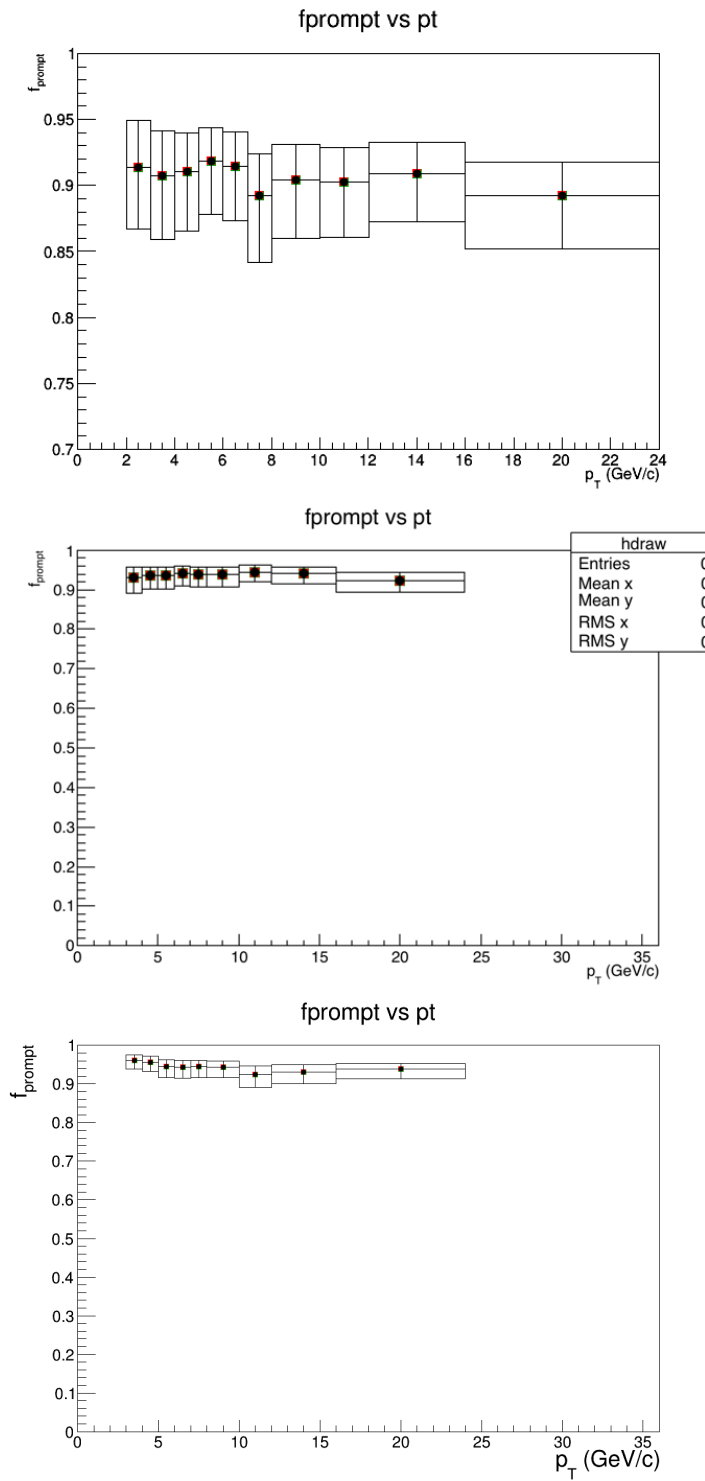


Figure 20: f_{prompt} as a function of the p_T for D^0 (top), D^{*+} (mid) and D^+ (bottom) estimated on the basis of FONLL predictions

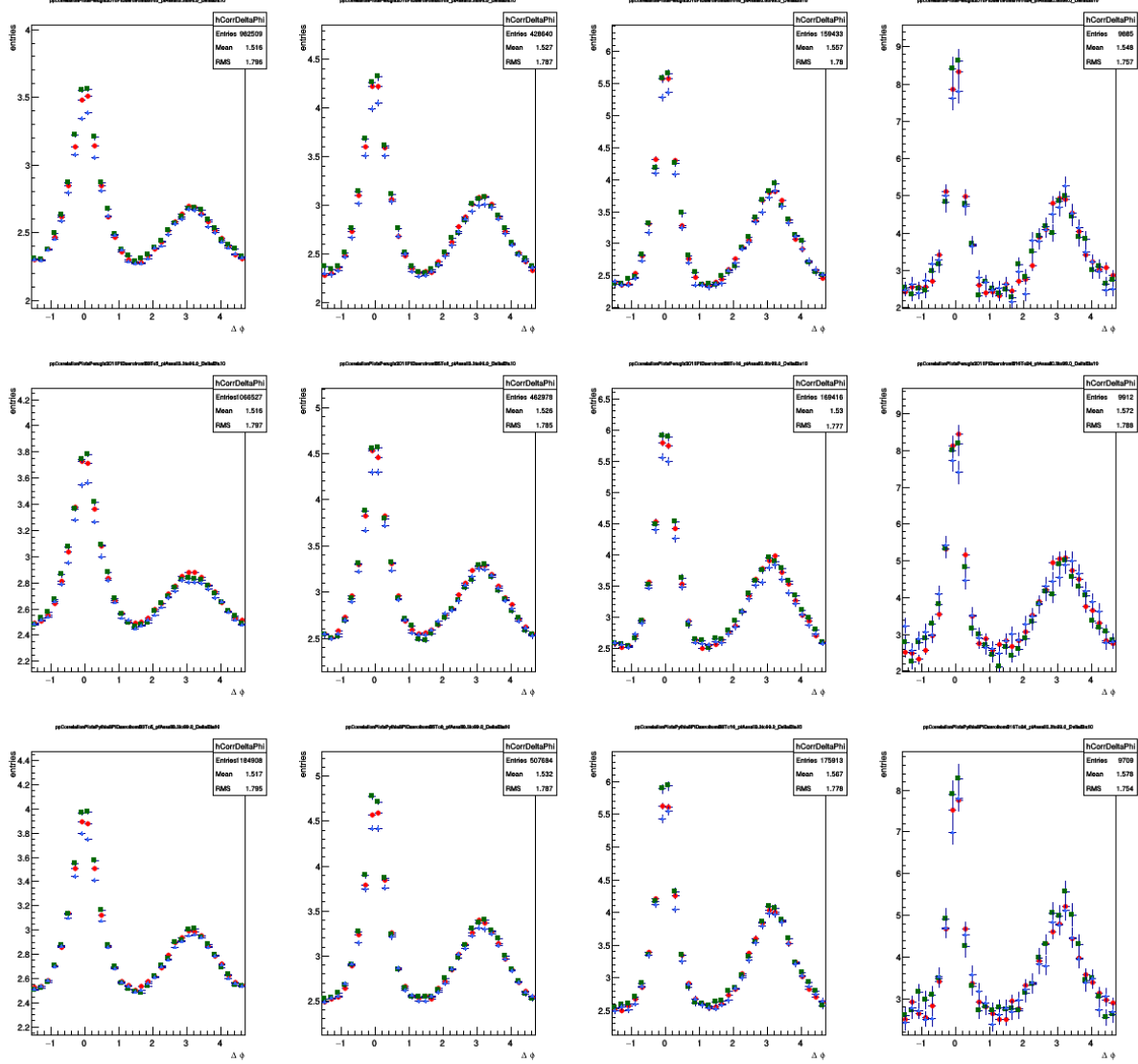


Figure 21: Azimuthal correlation distribution between D meson from b-hadron decay and charged particles obtained from Monte Carlo simulations based on Pythia-Perugia2010 tune (row1), Pythia-Perugia2011 tune (row2), Pythia8 tune 4C (row3) for associated track $p_T > 0.3$ GeV/ c and D-meson p_T ranges: 3-5, 5-8, 8-16, 16-24 GeV/ c . D⁰ in blue, D⁺ in green, D^{*+} in red.

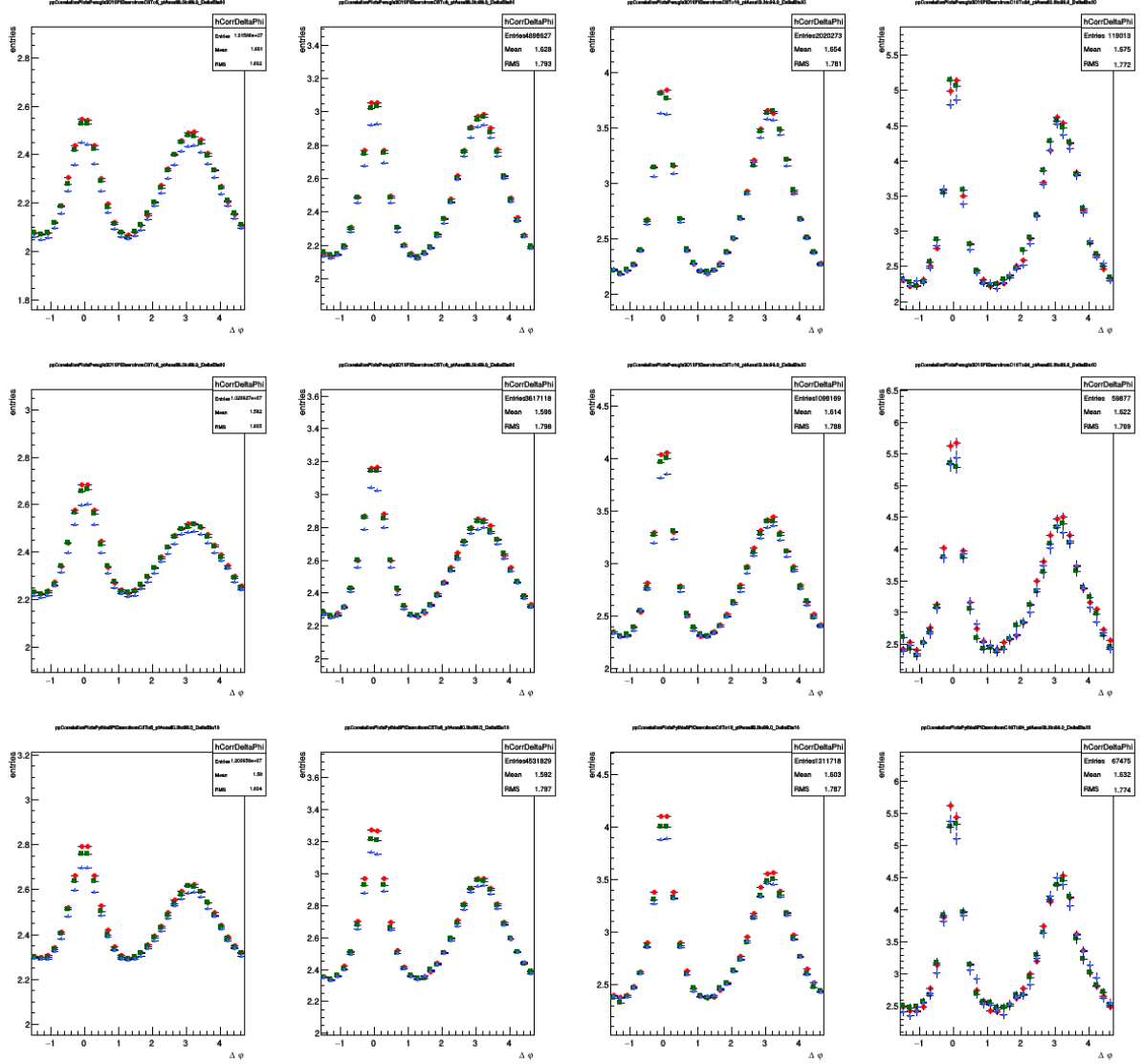


Figure 22: Azimuthal correlation distribution between prompt D meson and charged particles obtained from Monte Carlo simulations based on Pythia-Perugia2010 tune (row1), Pythia-Perugia2011 tune (row2), Pythia8 tune 4C (row3) for associated track $p_T > 0.3 \text{ GeV}/c$ and D-meson p_T ranges: 3-5, 5-8, 8-16, 16-24 GeV/c . D⁰ in blue, D⁺ in green, D^{*+} in red.

4 Systematic uncertainties on $\Delta\phi$ correlation distributions

4.1 Uncertainty on S and B extraction

The systematic uncertainty for the D meson yield extraction was determined separately for the three mesons. It was obtained by evaluating the value of the signal candidate from the invariant mass spectra with the following differences with respect to the standard approach:

- Changing the background fit function, for D^0 and D^+ (tried with polynomials of 1st and 2nd order) and for D^{*+} (tried with polynomials of 2nd order and a power function);
- Changing the range in which the signal is extracted from the Gaussian fit;
- Reducing the range of invariant mass axis in which the signal region is defined (and S and B are extracted);
- Rebinning the invariant mass distributions before the fit for D^0 and D^+
- Extracting S and B via integral of the fit functions or B via bin counting and S via integral of the Gaussian function.

Both the value of the yield and the sidebands correlations normalization factor are affected by changing the yield extraction approach, while the rest of the procedure to extract the azimuthal correlation distribution is the same as in the standard analysis. The fully corrected azimuthal correlation plots were evaluated, for each of these approaches, in all D meson p_T bins and for each value of associated tracks p_T threshold. The ratios of the correlation distributions obtained with the standard yield extraction procedure and by differentiating the approach were evaluated. From the average of these ratios, which are found to be flat versus $\Delta\phi$, a systematic uncertainty can be extracted, which was taken of 1% for $3 < p_T(D) < 16 \text{ GeV}/c$ and of 2% in $16 < p_T(D) < 24 \text{ GeV}/c$ (3% for D^0). No dependence versus the associated track p_T was assumed, since from a physics point of view we don't expect a modification of the signal and sideband values to have a dependence of this kind. Figures 23, show the ratios obtained by the above mentioned procedure for exemplary p_T ranges, which anyway span over the full kinematic ranges analyzed, for D^0 -h correlations. Figures 24 and 25 show the same ratios for D^{*+} -h, D^+ -h as well.

4.2 Uncertainty on background correlation shape

The systematic uncertainty for the subtraction of the background correlations includes the effects due to a potentially biased description of the background correlation shape, which is evaluated from of the sidebands correlations. In particular, the background correlation shape could present some hidden invariant mass dependence. To estimate this uncertainty, the invariant mass range of the sidebands definitions was varied with respect to the default values. For the D^0 meson, the usual range of the sidebands is 4 to 8 σ from the centre of the peak of the Gaussian fit and it was modified, for both sidebands to:

- inner half (4 to 6 σ from the centre of the peak);
- outer half (6 to 8 σ from the centre of the peak)
- extended to 4 to 10 σ (in case this is possible without exceeding the fitting range of the mass plots)

Slightly different variations, but with the same reasoning, were considered for the D^+ meson.

For the D^{*+} meson, the usual range of sideband in invariant mass spectra is 5 to 10 σ (only on the right side) from the centre of the peak of the Gaussian fit of the invariant mass spectra, and it was modified to:

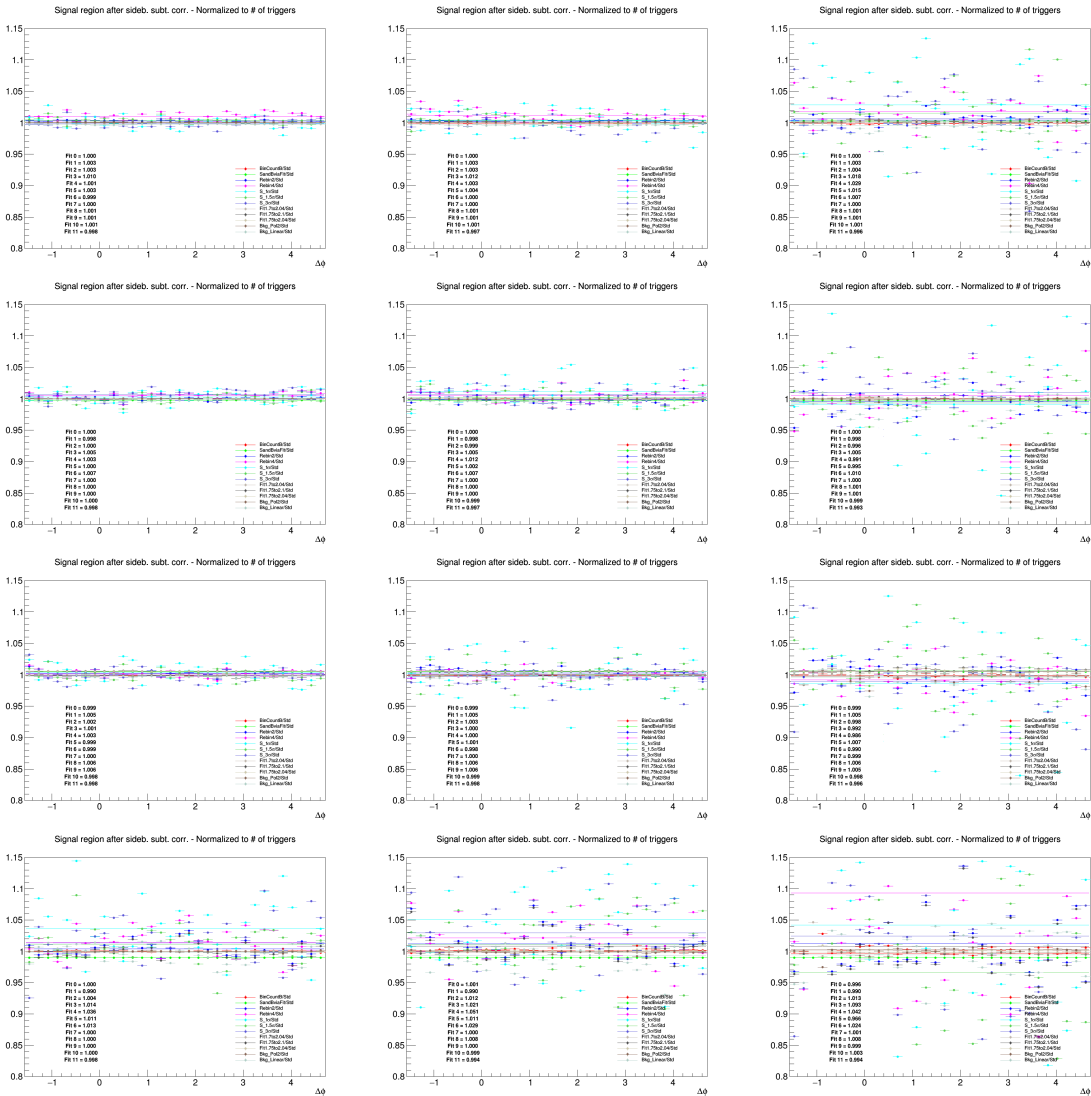


Figure 23: Ratios of D^0 - h correlation plots obtained changing S and B extraction procedure over those obtained with standard yield extraction procedure. Rows: $p_T(D^0)$ 3-5, 5-8, 8-16, 16-24 GeV/c . In each row, the panels show the associated track p_T ranges 0.3-1, 1-2, $>3 \text{ GeV}/c$, respectively.

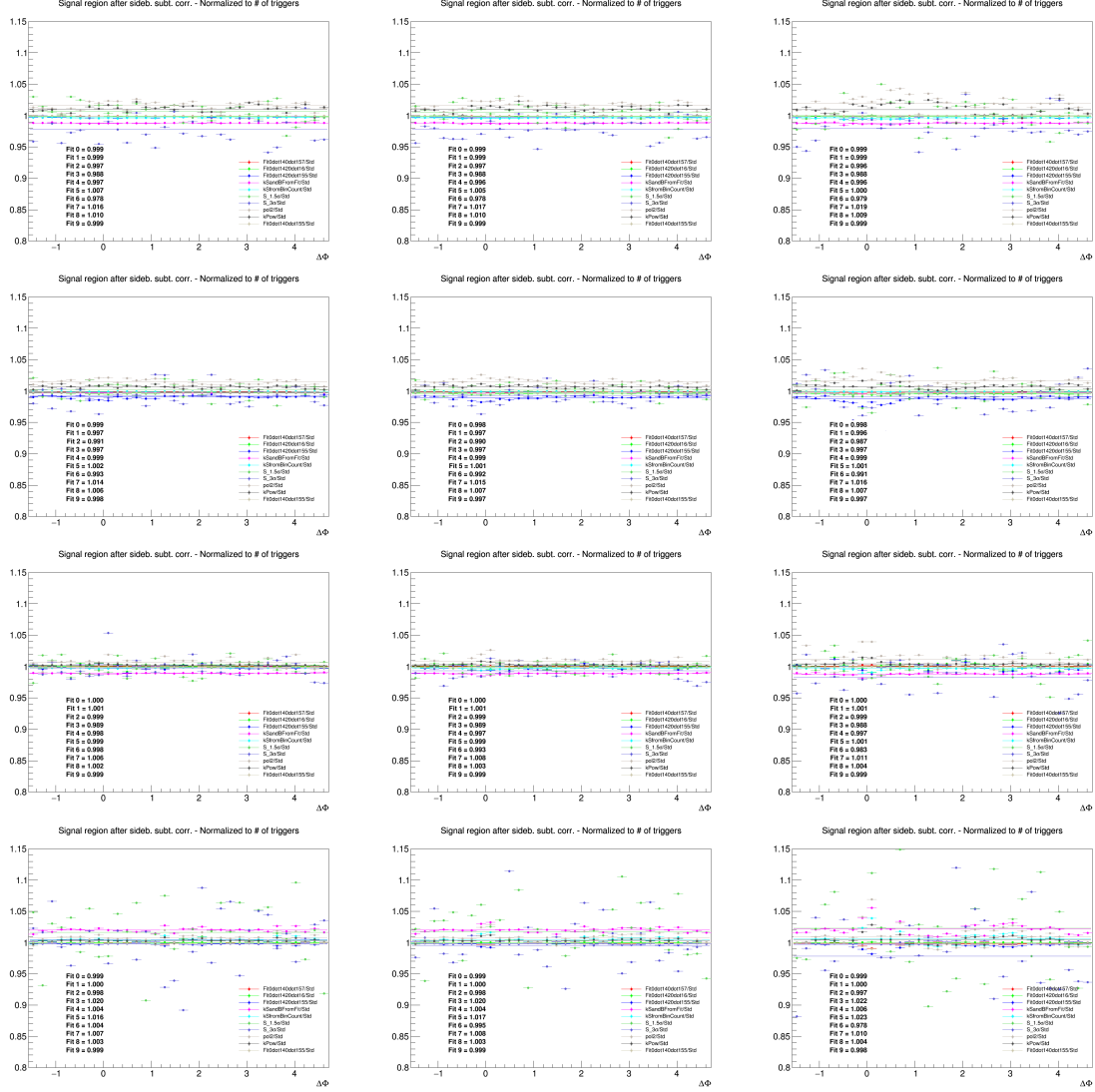


Figure 24: Ratios of D^{*+} - h correlation plots obtained changing S and B extraction procedure over those obtained with standard yield extraction procedure. Rows: $p_T(D^{*+})$ 3-5, 5-8, 8-16, 16-24 GeV/c . In each row, the panels show the associated track p_T ranges $>0.3 \text{ GeV}/c$, $0.3-1 \text{ GeV}/c$ and $>1 \text{ GeV}/c$, respectively.

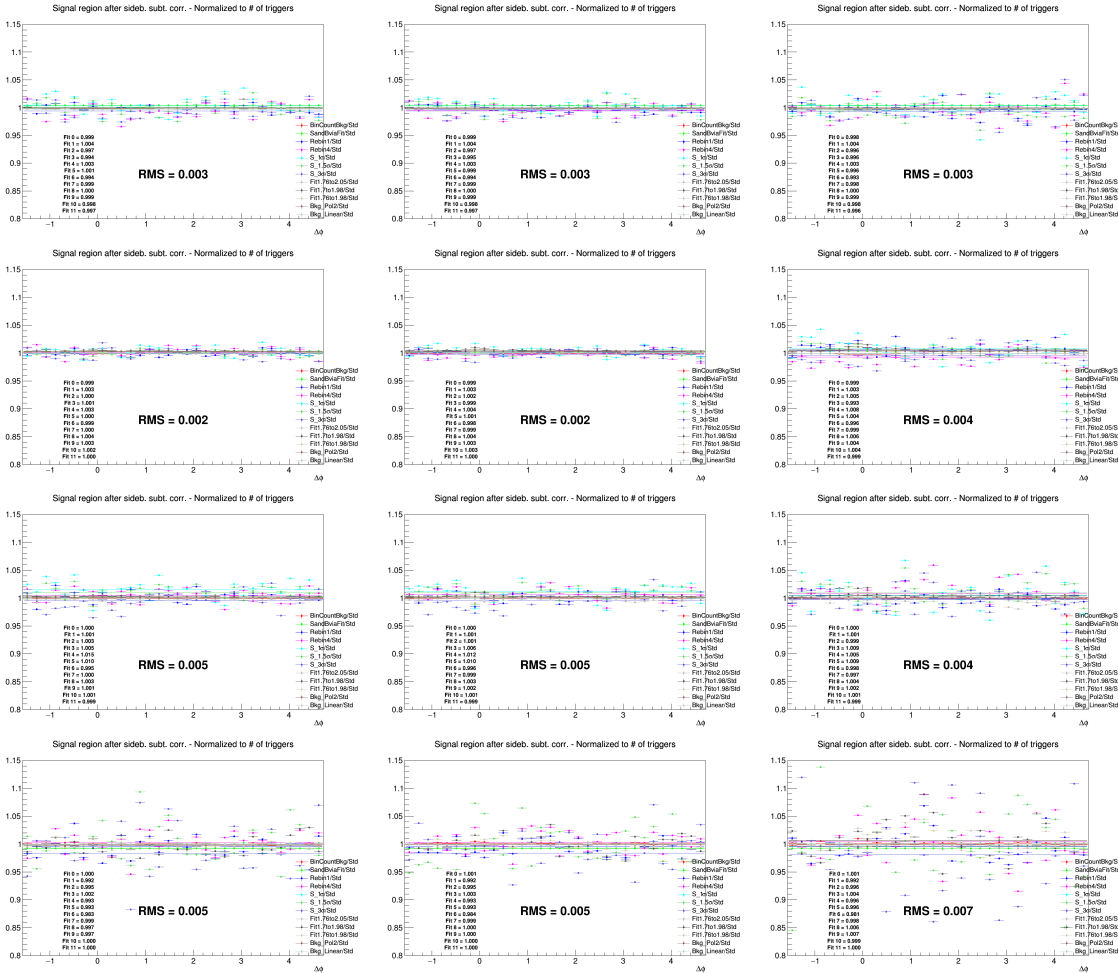


Figure 25: Ratios of $D^+ - h$ correlation plots obtained changing S and B extraction procedure over those obtained with standard yield extraction procedure. Rows: $p_T(D^+)$ 3-5, 5-8, 8-16, 16-24 GeV/ c . In each row, the panels show the associated track p_T ranges 0.3-1 GeV/ c , >0.3 GeV/ c , and >1 GeV/ c , respectively.

- inner half (5 to 8 σ from the centre of the peak);
- outer half (8 to 13 σ from the centre of the peak);
- extended to 5 to 13 σ from the centre of the peak;
- extended to 6 to 16 σ from the centre of the peak.

The rest of the procedure for the azimuthal correlations distribution was unchanged, and the ratios of the fully corrected azimuthal correlation plots obtained with the standard sidebands range and the correlation plots extracted with different sidebands definitions, were evaluated for each D-meson p_T bin and associated tracks p_T threshold. Results of this check are shown in Figures 26, 27 and 28 for D^0 , D^{*+} , D^+ respectively, for exemplary p_T ranges, spanning over the full kinematic regions analysis. From the values of the ratios extracted from the checks, which do not show any azimuthal dependence a systematic uncertainty for the background subtraction can be evaluated. Also no dependence versus the associated track p_T was assumed also in this case. The uncertainty was hence taken of 1% for $3 < p_T(D) < 16$ GeV/ c and 3% for $16 < p_T(D) < 24$ GeV/ c for the three D mesons.

4.3 Uncertainty on D-meson cut stability

To study the systematics due to the topological selections on the D meson, the cut variation approach was used. For each D-meson, alternate sets of released and tightened selection cuts were applied to extract the correlation distribution, varying in particular the cosine of the pointing angle, the maximum DCA among the daughter tracks and the product of the daughter track impact parameters. For each set of cuts new 2D (p_T vs multiplicity), D meson efficiency map was computed. In Figures 29, 30, 31 (for D^0 , D^{*+} and D^+ , respectively) the ratio of the different 1D efficiencies with the alternate cuts with respect to the default cut selection is chosen, to highlight how the different selections effectively varied the efficiency values, especially at low p_T , where cuts are more effective.

Figure 32, 33, 34 show the ratio of the correlation distributions with alternate cut sets over those with the standard approach, for exemplary p_T ranges covering the full kinematic region of interest for the analyses. The ratios are reasonably flat in $\Delta\phi$, hence a flat systematic was evaluated as systematic uncertainty from D-meson the cut variations. For the D^0 , the uncertainty was considered of 2% for all the p_T ranges of trigger and tracks analyzed. For the D^{*+} , the uncertainty was considered of 1.5% for $3 < p_T(D) < 8$ GeV/ c and of 1% for $8 < p_T(D) < 24$ GeV/ c . For the D^+ , the uncertainty was considered of 1% for $3 < p_T(D) < 16$ GeV/ c and of 3% for $16 < p_T(D) < 24$ GeV/ c .

4.4 Uncertainty on tracking efficiency evaluation

The systematic uncertainty for the tracking efficiency includes the effects related to the set of filtering cuts defined for the associated tracks selection (mainly requests on the quality of reconstructed tracks for the TPC and ITS detectors). This uncertainty was determined by repeating the full analysis using different selections for the cuts on the associated tracks with respect to the usual selection (TPC only tracks with at least 2 points in the ITS). The alternative selections were: pure TPConly selection, meaning TPC tracks with no requests on the number of hits in the ITS, and TPC+ITS selection, which requires filterbit 4 with, in addition, at least 3 points in the ITS, ITS refit and a hit in at least an SPD layer. The ratios of the azimuthal correlation distributions with different sets of tracks selection over distributions with standard selection were evaluated, and are shown in Figures 35 and 36 for D^0 -h correlations. Their values were used to determine a systematic uncertainty, which as the previous ones could be assigned flat in $\Delta\phi$, and which was estimated of 3% in all the ranges of p_T analyzed.

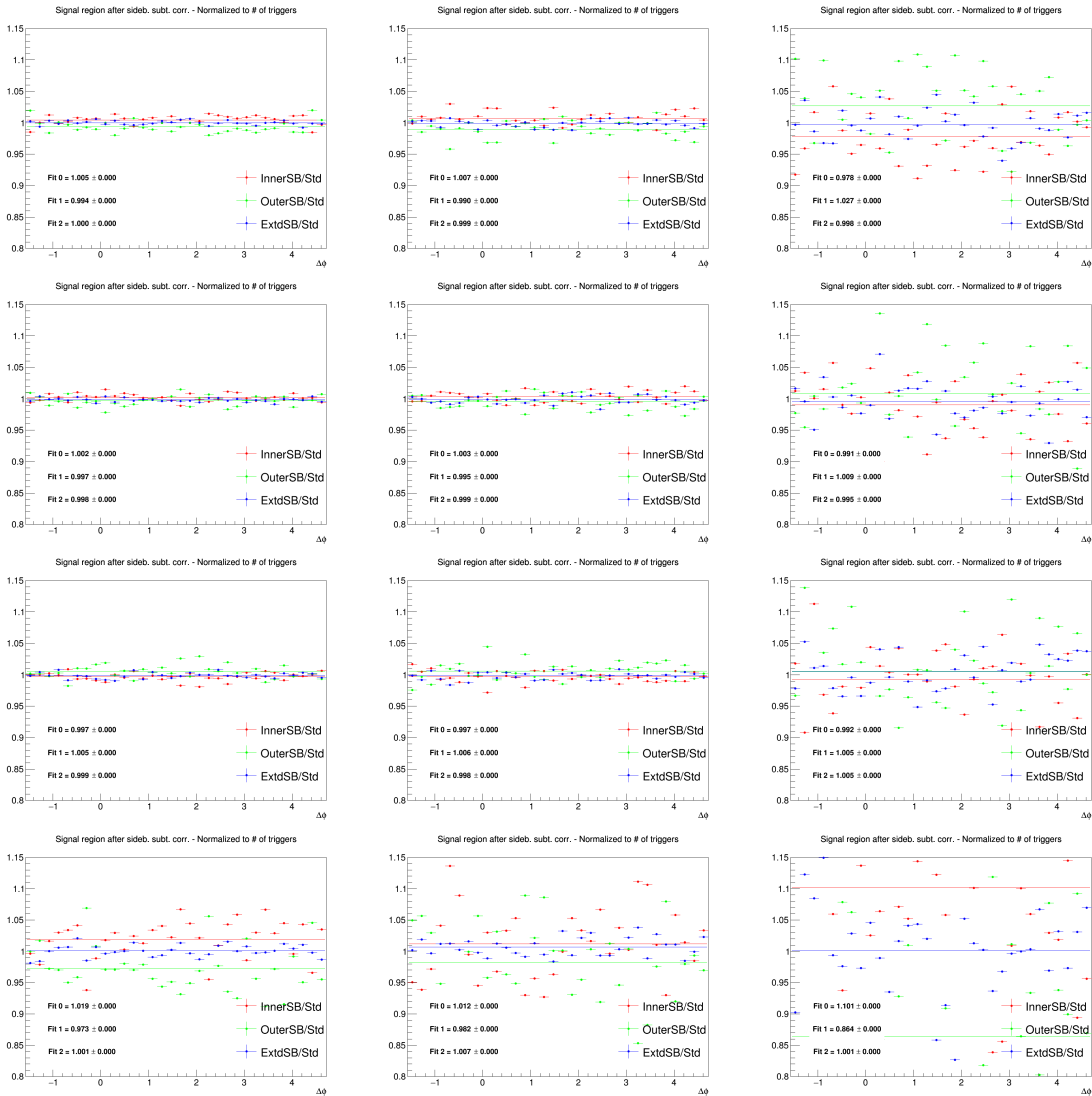


Figure 26: Ratios of D^0 - h correlation plots obtained by changing the sideband ranges over those obtained with standard sideband ranges. Rows: $p_T(D^0)$ 3-5, 5-8, 8-16, 16-24 GeV/ c . In each row, the panels show the associated track p_T ranges 0.3-1, 1-2, >3 GeV/ c , respectively.

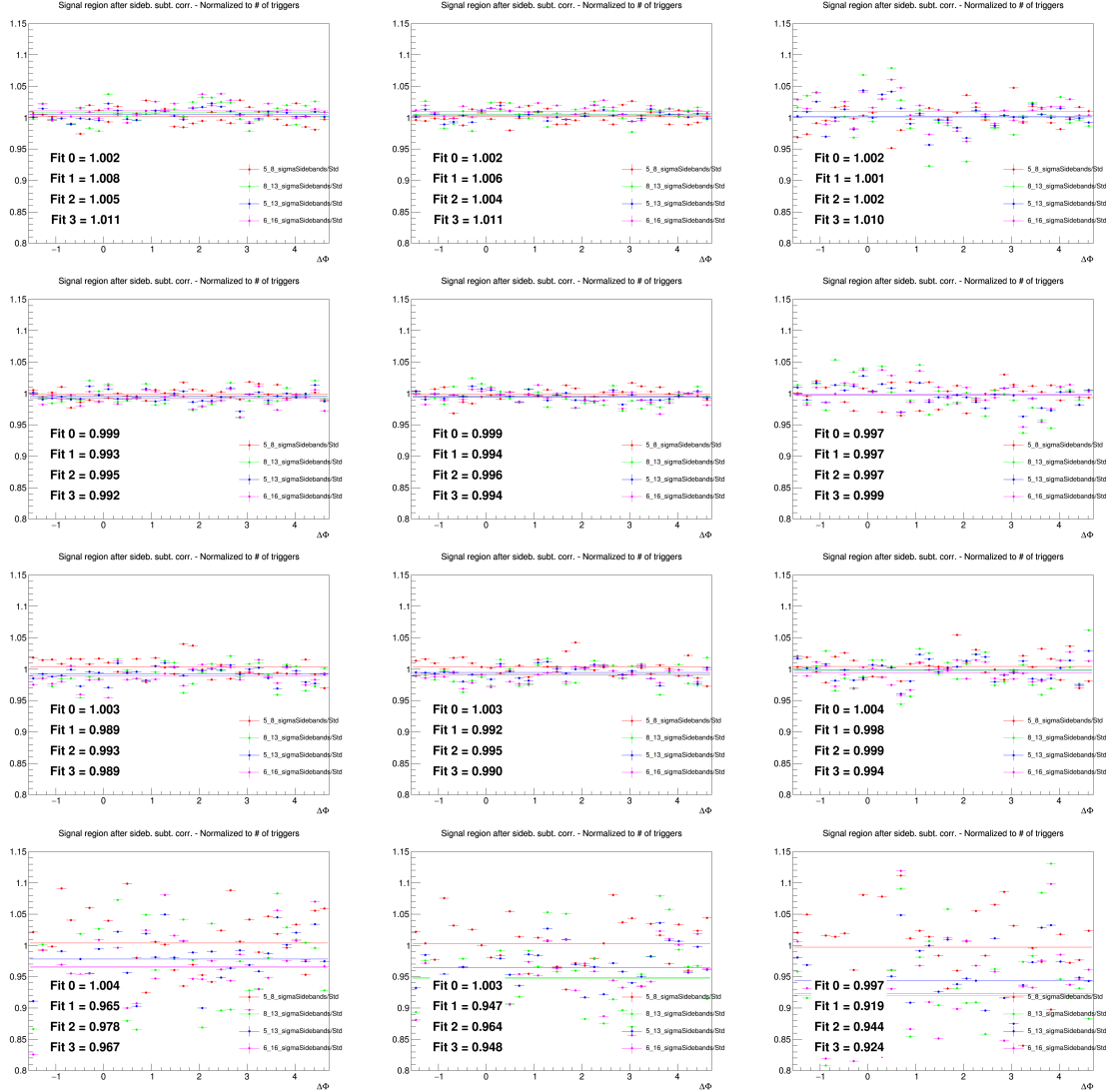


Figure 27: Ratios of D^*-h correlation plots obtained by changing the sideband ranges over those obtained with standard sideband ranges. Rows: $p_T(D^*)$ 3-5, 5-8, 8-16, 16-24 GeV/ c . In each row, the panels show the associated track p_T ranges 0.3-1, >0.3 GeV/ c and >1 GeV/ c , respectively.

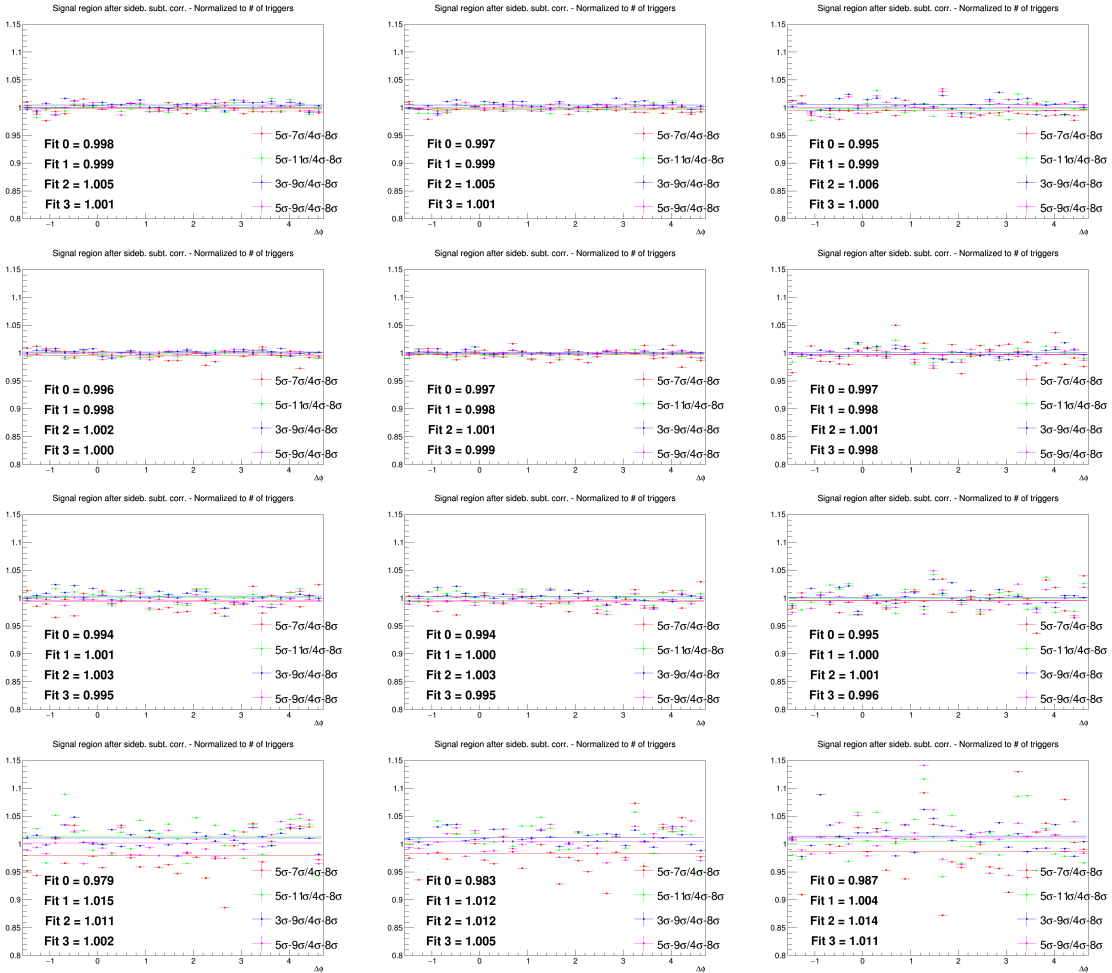


Figure 28: Ratios of D⁺-h correlation plots obtained by changing the sideband ranges over those obtained with standard sideband ranges. Rows: p_T(D⁺) 3-5, 5-8, 8-16, 16-24 GeV/c. In each row, the panels show the associated track p_T ranges 0.3-1, >0.3 GeV/c and >1 GeV/c, respectively.

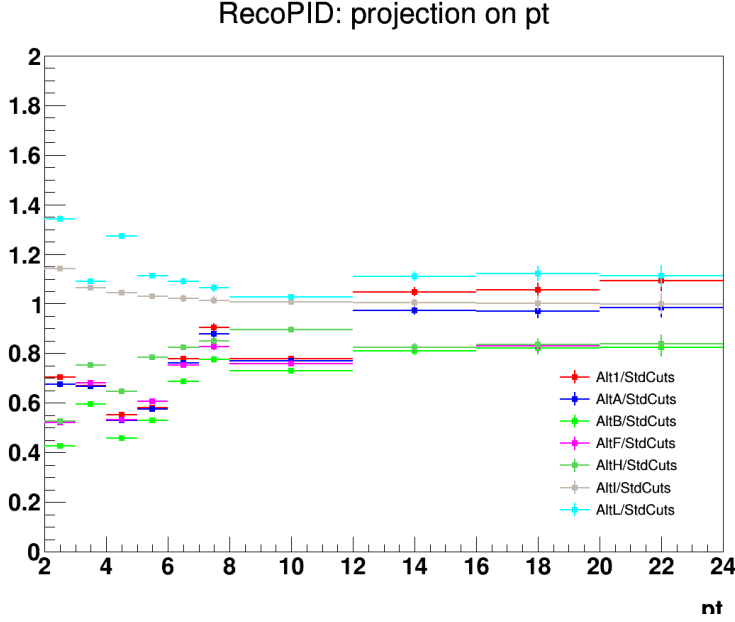


Figure 29: Ratio of D^0 efficiencies with alternate cut variations w.r.t. the standard cut used for the analysis.

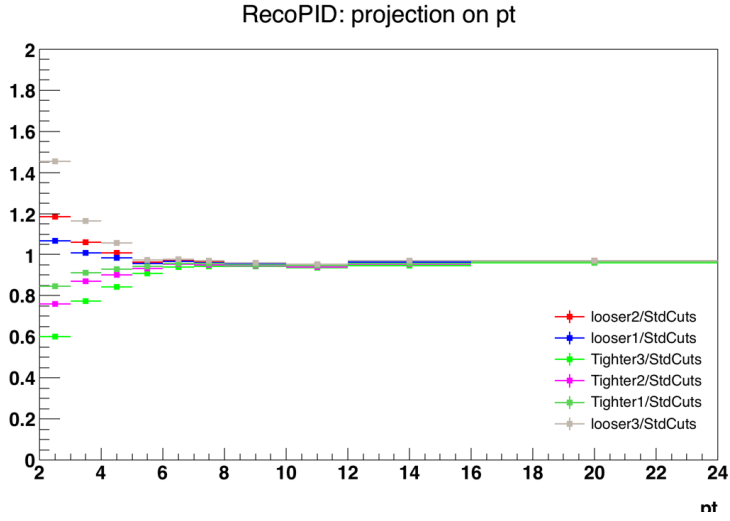


Figure 30: Ratio of D^{*+} efficiencies with alternate cut variations w.r.t. the standard cut used for the analysis.

550 4.5 Uncertainty on secondary particle contamination

551 Secondary particles, i.e. particles coming from strange hadrons decays or particles produced in inter-
 552 actions with the material, are expected to be tagged and removed by means of a distance of closest
 553 approach (DCA) from primary vertex cut. The uncertainty arising from the residual contamination of
 554 secondary tracks can be estimated from a Monte Carlo study, at reconstructed level. The number of
 555 primary/secondary tracks which are accepted/rejected from the DCA cut was determined for different
 556 values of the DCA selection, and the correlation distributions for the various cases were evaluated. The
 557 variations were done in the xy direction, where the DCA resolution is better, and the following cases
 558 were tried (in addition to the default 1 cm cut): 0.1 cm, 0.25 cm, 0.5 cm, filtering DCA cut (i.e. 2.4 cm).

559 Figure 37 shows the amount of secondary tracks which are accepted by the DCA cut, over the total
 560 number of tracks (primary and secondary) accepted by the selection, for the various DCA selections that
 561 were tried. This is shown for the exemplary case of $5 < p_T < 8 \text{ GeV}/c$ (there's no $p_T(D)$ dependence) and
 562 as a function of the associated track p_T ranges. Hence, this quantity represents the residual contamination

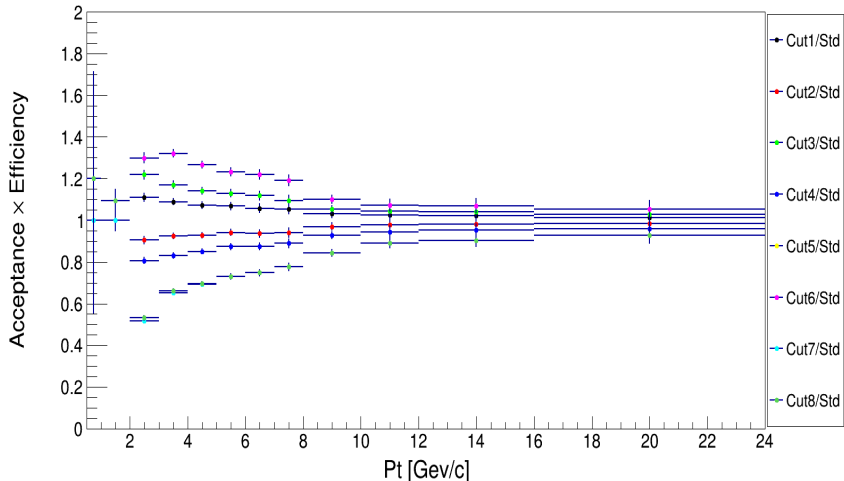


Figure 31: Ratio of D^+ efficiencies with alternate cut variations w.r.t. the standard cut used for the analysis.

of secondary tracks in our reconstructed track sample. From these values, the corresponding primary track purities (1-contamination) were extracted, in each of the momentum ranges. It was also verified that, for all the cut selections, the $\Delta\varphi$ distributions of the residual contaminations were flat within 1%.

As a second step of the procedure to verify the DCA cut stability, the D^0 -h data analysis was performed with all the different DCA selection (each time with the proper tracking efficiency map). After having extracted the correlation distributions, these were rescaled for the corresponding purities and compared with the purity-corrected correlation distributions obtained with the standard DCA selection. The ratios of the alternate selections over the standard selection, after the purity correction of both, are shown in Figures 38 and 39.

The ratios show a flat trend along the $\Delta\varphi$ axis and, in general, a discrepancy from the value of 1 of no more than 3% (the worst case being the 0.3-1 GeV/c range for the associated track). Hence, a flat and symmetric 3% systematical uncertainty on the evaluation of the secondary contamination was assigned on the base of this check in 0.3-1 GeV/c, reduced to 2.5% in > 0.3 GeV/c and to 1.5% for the other ranges. This amount also covers possible biases in the estimation of the purity (the $\Delta\varphi$ distribution of the residual contamination is always contained inside 1%, as previously said).

4.6 Uncertainty on feed-down subtraction

As described in the 3.3.5 section, the feed-down subtraction from the data distributions is performed by means of simulation templates of $B \rightarrow D$ -h correlation distributions from PYTHIA6 generator, with Perugia2011 tune, and considering the central value of f_{prompt} to extract the feed-down D-meson contribution. In order to evaluate a systematic uncertainty on this procedure, the feed-down subtraction procedure was repeated considering, together with PYTHIA6+Perugia2011 templates, also PYTHIA6+Perugia2010 and PYTHIA8 simulations. In each case, not only the central value of the measured f_{prompt} was considered to rescale the distributions, but also the maximum and minimum values of its total uncertainty.

Then, the envelope of nine the different cases obtained by varying the templates and the f_{prompt} assumption was considered, and a value of the systematics defined as the envelope spread divided by $\sqrt{3}$ was taken as systematic uncertainty. This uncertainty was assumed uncorrelated among the different $\Delta\varphi$ points.

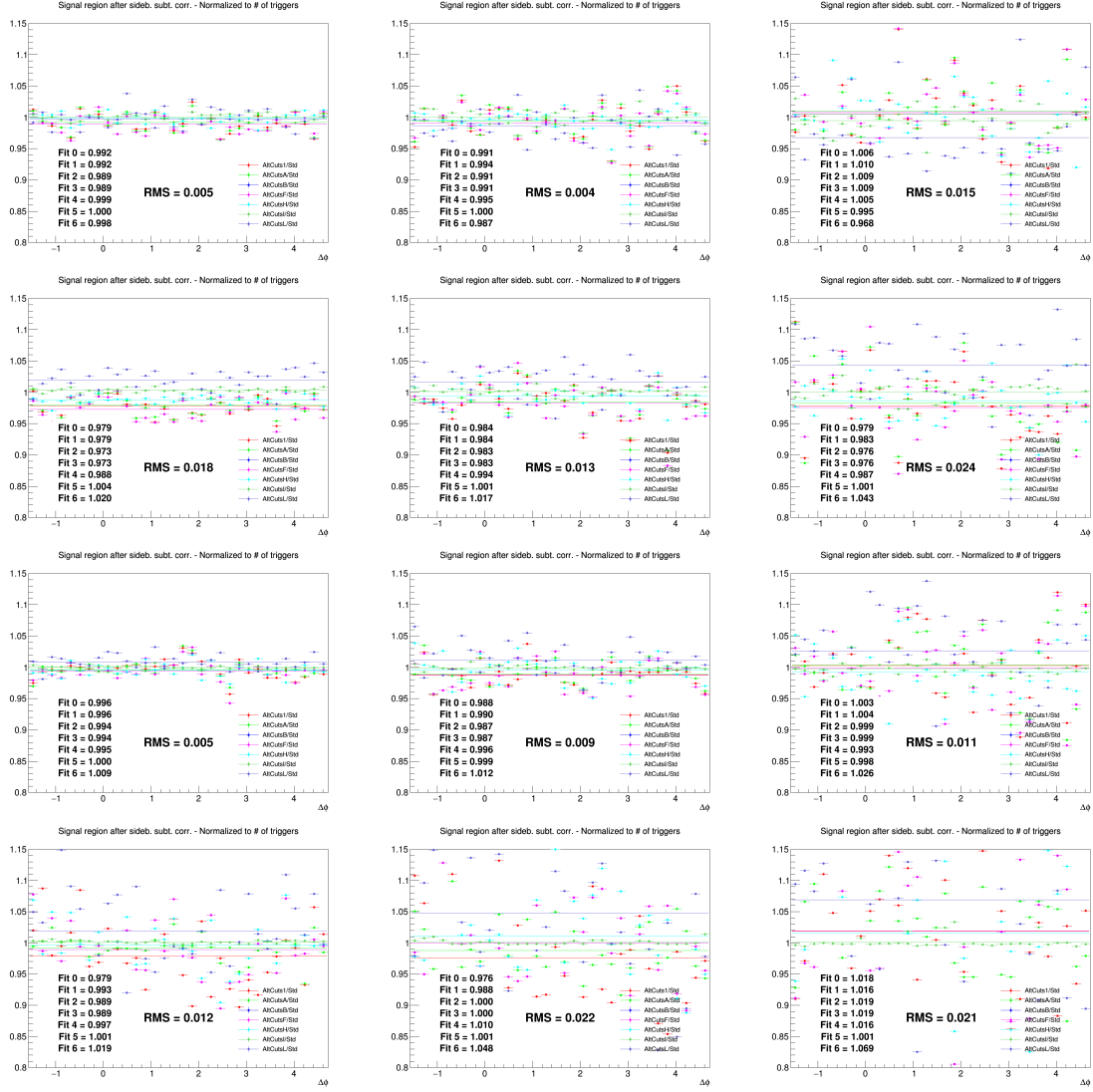


Figure 32: Ratios of D⁰-h correlation plots obtained with alternate D-meson cut sets over those obtained with standard selection. Rows: $p_T(D^0)$ 3-5, 5-8, 8-16, 16-24 GeV/ c . In each row, the panels show the associated track p_T ranges 0.3-1, 1-2, 2-3 GeV/ c , respectively.

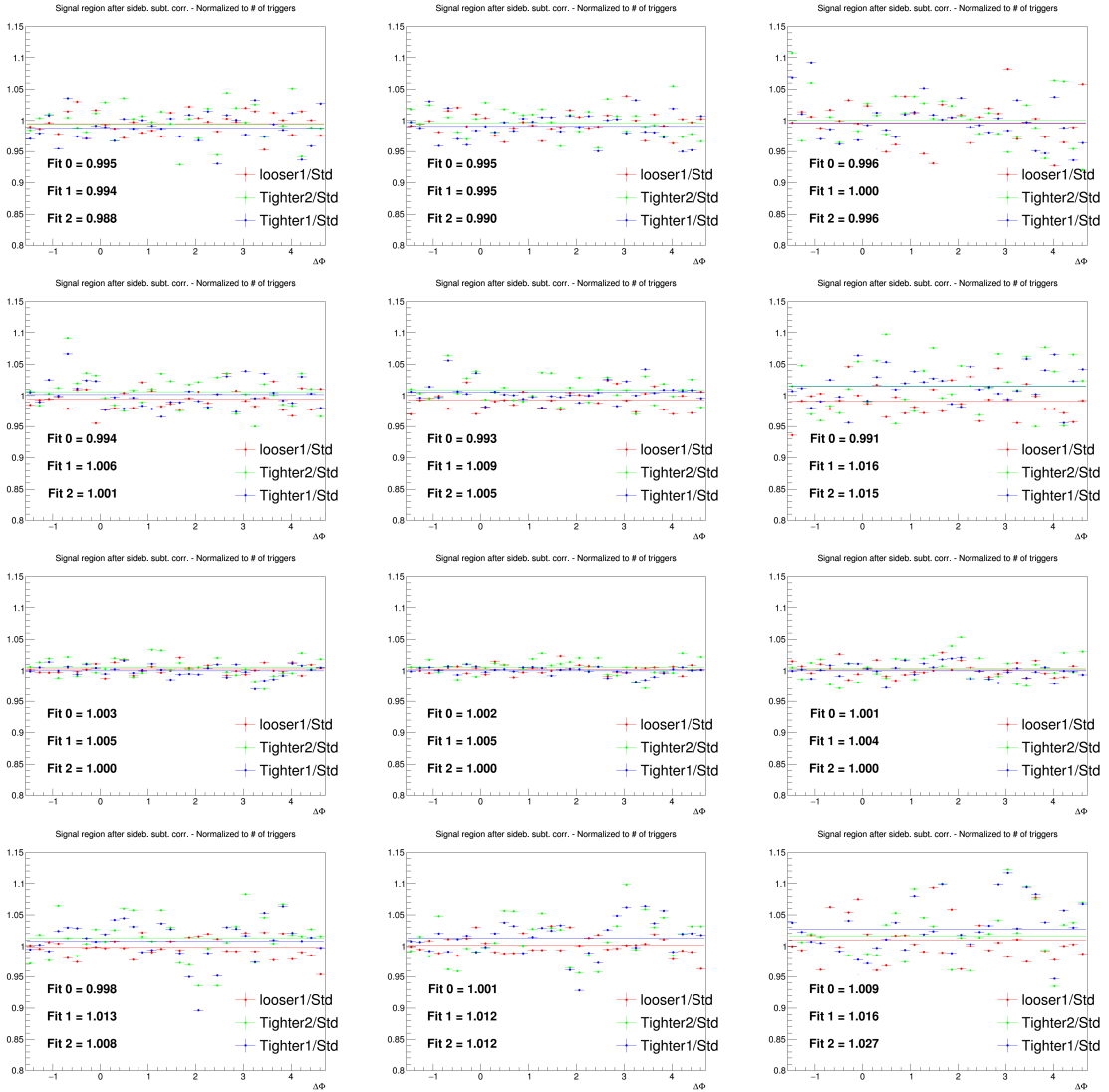


Figure 33: Ratios of D^{*+} - h correlation plots obtained with alternate D-meson cut sets over those obtained with standard selection. Rows: $p_T(D^{*+})$ 3-5, 5-8, 8-16, 16-24 GeV/ c . In each row, the panels show the associated track p_T ranges 0.3-1, >0.3 GeV/ c , >1 GeV/ c , respectively.

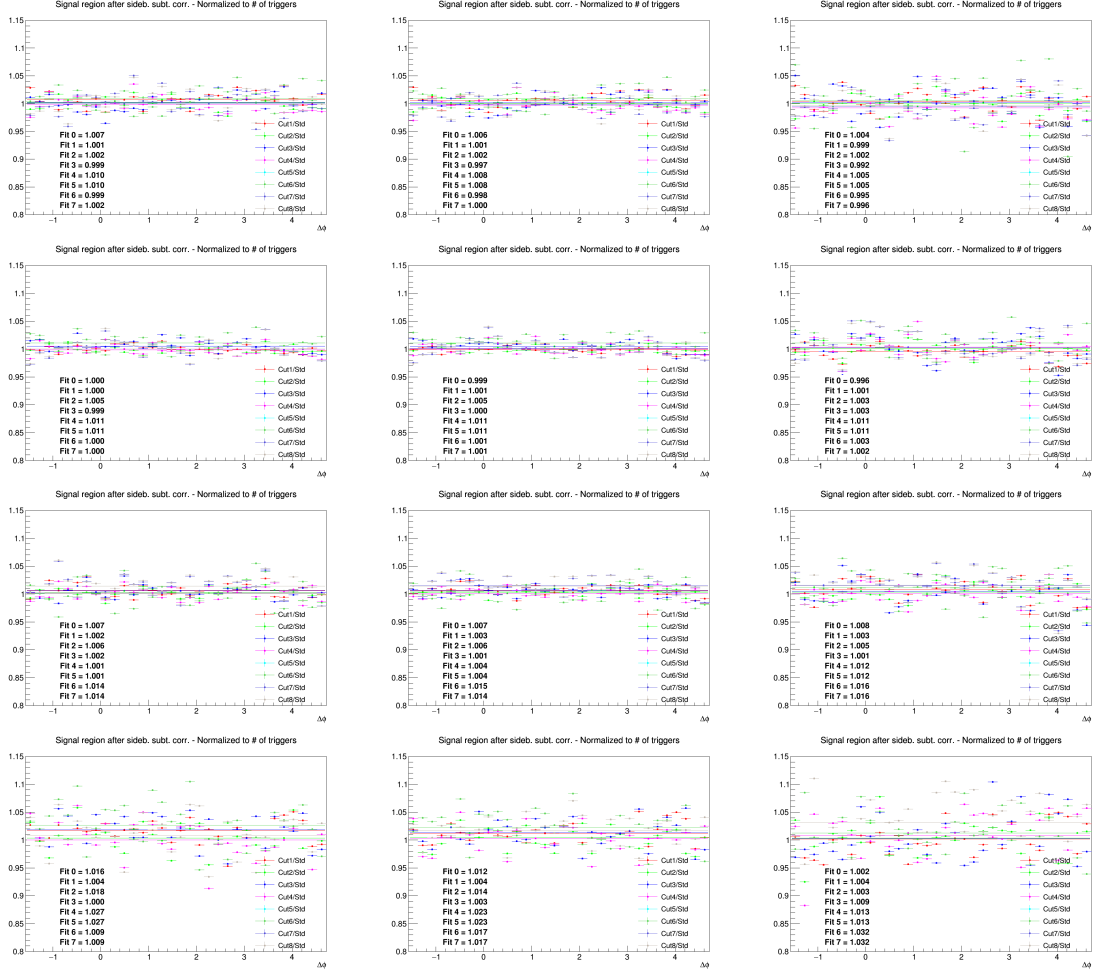


Figure 34: Ratios of D⁺ - h correlation plots obtained with alternate D-meson cut sets over those obtained with standard selection. Rows: $p_T(D^+)$ 3-5, 5-8, 8-16, 16-24 GeV/c. In each row, the panels show the associated track p_T ranges 0.3-1, >0.3 GeV/c, >1 GeV/c, respectively.



Figure 35: Ratios of D^0 - h correlation plots obtained with different associated tracks filtering selections. First 6 plots: $p_T(D)$ 3-5 GeV/c , next 6 plots: $p_T(D)$ 5-8 GeV/c . Each bunch of 6 plots has $p_T(\text{assoc})$ of >0.3 , 0.3-1, >1 , 1-2, 2-3, $<3 \text{ GeV}/c$, respectively.

590 4.7 Uncertainty on correction for the bias on B to D decay topologies

591 The evaluation of this systematic uncertainty was already explained in Section 3.3.3. For each of the
 592 five data points close to the center of the near-side peak, which are affected by the bias, a bilateral and
 593 symmetric uncertainty of amplitude $|C(\Delta\phi)_{\text{corr}} - C(\Delta\phi)_{\text{raw}}|/\sqrt{12}$ was assigned.

594 This because the uncorrected data points are expected to be the extreme (with the current D -meson
 595 selection, the bias is always upwards at the centre of the peak, and always upwards on its sides). We
 596 then assume that, if the correction is properly evaluated, the corrected data points are at the centre of the
 597 possible spread of the true unbiased results. In this case, the span of the possible true results (in case
 598 of underestimation/overestimation of the bias) goes from the uncorrected data points to its symmetric
 599 value, with respect to the corrected data point, on the other direction. If this distribution is uniform,
 600 and constrained by these two values, the 1σ confidence region for the position of the is in a bilateral
 601 $|C(\Delta\phi)_{\text{corr}} - C(\Delta\phi)_{\text{raw}}|/\sqrt{12}$ window, centered on the $C(\Delta\phi)_{\text{corr}}$ points.

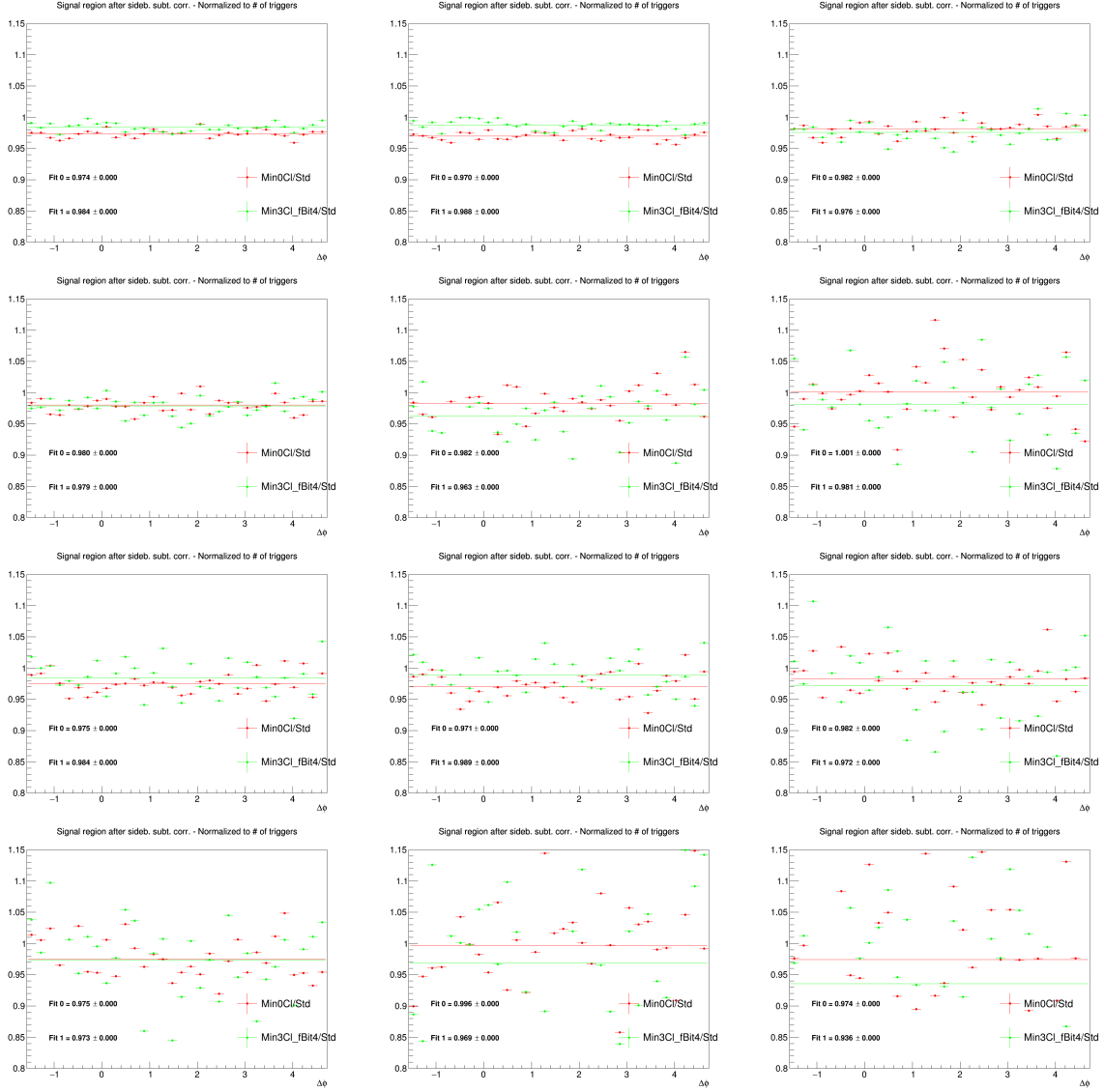


Figure 36: Ratios of D^0 - h correlation plots obtained with different associated tracks filtering selections. First 6 plots: $p_T(D) 8-16 \text{ GeV}/c$, next 6 plots: $p_T(D) 16-24 \text{ GeV}/c$. Each bunch of 6 plots has $p_T(\text{assoc})$ of >0.3 , $0.3-1$, >1 , $1-2$, $<3 \text{ GeV}/c$, respectively.

This source of uncertainty was assumed uncorrelated among the $\Delta\phi$ points.

4.8 Summary table

A summary of the $\Delta\phi$ -correlated uncertainties affecting the correlation distributions is shown in Figure 40. They are the S and B extraction uncertainty, the background shape uncertainty, the cut variation uncertainty, the tracking efficiency uncertainty and the secondary particle contamination uncertainty.

The overall amount of $\Delta\phi$ -correlated uncertainties is about 5-6% (depending on the p_T bin) for the single D-meson cases; when evaluating the averages of the distributions (see next section), this uncertainty shrinks to 4-5%. This uncertainty is a global scale factor of the distributions, and is quoted as a label in the plots.

The systematics uncertainties from feed-down subtraction and $B \rightarrow D$ decay topology bias, instead are $\Delta\phi$ dependent, and are hence reported as uncorrelated boxes in the plots. They do not amount to more than 4%, in every bin of all the kinematic ranges studied.

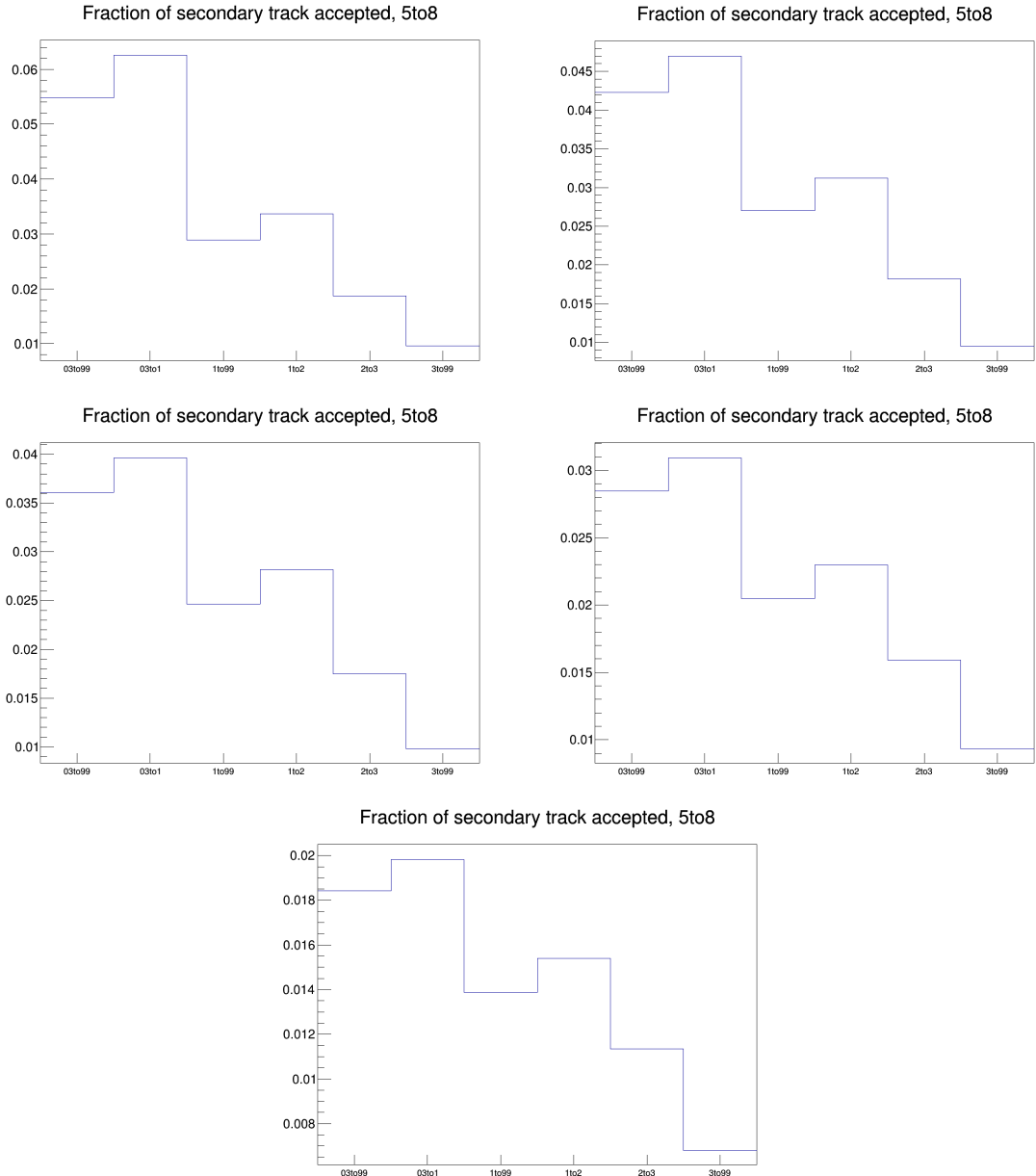


Figure 37: Secondary track contamination as a function of the associated track p_T , for the various DCA selections tried. The plots are ordered from the loosest to the tightest selection, i.e.: $\text{DCA}(xy) < 2.4 \text{ cm}$, $< 1 \text{ cm}$, $< 0.5 \text{ cm}$, $< 0.25 \text{ cm}$, $< 0.1 \text{ cm}$.

614 5 Results

615 5.1 Comparing the three D meson correlation distributions

616 To check the compatibility of three D meson analyses, Figure 41 shows the corrected azimuthal corre-
 617 lation distributions (except for the feed-down subtraction and the secondary contamination removal) for
 618 $D^0\text{-}h$, $D^{*+}\text{-}h$ and $D^+\text{-}h$, in each column, on the data sample used in the analysis. Results are shown for
 619 $3 < D p_T < 5 \text{ GeV}/c$, $5 < D p_T < 8 \text{ GeV}/c$, $8 < D p_T < 16 \text{ GeV}/c$ and $16 < D p_T < 24 \text{ GeV}/c$ with
 620 associated tracks $p_T > 0.3$, $p_T > 1$, $0.3 < p_T < 1 \text{ GeV}/c$, $1 < p_T < 2 \text{ GeV}/c$, $2 < p_T < 3 \text{ GeV}/c$ and
 621 $p_T > 3 \text{ GeV}/c$.

622 Figures 42, 43, 44, 45 show the superimposed correlation distributions from the single-meson analyses

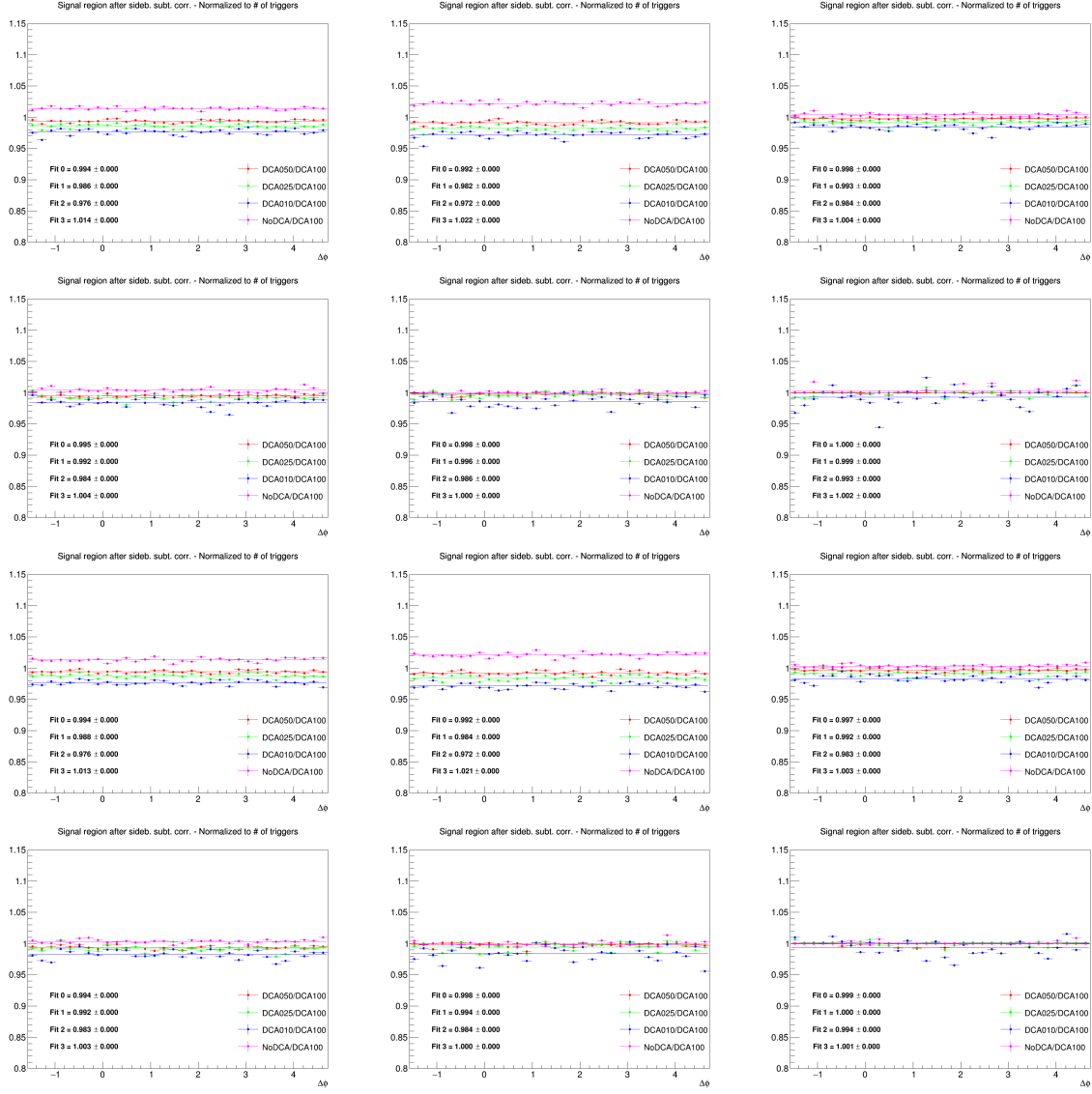


Figure 38: Ratios of correlation plots (with D^0 as trigger meson) obtained with different associated DCA selections, after purity correction. First 6 plots: $p_T(D)$ 3-5 GeV/ c , next 6 plots: $p_T(D)$ 5-8 GeV/ c . Each bunch of 6 plots has $p_T(\text{assoc})$ of >0.3 , 0.3-1, >1 , 1-2, 2-3, <3 GeV/ c , respectively.

623 (same plots as previous figure) for better visualize the agreement among the different D-meson species
624 results.

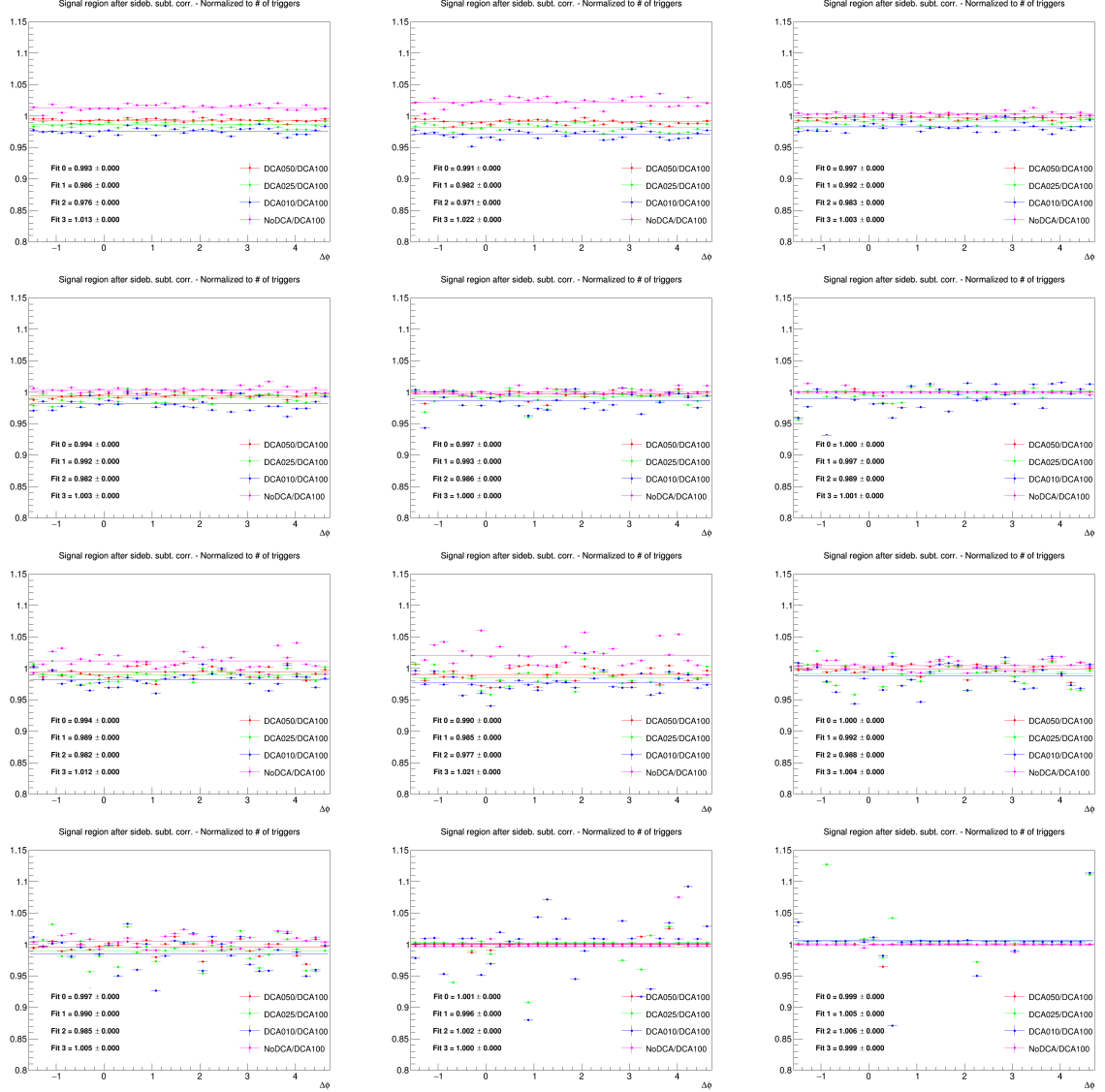


Figure 39: Ratios of correlation plots (with D^0 as trigger meson) obtained with different associated DCA selections, after purity correction. First 6 plots: $p_T(D)$ 8-16 GeV/c , next 6 plots: $p_T(D)$ 16-24 GeV/c . Each bunch of 6 plots has $p_T(\text{assoc})$ of >0.3 , $0.3-1$, >1 , $1-2$, $2-3$, $<3 \text{ GeV}/c$, respectively.

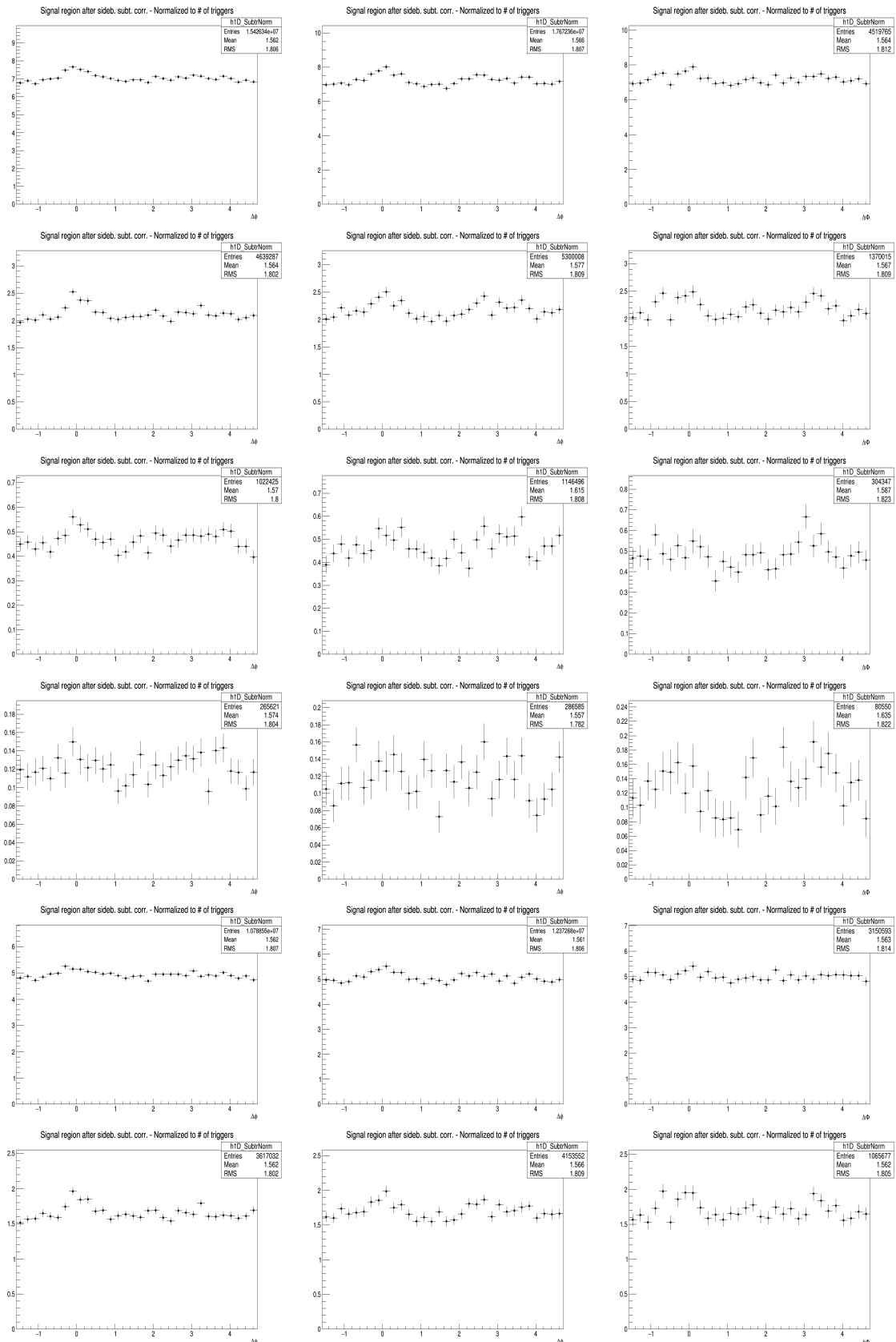
pPb Sample	D^0				D^*				D^+			
D Pt Range (GeV/c)	3-5	5-8	8-16	16-24	3-5	5-8	8-16	16-24	3-5	5-8	8-16	16-24
S and B Extraction	1%	1%	1%	3%	1%	1%	1%	2%	1%	1%	1%	2%
Background Correlation Shape	1%	1%	1%	3%	1%	1%	1%	3%	1%	1%	1%	3%
D meson Cut Variation	2%	2%	2%	2%	1.5%	1.5%	1%	1%	1%	1%	1%	3%

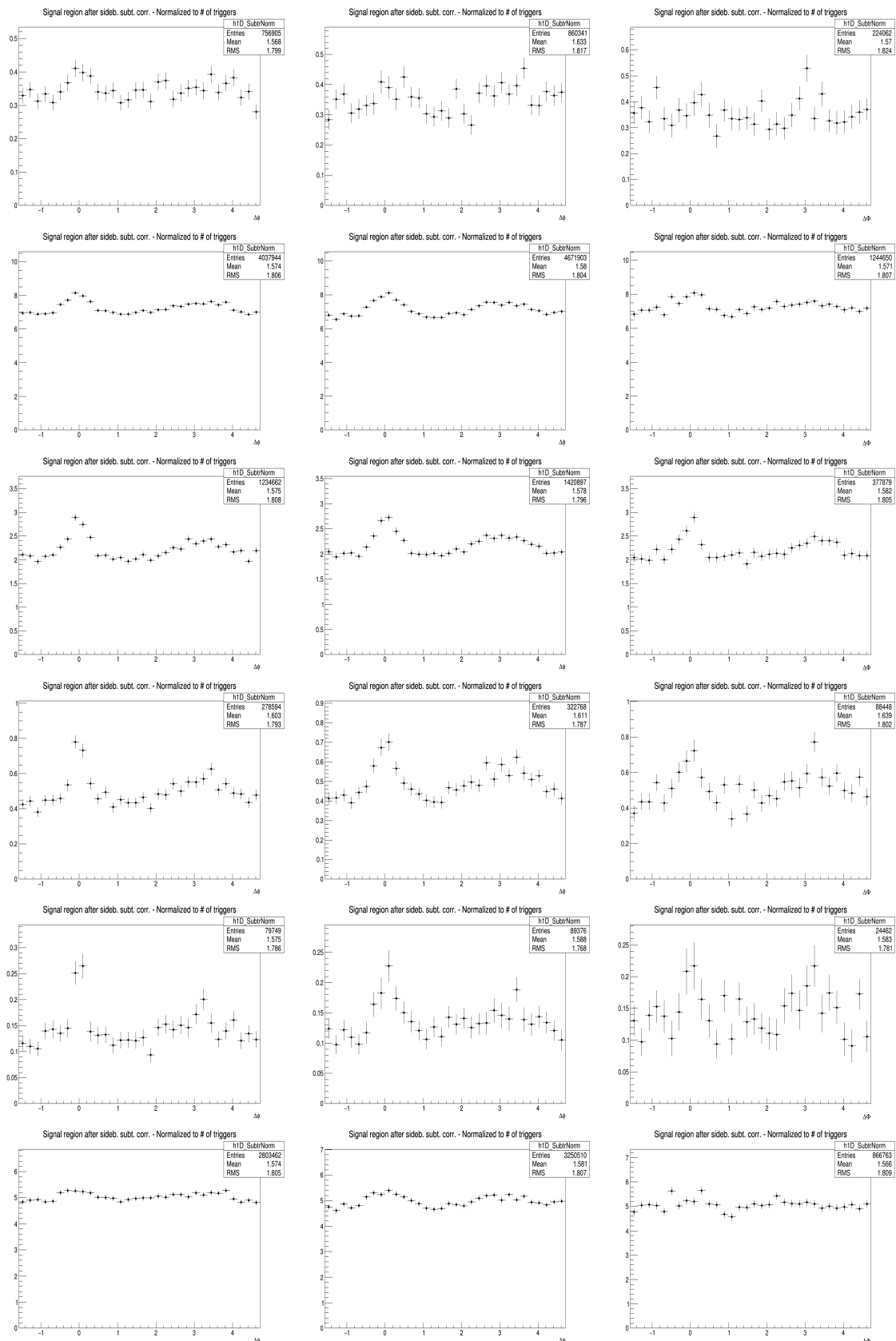
pPb Sample	D^0, D^* and D^+ (common for all the $p_T(D)$ ranges)						
Assoc (p_T) Ranges (GeV/c)	> 0.3	> 1.0	> 2.0	> 3.0	0.3-1.0	1.0-2.0	2.0-3.0
Track Efficiency	3.5%	3.5%	3.5%	3.5%	3.5%	3.5%	3.5%
Purity	2.5%	1.5%	1.5%	1.5%	3%	1.5%	1.5%

Figure 40: Summary of the $\Delta\phi$ -correlated uncertainties associated to the correlation distributions, for three D-mesons, in the different kinematic ranges of D meson and hadrons.

5.1 Comparing the three D meson correlation distributions

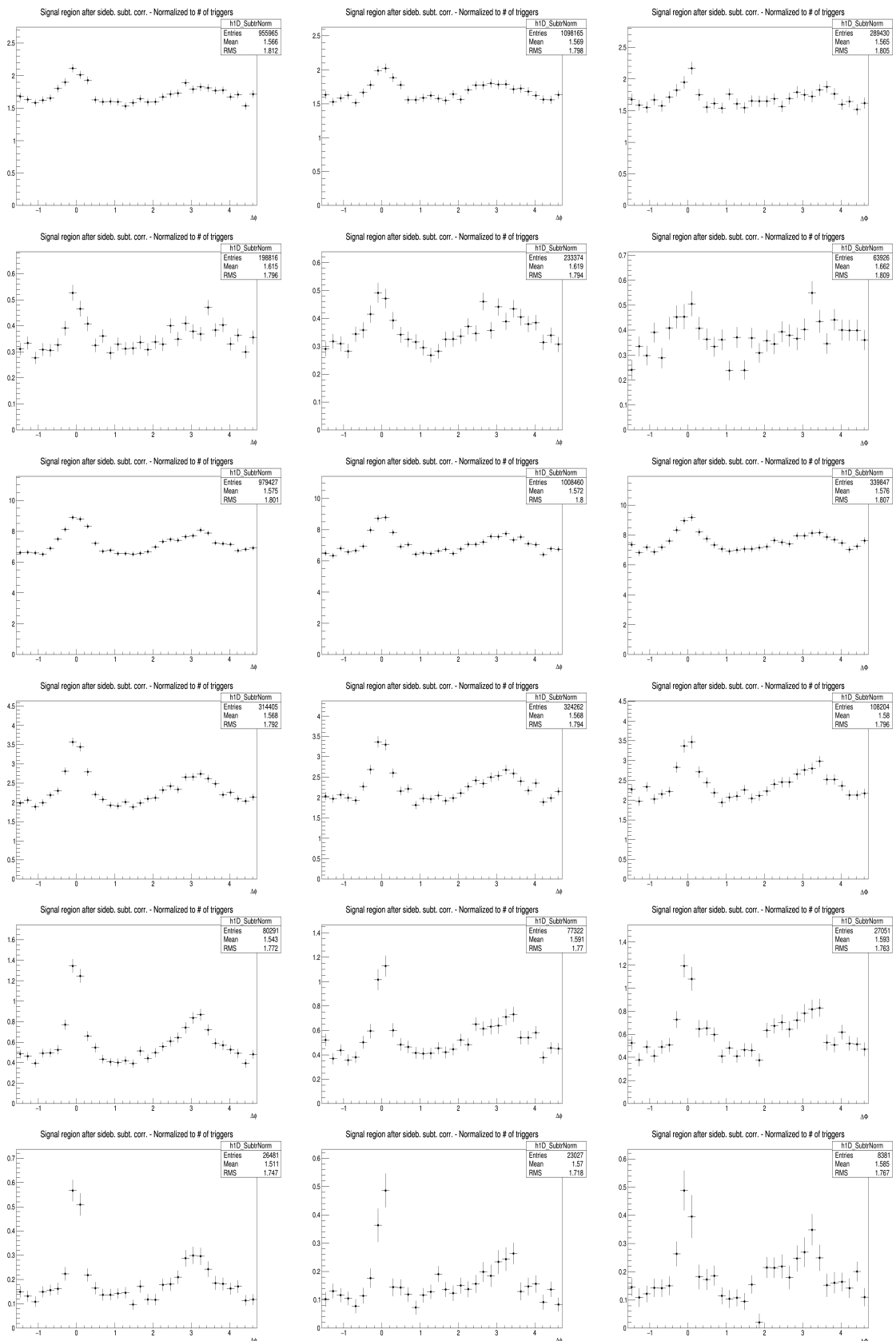
55

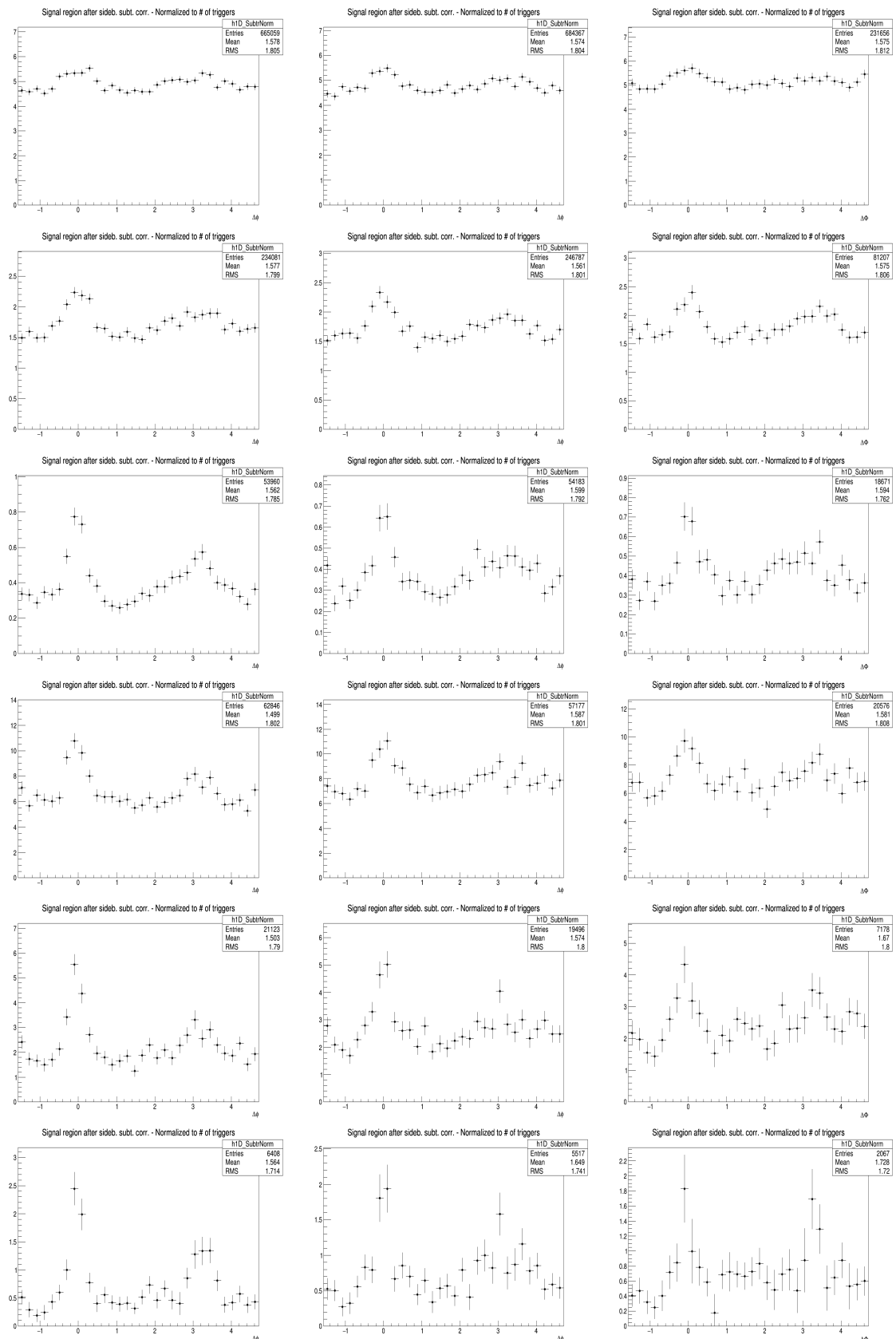




5.1 Comparing the three D meson correlation distributions

57





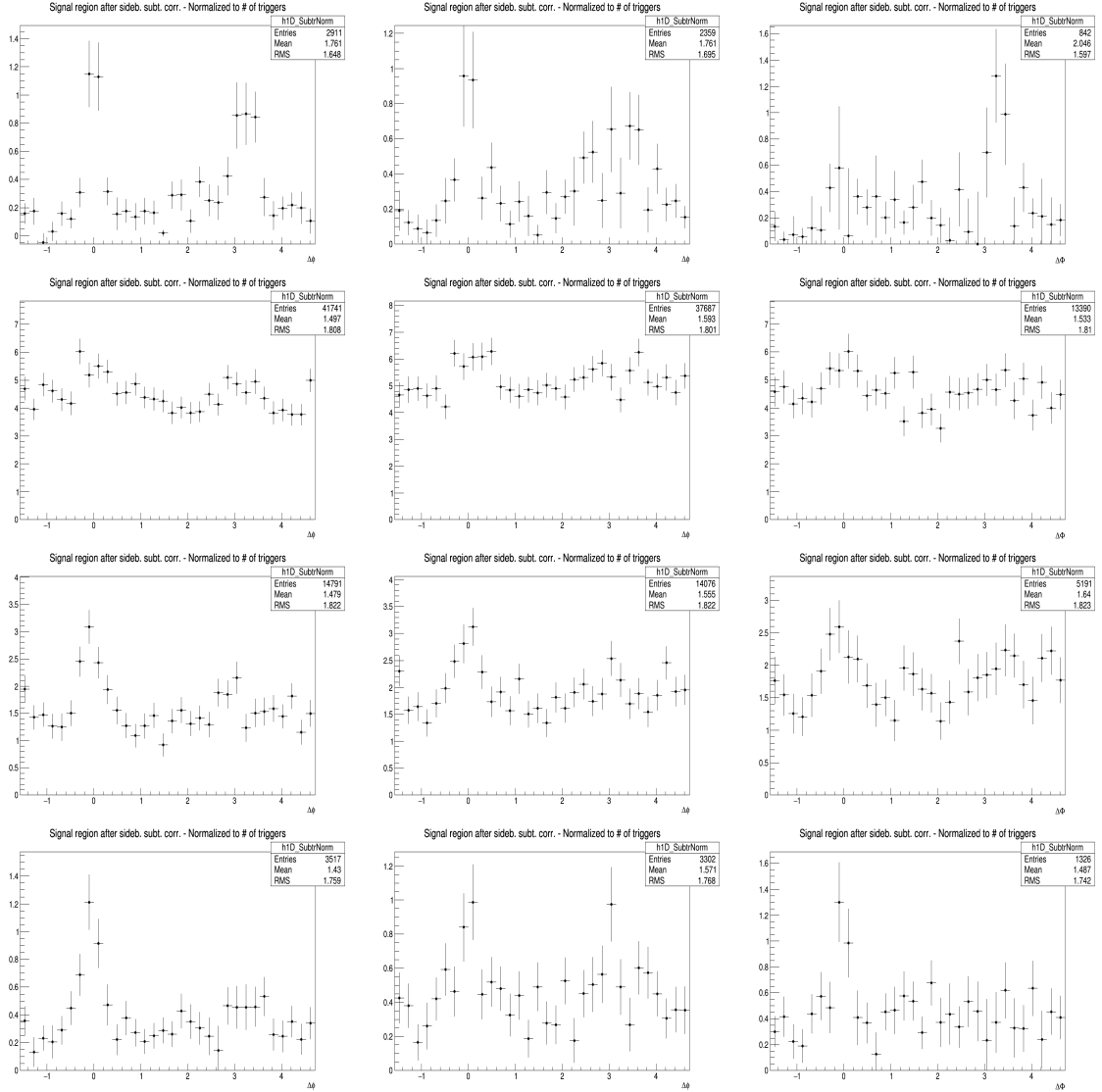


Figure 41: Corrected distribution of D-hadrons azimuthal correlations for the three species (apart from feed-down and purity), from analysis on the data sample, for the analyzed D-meson (**Column-Left:** D^0 , **Column-Middle:** D^+ and **Column-Right:** D^{*+}) and different associated tracks p_T ranges (**Row 1-7:** $3 < D_{pT} < 5 \text{ GeV}/c$, $p_T(\text{Assoc}) > 0.3, >1.0, >2.0, >3.0, 0.3-1.0, 1.0-2.0$ and $2.0-3.0 \text{ GeV}/c$ respectively), (**Row 8-14:** $5 < D_{pT} < 8 \text{ GeV}/c$, $p_T(\text{Assoc}) > 0.3, >1.0, >2.0, >3.0, 0.3-1.0, 1.0-2.0$ and $2.0-3.0 \text{ GeV}/c$ respectively), (**Row 15-21:** $8 < D_{pT} < 16 \text{ GeV}/c$, $p_T(\text{Assoc}) > 0.3, >1.0, >2.0, >3.0, 0.3-1.0, 1.0-2.0$ and $2.0-3.0 \text{ GeV}/c$ respectively) and (**Row 22-28:** $16 < D_{pT} < 24 \text{ GeV}/c$, $p_T(\text{Assoc}) > 0.3, >1.0, >2.0, >3.0, 0.3-1.0, 1.0-2.0$ and $2.0-3.0 \text{ GeV}/c$ respectively)

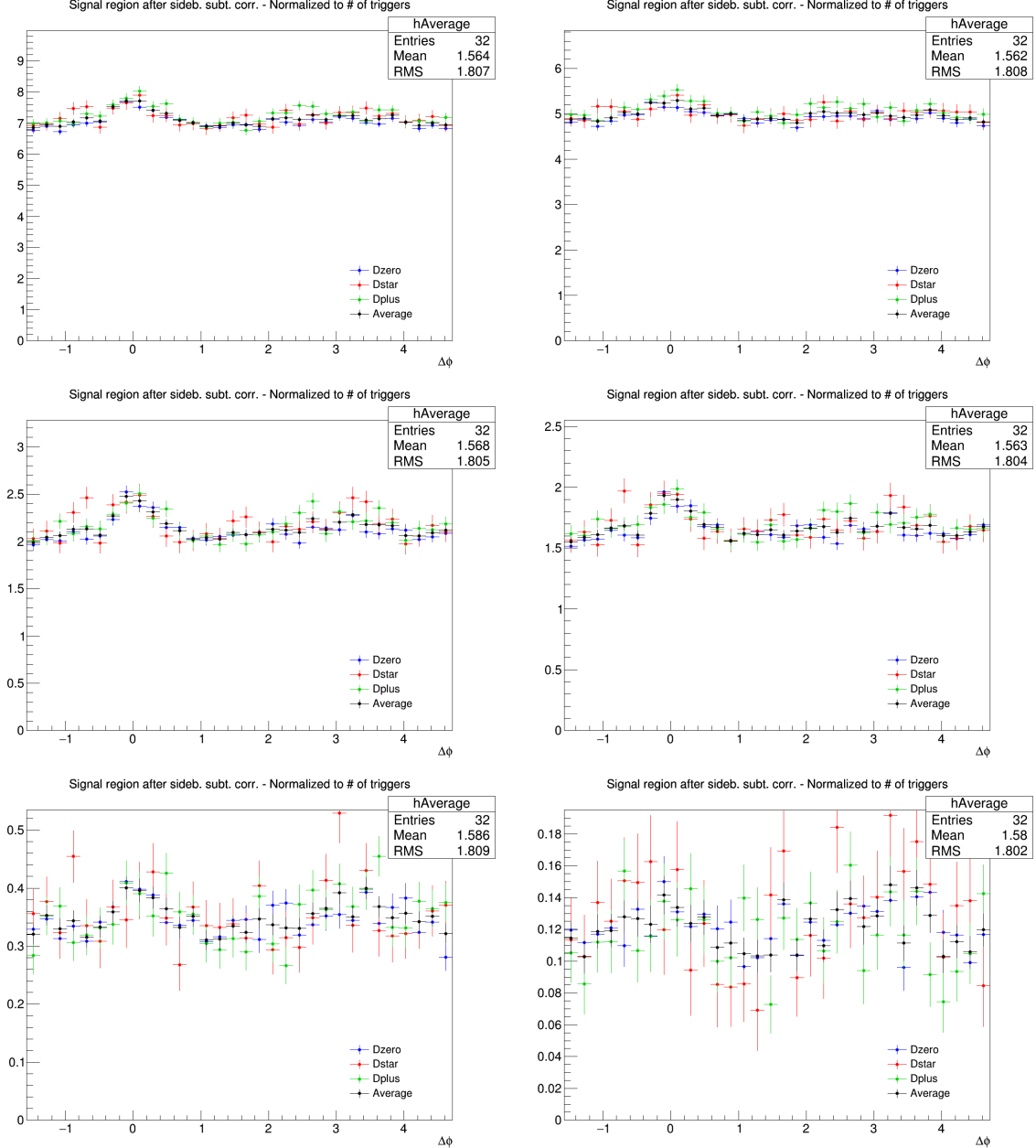


Figure 42: Superimposition of the corrected distribution of D-hadrons azimuthal correlations for the three species (apart from feed-down and purity), from analysis on the data sample, for the analyzed D-meson and different associated track p_T ranges, and D-meson p_T ranges (3-5 GeV/c on this page). **Panels from 1 to 6 of each page:** p_T (Assoc) > 0.3, 0.3-1.0, >1.0, 1.0-2.0, 2.0-3.0 and >3.0 GeV/c

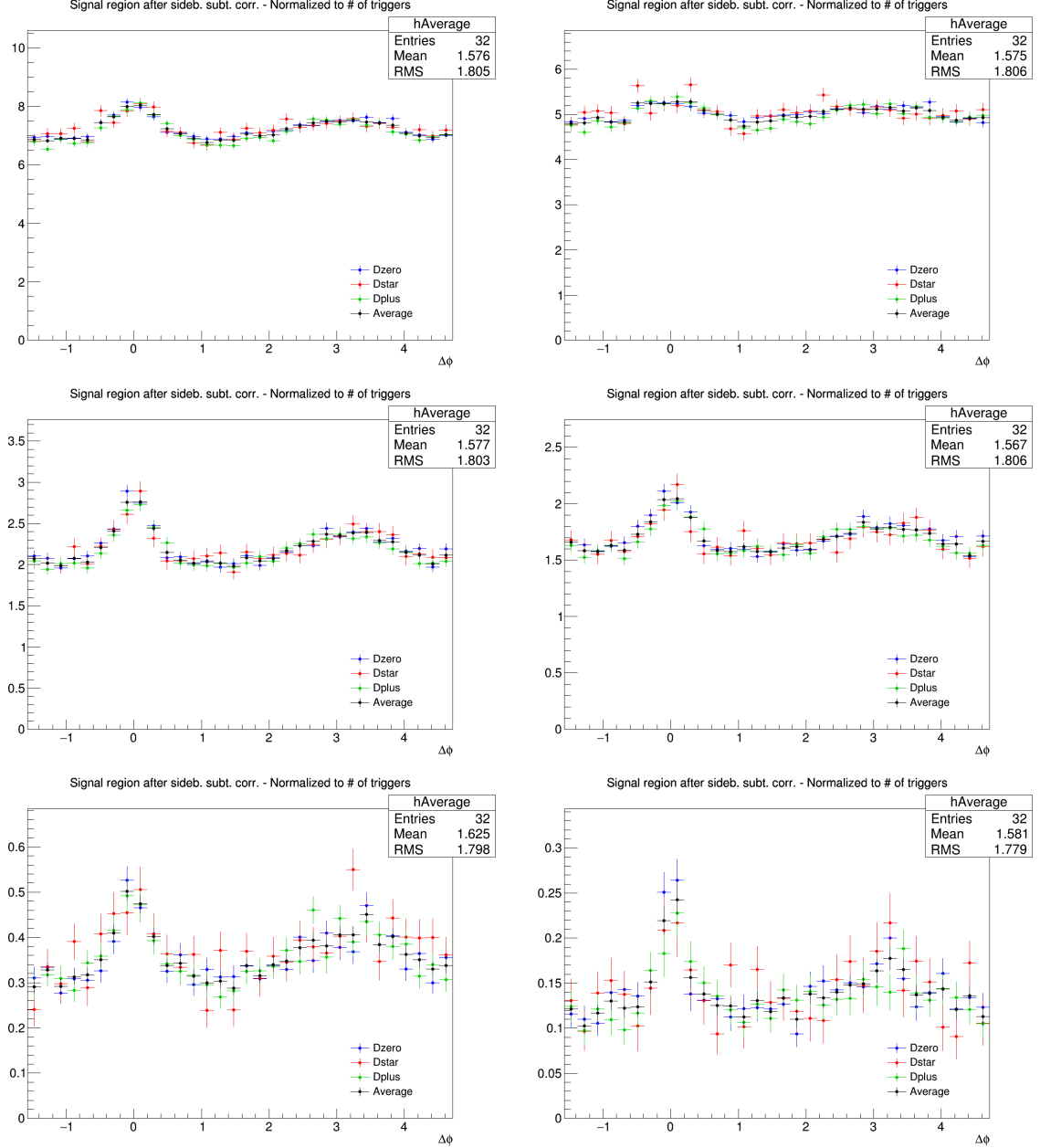


Figure 43: Superimposition of the corrected distribution of D-hadrons azimuthal correlations for the three species (apart from feed-down and purity), from analysis on the data sample, for the analyzed D-meson and different associated track p_T ranges, and D-meson p_T ranges (5-8 GeV/c on this page). **Panels from 1 to 6 of each page:** $p_T(\text{Assoc}) > 0.3, 0.3-1.0, >1.0, 1.0-2.0, 2.0-3.0$ and $>3.0 \text{ GeV}/c$

625 An agreement of the distributions from the three mesons within the uncertainties is found in all the
626 kinematic ranges.

627 Despite being evaluated in the full 2π range, the range of final results was then reduced to $[0, \pi]$ radians,
628 reflecting the points outside that range over the value of 0. This allowed to reduce the impact of statistical
629 fluctuations on the data points (supposing equal statistics for a pair of symmetric bins, after the reflection
630 the relative statistical uncertainty for the resulting bin is reduced by a factor $1/\sqrt{2}$).

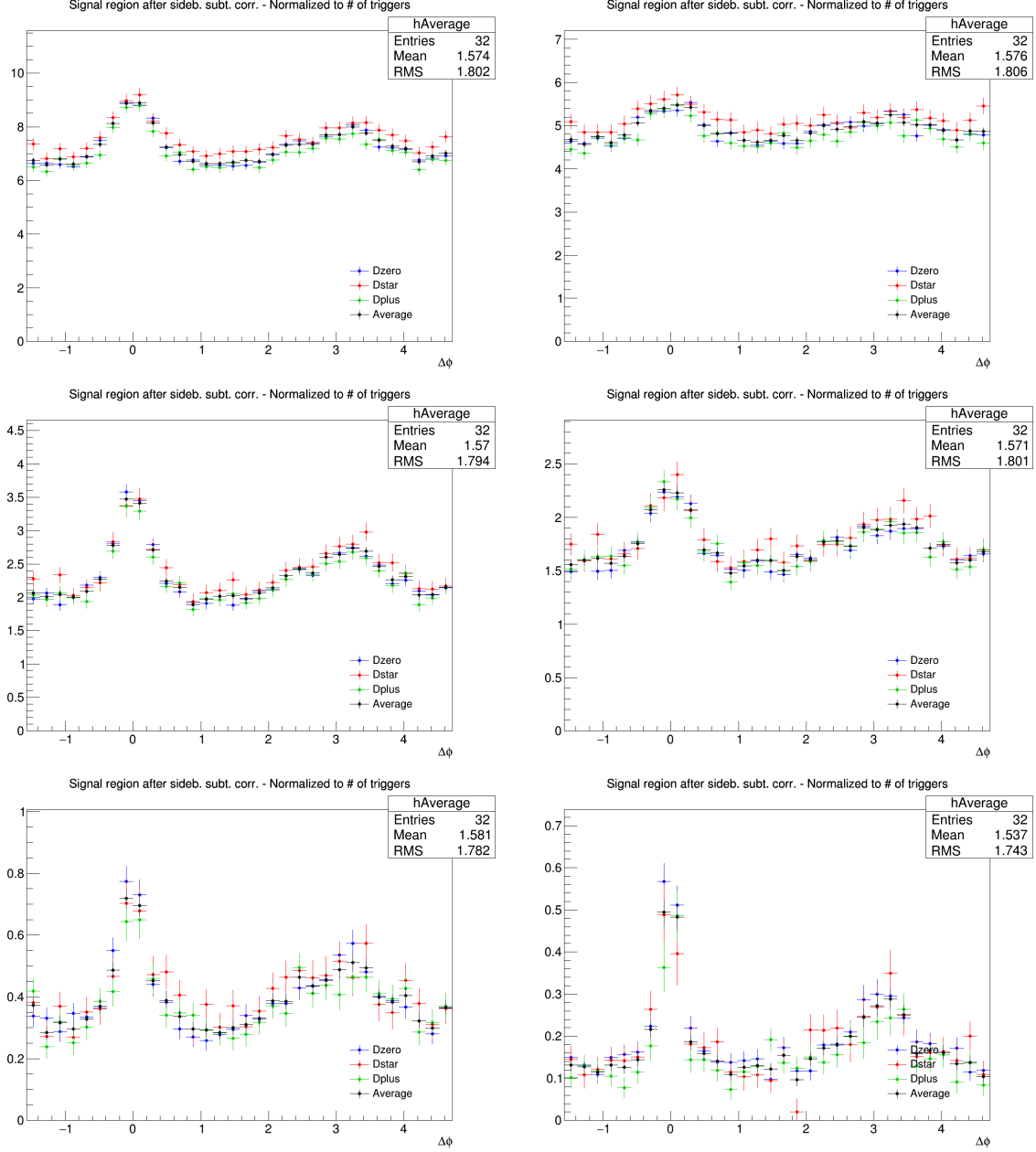


Figure 44: Superimposition of the corrected distribution of D-hadrons azimuthal correlations for the three species (apart from feed-down and purity), from analysis on the data sample, for the analyzed D-meson and different associated track p_T ranges, and D-meson p_T ranges (8-16 GeV/c on this page). **Panels from 1 to 6 of each page:** p_T (Assoc) > 0.3, 0.3-1.0, >1.0, 1.0-2.0, 2.0-3.0 and >3.0 GeV/c

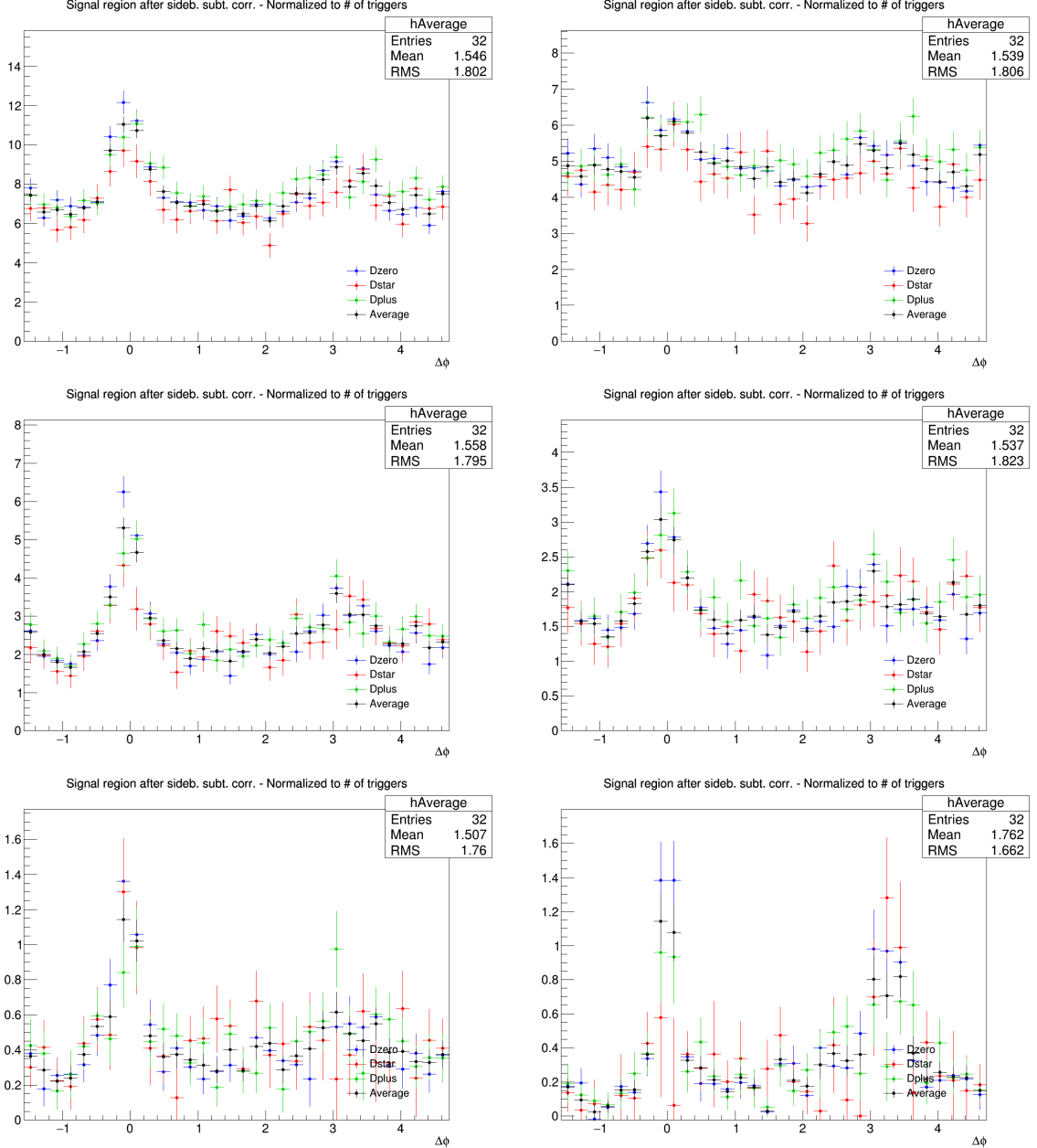


Figure 45: Superimposition of the corrected distribution of D-hadrons azimuthal correlations for the three species (apart from feed-down and purity), from analysis on the data sample, for the analyzed D-meson and different associated track p_T ranges, and D-meson p_T ranges (16-24 GeV/c on this page). **Panels from 1 to 6 of each page:** $p_T(\text{Assoc}) > 0.3, 0.3-1.0, >1.0, 1.0-2.0, 2.0-3.0$ and $>3.0 \text{ GeV}/c$

631 **5.2 Average of D⁰, D⁺ and D^{*+} results**

632 Given the compatibility within the uncertainties among the D⁰, D⁺ and D^{*+} azimuthal correlations, and
 633 since no large differences are visible in the correlation distributions observed in Monte Carlo simulations
 634 based on Pythia with Perugia0, 2010 and 2011 tunes¹, it was possible to perform a weighted average
 635 (eq. 5) of the azimuthal correlation distributions of D⁰, D⁺ and D^{*+}, in order to reduce the overall
 636 uncertainties. Although some correlation between the mesons could be present (about the 30% of the
 637 D⁰, and also part of the D⁺, come from D^{*+} decays), the three selected D-meson samples can be treated
 638 as uncorrelated. The sum of the statistical uncertainties; the systematics uncertainty on S and B extraction
 639 and on background shape, are added in quadrature and the inverse of this sum was used as weight, w_i .

$$\left\langle \frac{1}{N_D} \frac{dN_{\text{assoc}}}{dp_T} \right\rangle_{D\text{mesons}} = \frac{\sum_{i=\text{meson}} w_i \frac{1}{N_D} \frac{dN_i^{\text{assoc}}}{d\Delta\phi}}{\sum_{i=\text{meson}} w_i}, w_i = \frac{1}{\sigma_{i,\text{stat}}^2 + \sigma_{i,\text{uncorr.syst}}^2} \quad (5)$$

640 The statistical uncertainty and the uncertainties on S and B extraction and on background shape (those
 641 used for the weights) on the average were then recalculated using the following formula:

$$\sigma^2 = \frac{1}{n_D} \frac{\sum_{i=\text{meson}} w_i \sigma_i^2}{\sum_{i=\text{meson}} w_i} \quad (6)$$

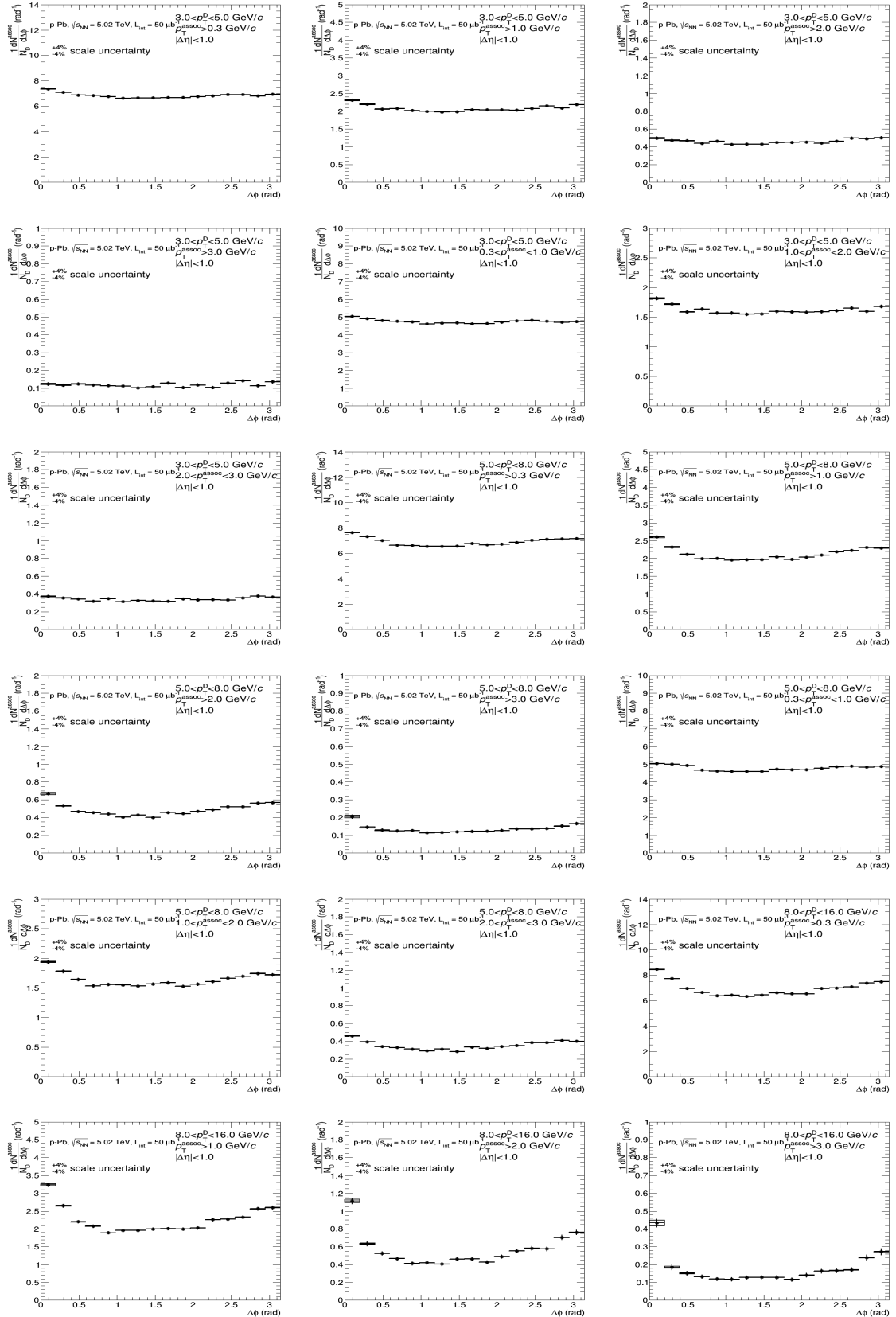
642 where n_D is the number of mesons considered in the average. It can be observed that for $\sigma_i^2 = 1/w_i$ the
 643 formula coincides with the standard one giving the uncertainty on a weighted average. The contribution
 644 to the average systematic uncertainty for those uncertainty sources not included in the weight definition,
 645 was evaluated via error propagation on the formula of the weighted average (5), resulting in equation
 646 (7) and (8) for sources considered uncorrelated and correlated among the mesons. In particular, the
 647 uncertainties on the associated track reconstruction efficiency, on the contamination from secondary, on
 648 the feed-down subtraction, and that resulting from the Monte Carlo closure test were considered fully
 649 correlated among the mesons, while those deriving from the yield extraction (included in the weight
 650 definition) and on the D meson reconstruction and selection efficiency were treated as uncorrelated.

$$\sigma^2 = \frac{\sum_{i=\text{meson}} w_i^2 \sigma_i^2}{(\sum_{i=\text{meson}} w_i)^2} \quad (7)$$

$$\sigma = \frac{\sum_{i=\text{meson}} w_i \sigma_i}{\sum_{i=\text{meson}} w_i} \quad (8)$$

651 Figure 46 shows the averages of the azimuthal correlation distributions of D⁰, D⁺ and D^{*+} and charged
 652 particles with $p_T > 0.3$ GeV/c, $0.3 < p_T < 1$ GeV/c, $p_T > 1$ GeV/c, $1 < p_T < 2$ GeV/c, $2 < p_T <$
 653 3 GeV/c, $p_T < 3$ GeV/c in the D meson p_T ranges $3 < p_T < 5$ GeV/c, $5 < p_T < 8$ GeV/c, $8 < p_T <$
 654 16 GeV/c and $16 < p_T < 24$ GeV/c. As expected, a rising trend of the height of the near-side peak
 655 with increasing D-meson p_T is observed, together with a decrease of the baseline level with increasing
 656 p_T of the associated tracks. To further increase the statistical precision on the averaged correlation
 657 distributions, given the symmetry around 0 on the azimuthal axis, the distributions were reflected and
 658 shown in the range $[0, \pi]$. This reduces the statistical uncertainty on the points by, approximately, a factor
 659 of $1/\sqrt{2}$.

¹A slight near side hierarchy is present among the three meson results, with D^{*+} meson having a lower peak amplitude than D⁰ and D⁺. It was verified that this is induced by the presence of D⁰ and D⁺ mesons coming from D^{*+}, the latter having on average a larger p_T and coming, hence, on average, from a larger p_T quark parton, which fragments in slightly more tracks in the near-side.



660 The usage of weighted average requires, as an underlying assumption, identical results expected for
 661 different species (or, at least, compatible within the uncertainties). Anyway, it was also verified that the
 662 usage of the arithmetic average instead of the weighted average increases the uncertainties on the points,

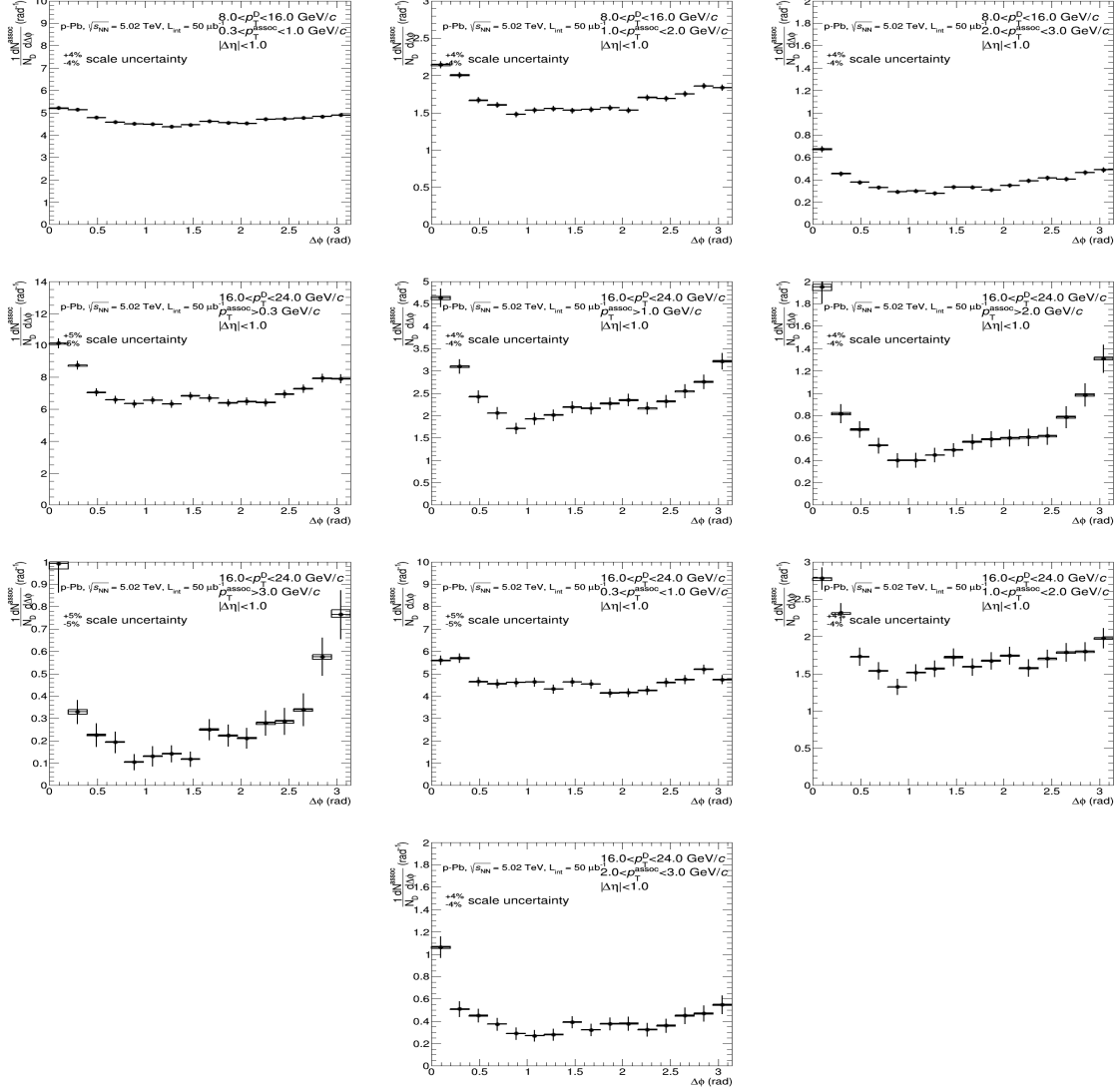


Figure 46: Average of D^0 , D^+ and D^{*+} azimuthal correlation distributions, in the D meson p_T ranges $3 < p_T < 5 \text{ GeV}/c$, $5 < p_T < 8 \text{ GeV}/c$, $8 < p_T < 16 \text{ GeV}/c$ and $16 < p_T < 24 \text{ GeV}/c$, with associated tracks with $p_T > 0.3 \text{ GeV}/c$, $p_T > 1 \text{ GeV}/c$ and $0.3 < p_T < 1 \text{ GeV}/c$.

663 but produces a negligible shift of their central values.

664 5.3 Fit observable p_T trends and uncertainties

665 In order to extract quantitative and physical information from the data correlation patterns, the averaged
 666 D-h correlation distributions are fitted with two Gaussian functions (with means fixed at $\Delta\varphi=0$ and $\Delta\varphi=\pi$
 667 values), plus a constant term (baseline). A periodicity condition is also applied to the fit function to obtain
 668 the same value at the bounds of 2π range. The expression of the fit function is reported below (equation
 669 9):

$$f(\Delta\varphi) = c + \frac{Y_{NS}}{\sqrt{2\pi}\sigma_{NS}} e^{-\frac{(\Delta\varphi-\mu_{NS})^2}{2\sigma_{NS}^2}} + \frac{Y_{AS}}{\sqrt{2\pi}\sigma_{AS}} e^{-\frac{(\Delta\varphi-\mu_{AS})^2}{2\sigma_{AS}^2}} \quad (9)$$

670 where baseline is calculated as the weighted average of the points lying in the so-called "transverse
 671 region", i.e. the interval $\frac{\pi}{4} < |\Delta\varphi| < \frac{\pi}{2}$.

672 An example of the results from the fit is shown in Figure 47

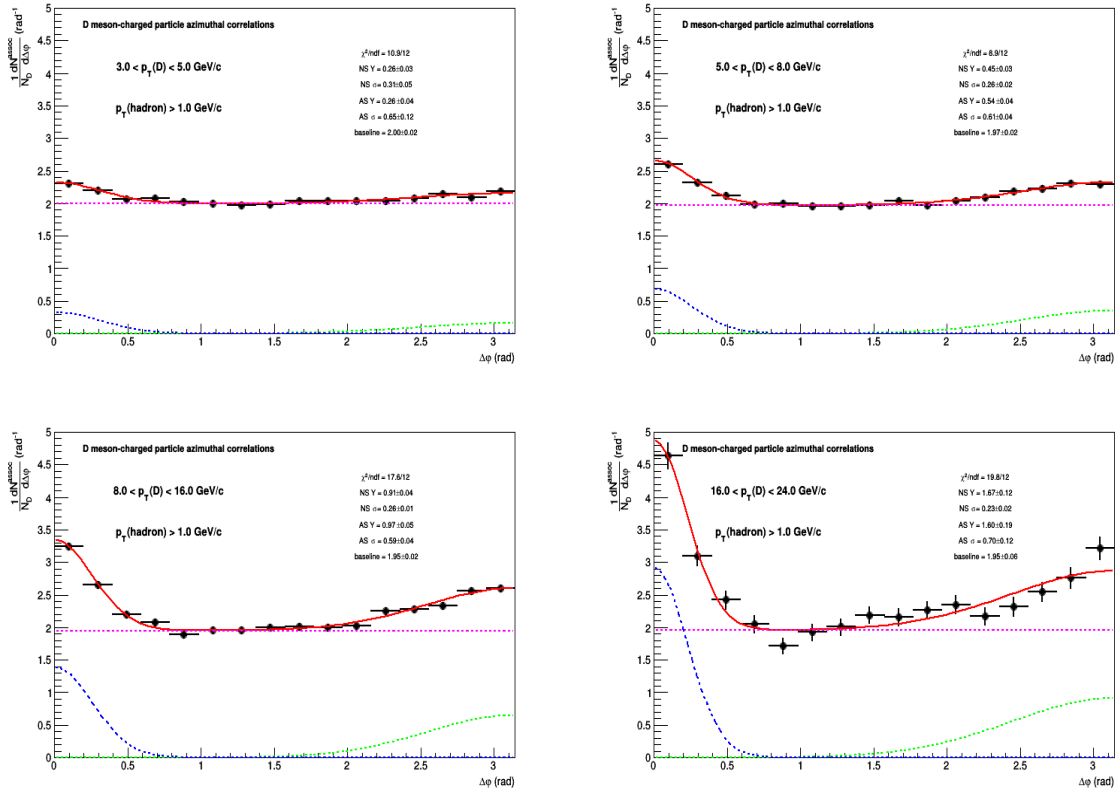


Figure 47: Example of fit to azimuthal correlation distributions and baseline estimation.

673 From the fit outcome, it is possible to retrieve the near-side and away-side yield and widths (integral
 674 and sigma of the Gaussian functions, respectively), as well as the baseline height of the correlation
 675 distribution. The near-side observables give information on the multiplicity and angular spread of the
 676 tracks from the fragmentation of the charm jet which gave birth to the D-meson trigger. At first order,
 677 instead, the away-side observables are related to the hadronization of the charm parton produced in the
 678 opposite direction (though the presence of NLO processes for charm production breaks the full validity
 679 of this assumption). The baseline value is a rough indicator of the underlying event multiplicity, though

680 below the baseline level also charm and beauty-related pairs are contained (especially in cases of NLO
 681 production for the heavy quarks).

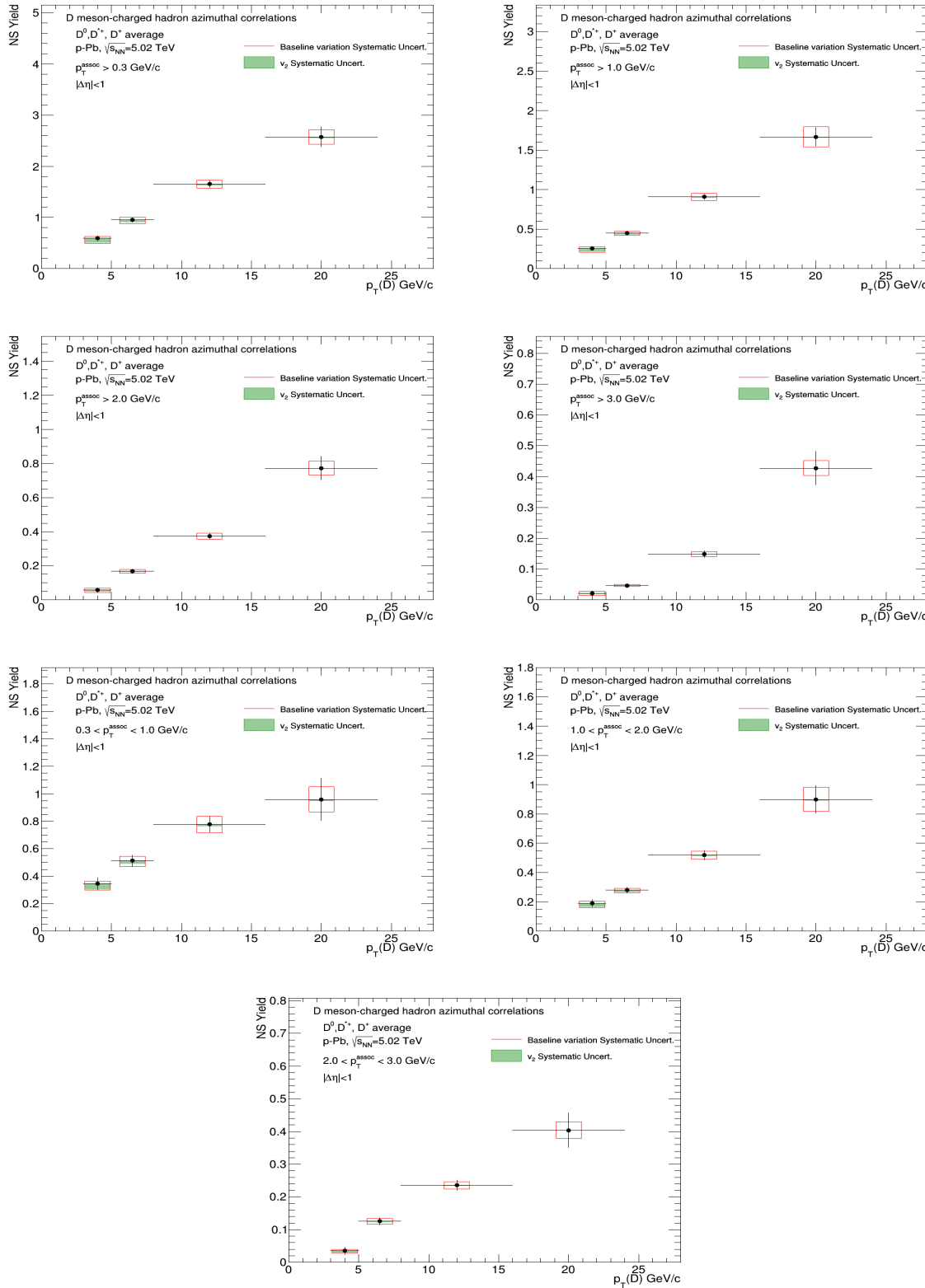
682 The evaluation of the systematic uncertainties on the observables obtained from the fits is performed as
 683 follows:

- 684 – The fits are repeated by changing the range of the transverse region in which the baseline is evaluated.
 685 Alternate definitions of $\frac{\pi}{4} < |\Delta\phi| < \frac{3\pi}{8}$, $\frac{3\pi}{8} < |\Delta\phi| < \frac{\pi}{2}$ and $\frac{\pi}{4} < |\Delta\phi| < \frac{5\pi}{8}$ are considered.
- 686 – In addition, $\Delta\phi$ correlation points are shifted to the upper and lower bounds of their uncorrelated
 687 systematic boxes, and refitted.
- 688 – The maximum variation of the parameters between the fit outcomes defined in the previous points
 689 is considered as systematic uncertainty for the near-side and away-side widths.
- 690 – For the estimation of the baseline and of the near-side and away-side yields, the previous value is
 691 added in quadrature with the $\Delta\phi$ -correlated systematics in the correlation distributions, since these
 692 values are affected by a change in the global normalization of the distributions.
- 693 – In addition, for all the fit observables, another fit variation is performed assuming, instead of a flat
 694 baseline, a $v_{2\Delta}$ -like modulation, with the following v_2 values for the associated tracks (assuming
 695 $v_{2\Delta} = v_2(h) \cdot v_2(D)$): 0.04 (0.3-1 GeV/c), 0.06 (>0.3 GeV/c), 0.08 (1-2 GeV/c), 0.09 (>1 GeV/c, 2-
 696 3 GeV/c), 0.1 (>3 GeV/c), on the basis of ATLAS preliminary results for heavy-flavour muons at
 697 8 TeV; for the D-meson triggers the following v_2 values were instead assumed: 0.05 (3-5 GeV/c),
 698 0.03 (5-8 GeV/c), 0.02 (8-24 GeV/c), on the basis of previous ALICE measurements in p-Pb
 699 collisions at 5 TeV [3]. The difference of the fit observables with respect to the standard fits is
 700 taken as uncertainty. Due to its peculiarity, this systematic uncertainty is summed in quadrature
 701 with the others to obtain the total uncertainty, but is also shown separately in the figures.

$$\sigma^{syst} = \sqrt{(Max(\Delta par^{ped.mode}, \Delta par^{\Delta\phi point}))^2 + (\sigma_{Syst}^{corr})^2} \quad (10)$$

702 5.3.1 Results for near-side yield and width, away-side yield and width, and baseline

703 Figures 48, 49, 50, 51 and 52 show the near-side associated yield, width (the sigma of the Gaussian part
 704 of the fit functions), away-side associated yield, width and the height of the baseline, for the average
 705 correlation distributions, in the kinematic ranges studied in the analysis, together with their statistical
 706 and systematic uncertainties. For each kinematic range, the correspondent plot showing the systematic
 707 uncertainty of the considered observable from the variation of the fit procedure is reported as well (which
 708 is the full systematic uncertainty for the widths). Figures 53, 54, 55, 56 and 57 show the full systematic
 709 uncertainties for near side yield and width, away side yield and width, and baseline, with the breakdown
 710 of fit variation, $v_{2\Delta}$ and $\Delta\phi$ correlated systematic uncertainties.



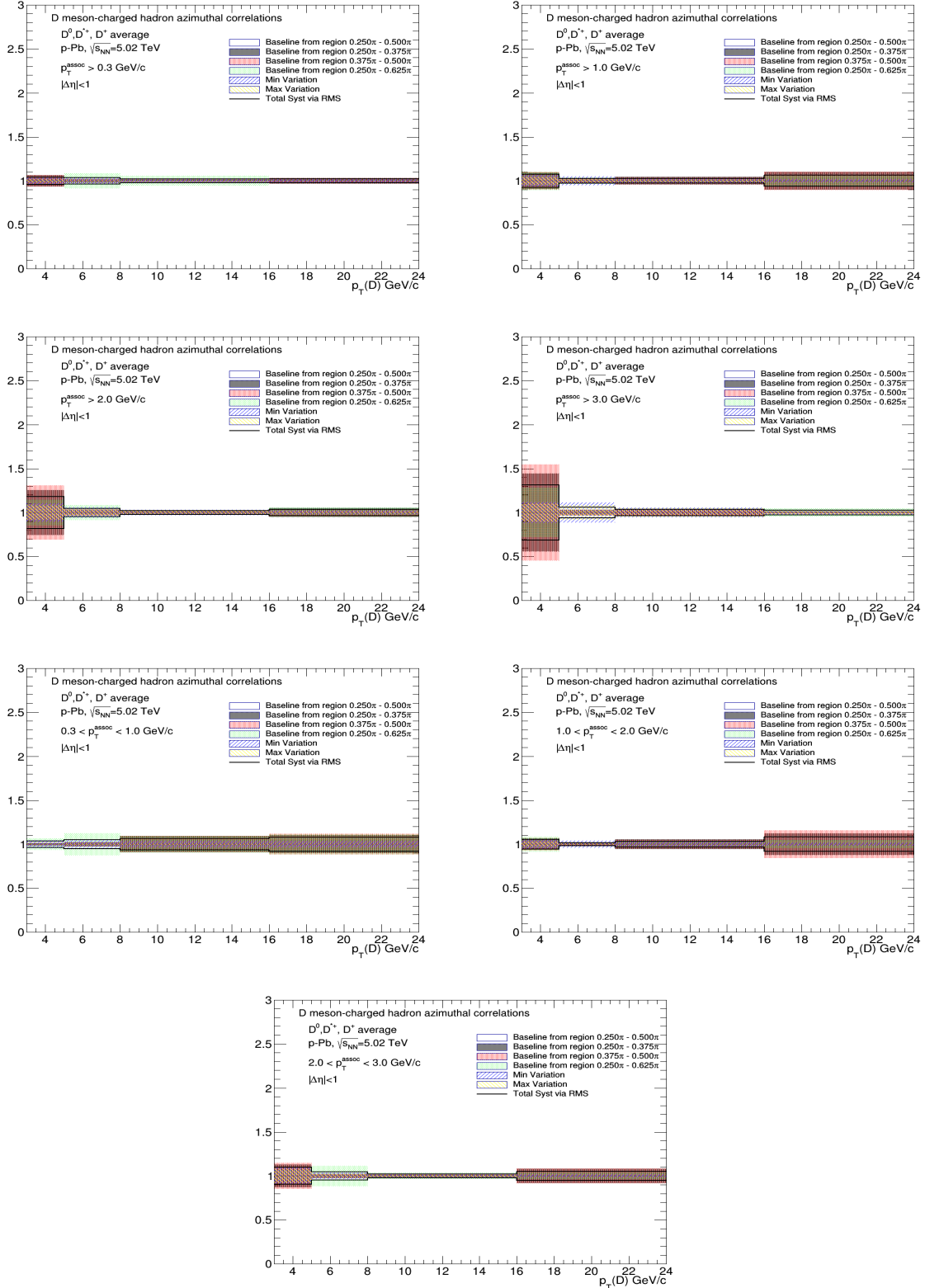
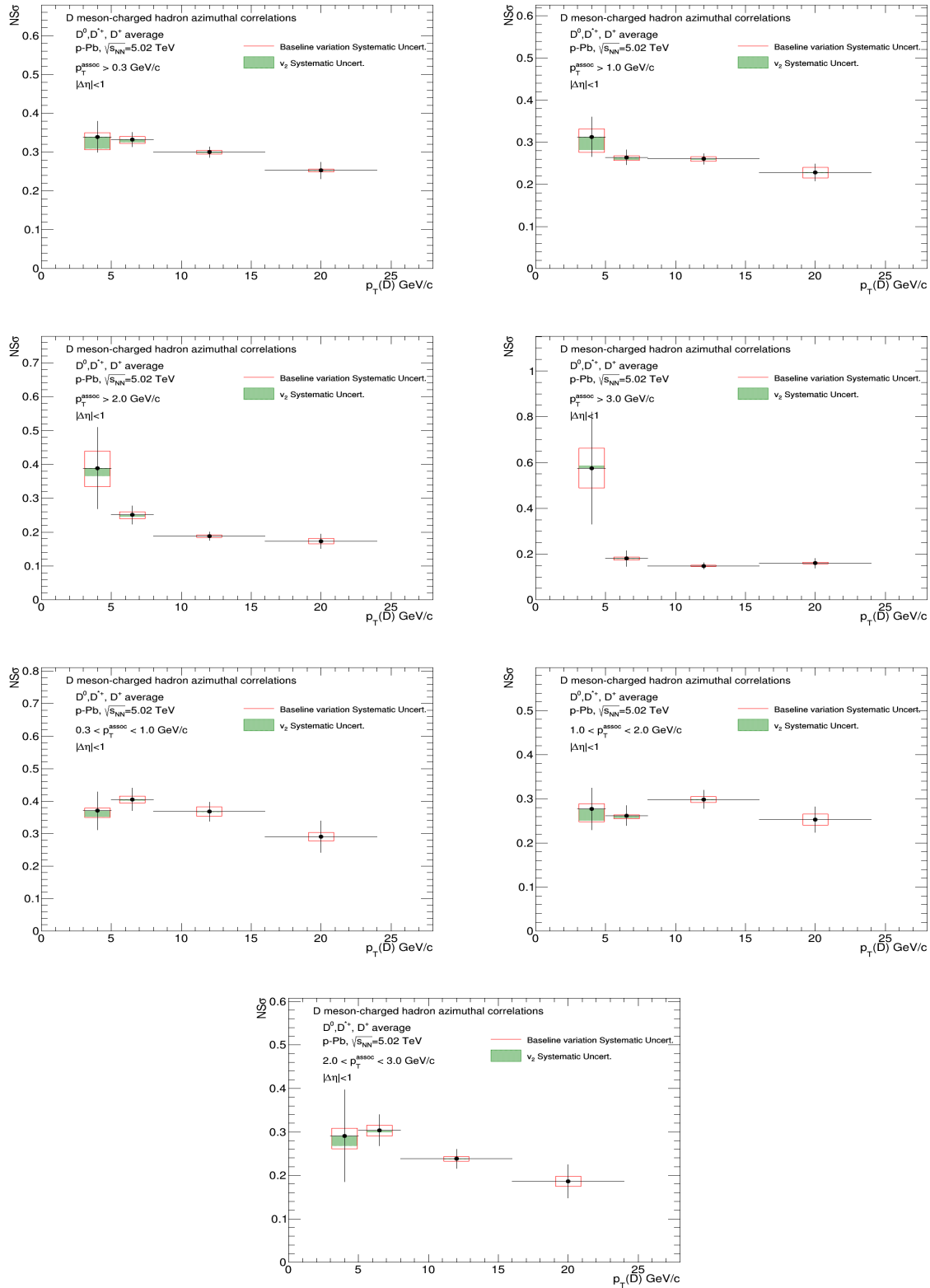


Figure 48: Top panels: near side yield $p_T(D)$ trend for the D-meson average, extracted from fit to the azimuthal correlation distributions, for all the analyzed kinematic ranges of associated track p_T . Bottom panels: for each kinematic region the systematic uncertainties coming from the variation of the fit procedure are shown.



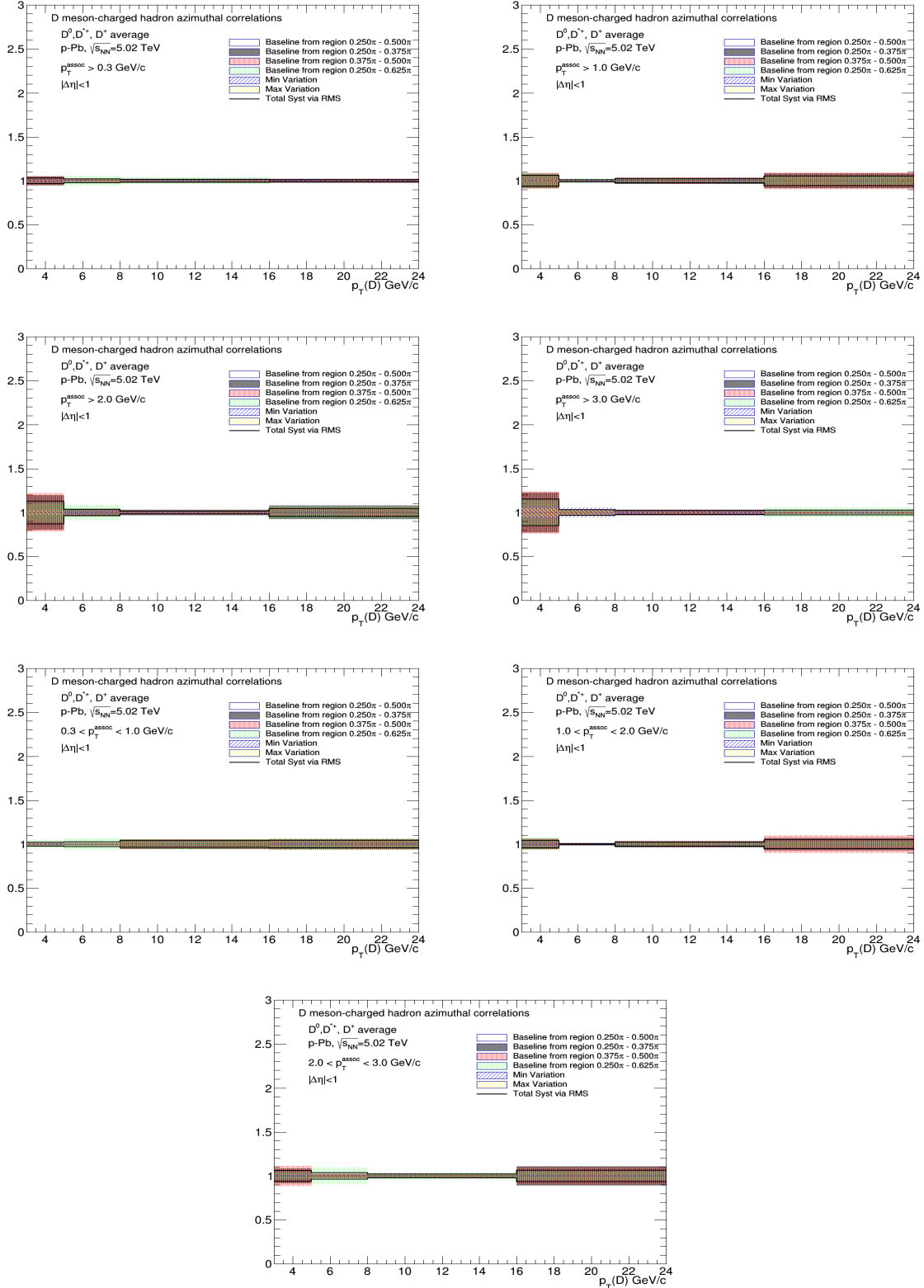
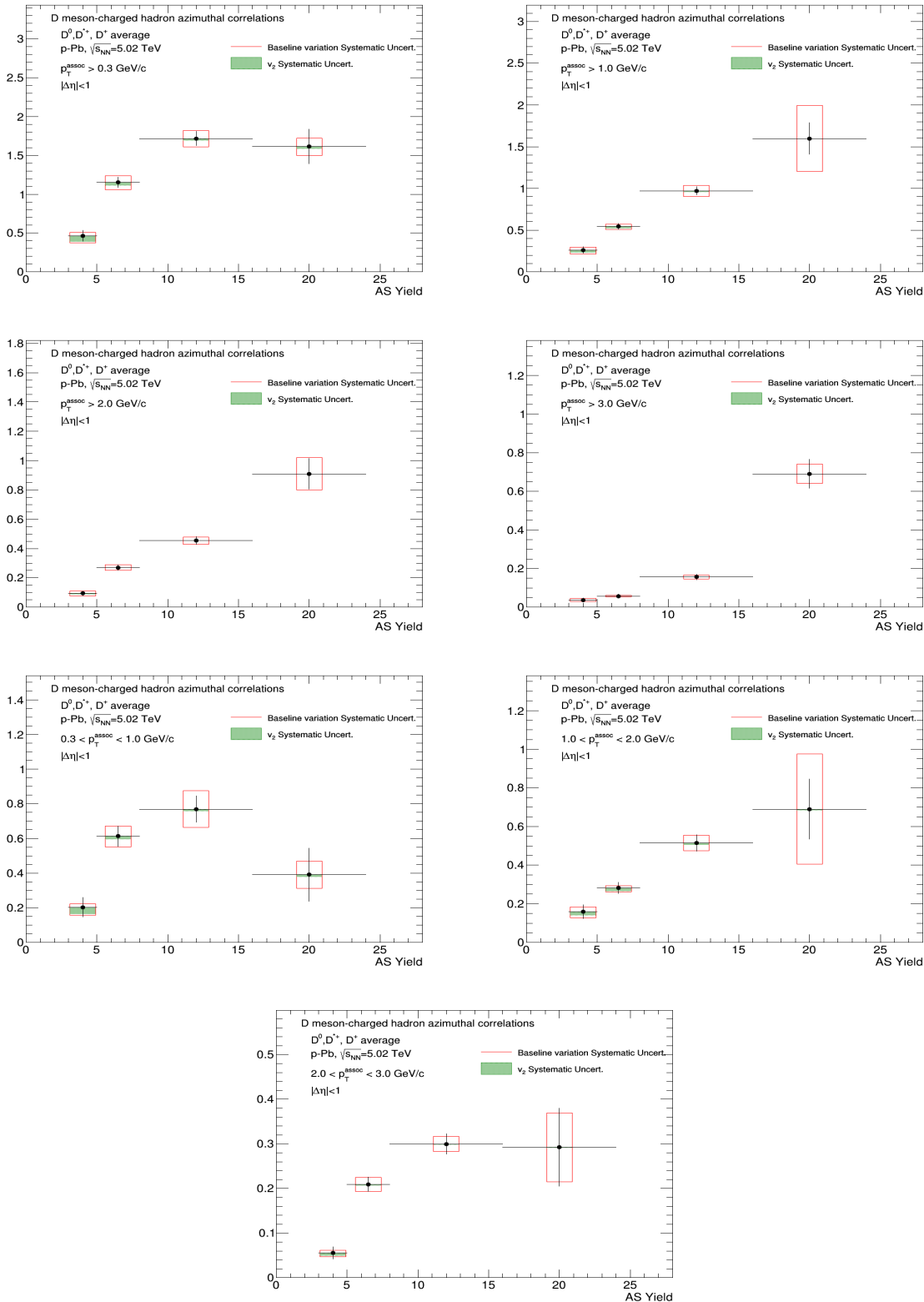


Figure 49: Top panels: near side width $p_T(D)$ trend for the D-meson average, extracted from fit to the azimuthal correlation distributions, for all the analyzed kinematic ranges of associated track p_T . Bottom panels: for each kinematic region the systematic uncertainties coming from the variation of the fit procedure are shown.



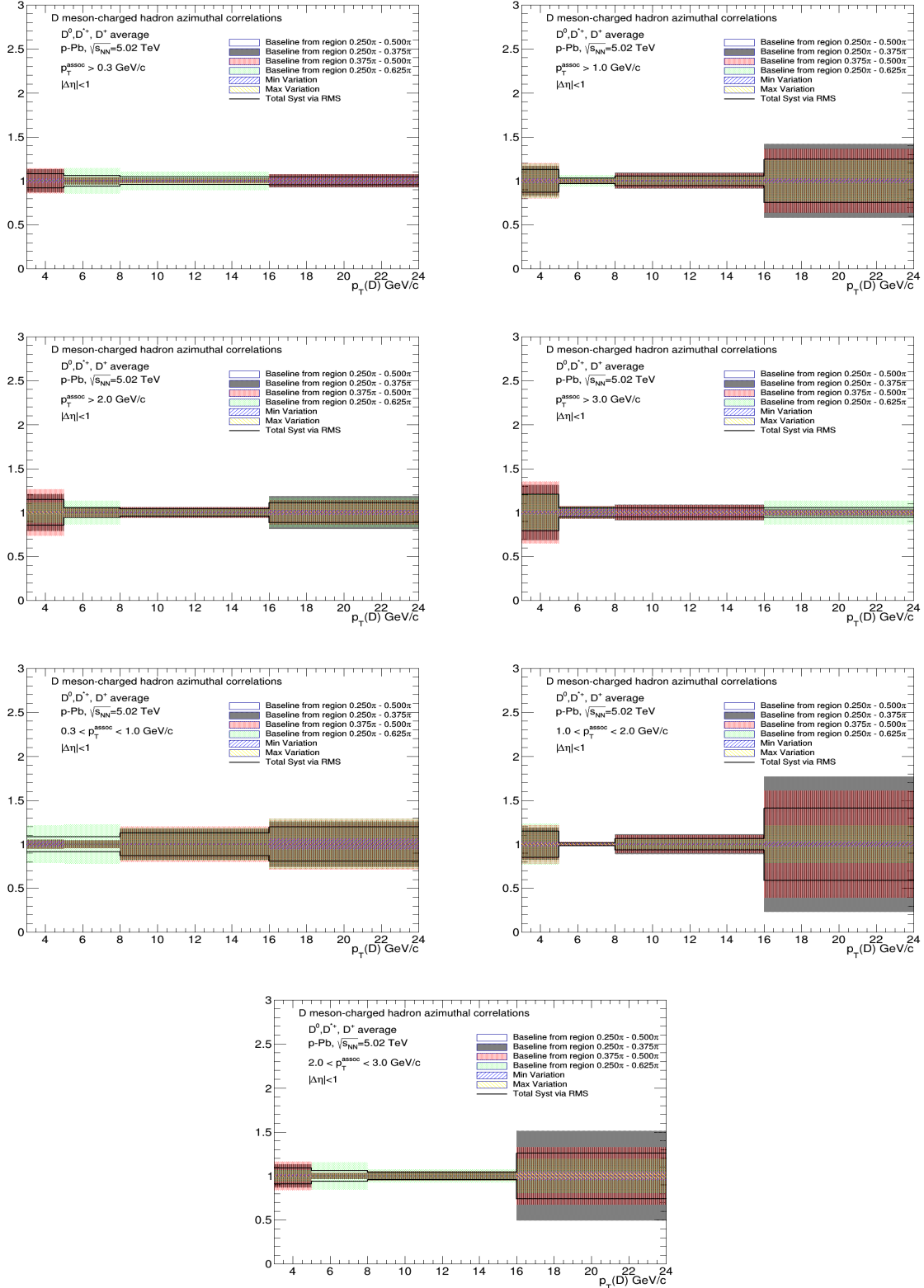
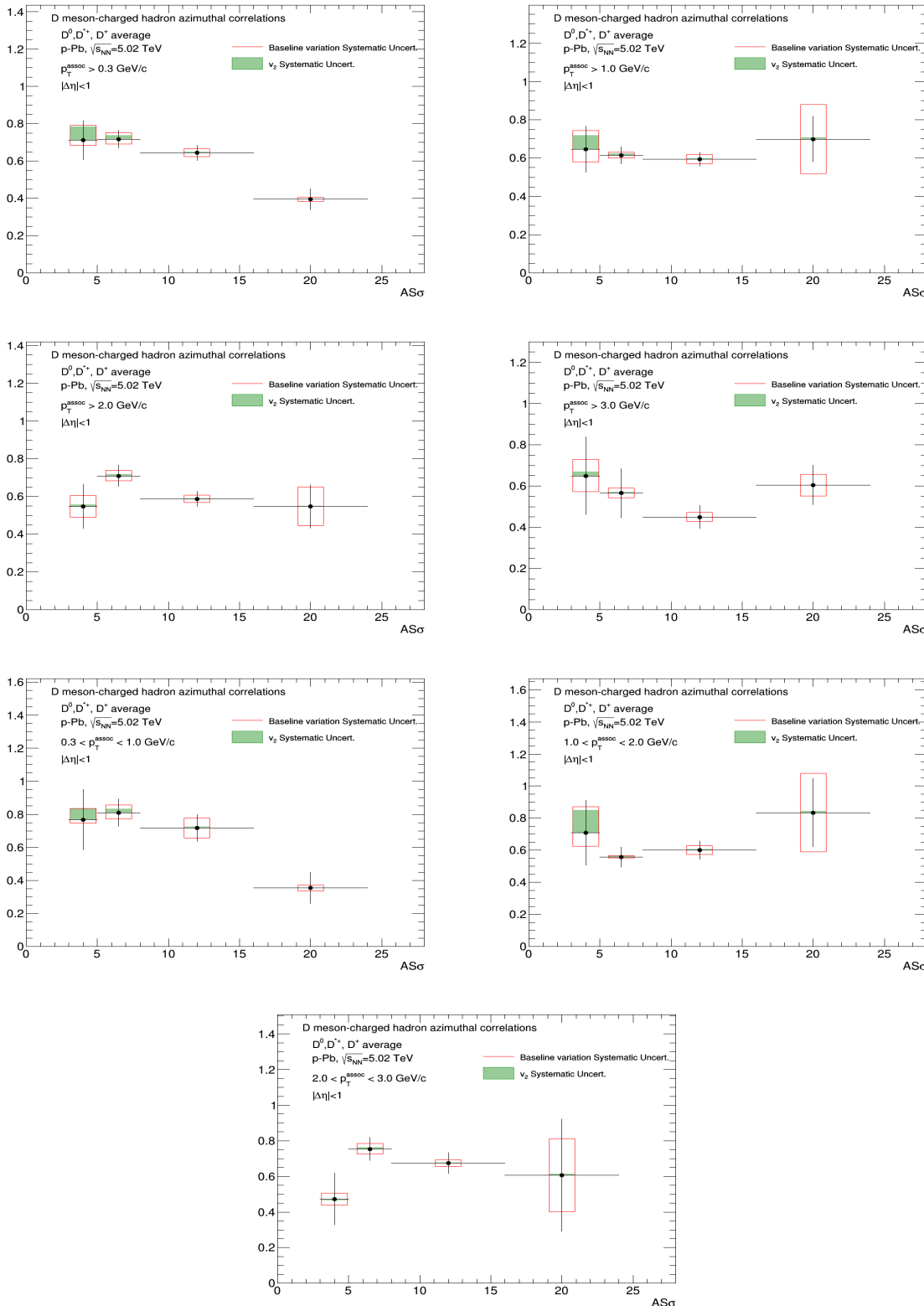


Figure 50: Top panels: away side yield $p_T(D)$ trend for the D-meson average, extracted from fit to the azimuthal correlation distributions, for all the analyzed kinematic ranges of associated track p_T . Bottom panels: for each kinematic region the systematic uncertainties coming from the variation of the fit procedure are shown.



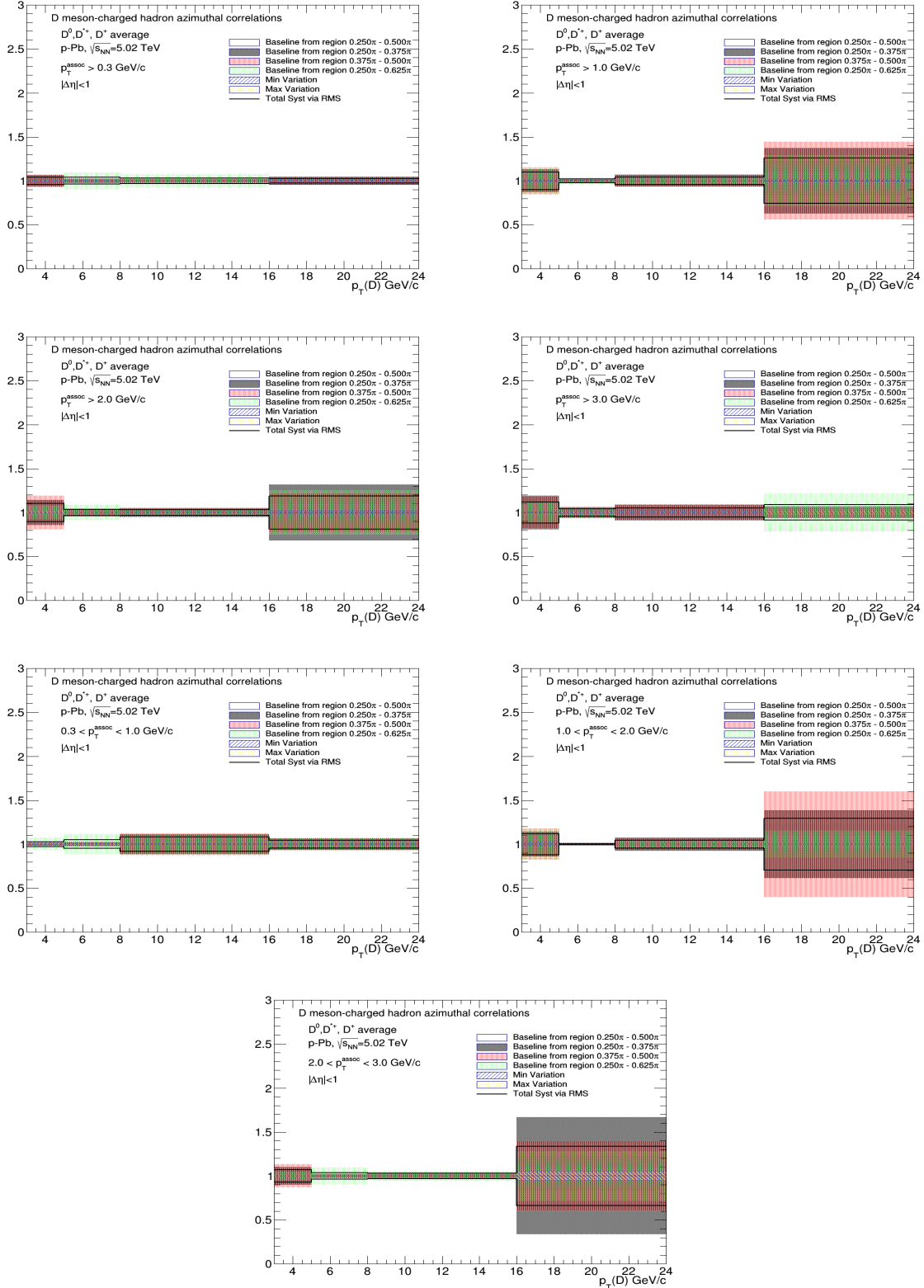
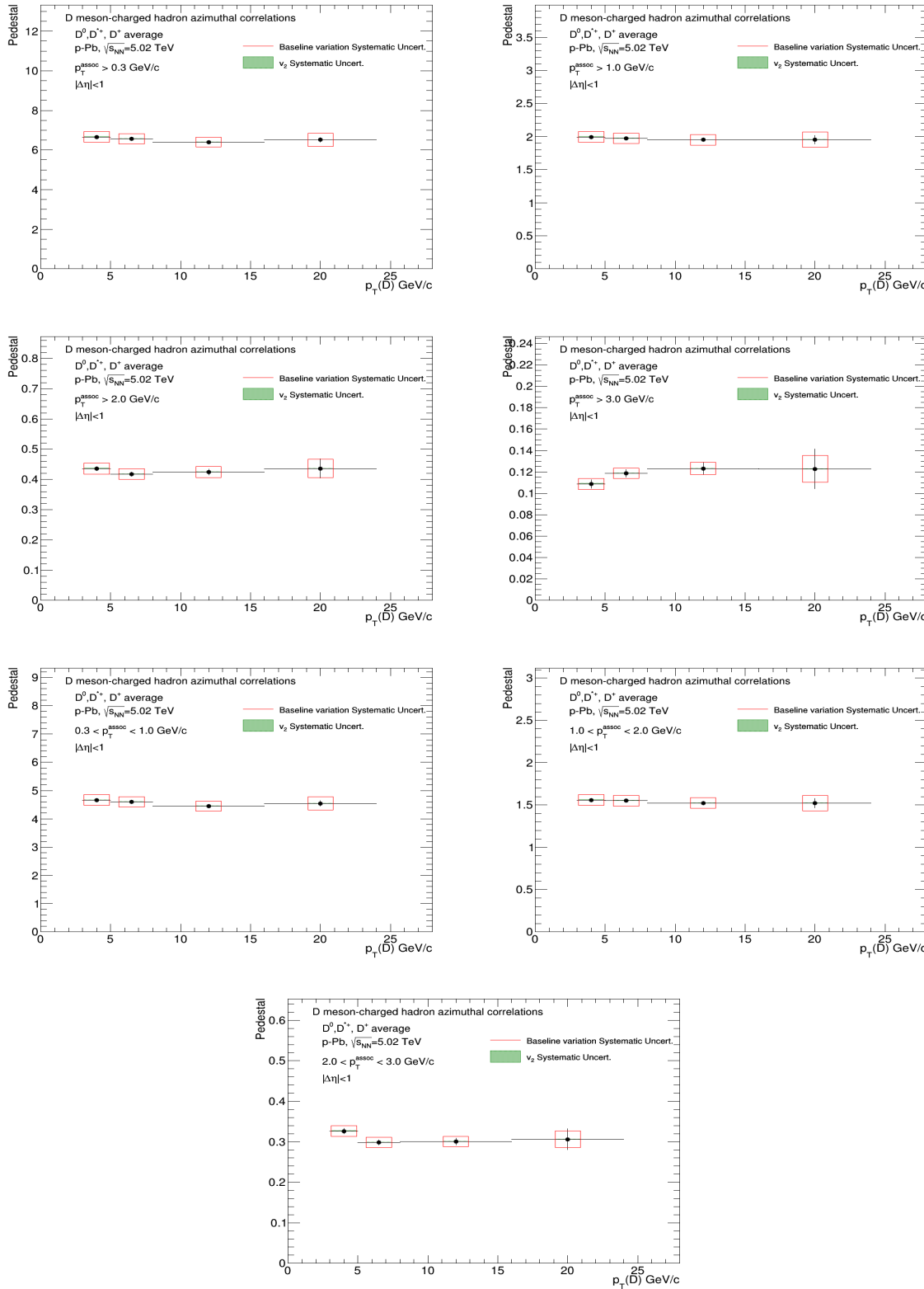


Figure 51: Top panels: away side width $p_T(D)$ trend for the D-meson average, extracted from fit to the azimuthal correlation distributions, for all the analyzed kinematic ranges of associated track p_T . Bottom panels: for each kinematic region the systematic uncertainties coming from the variation of the fit procedure are shown.



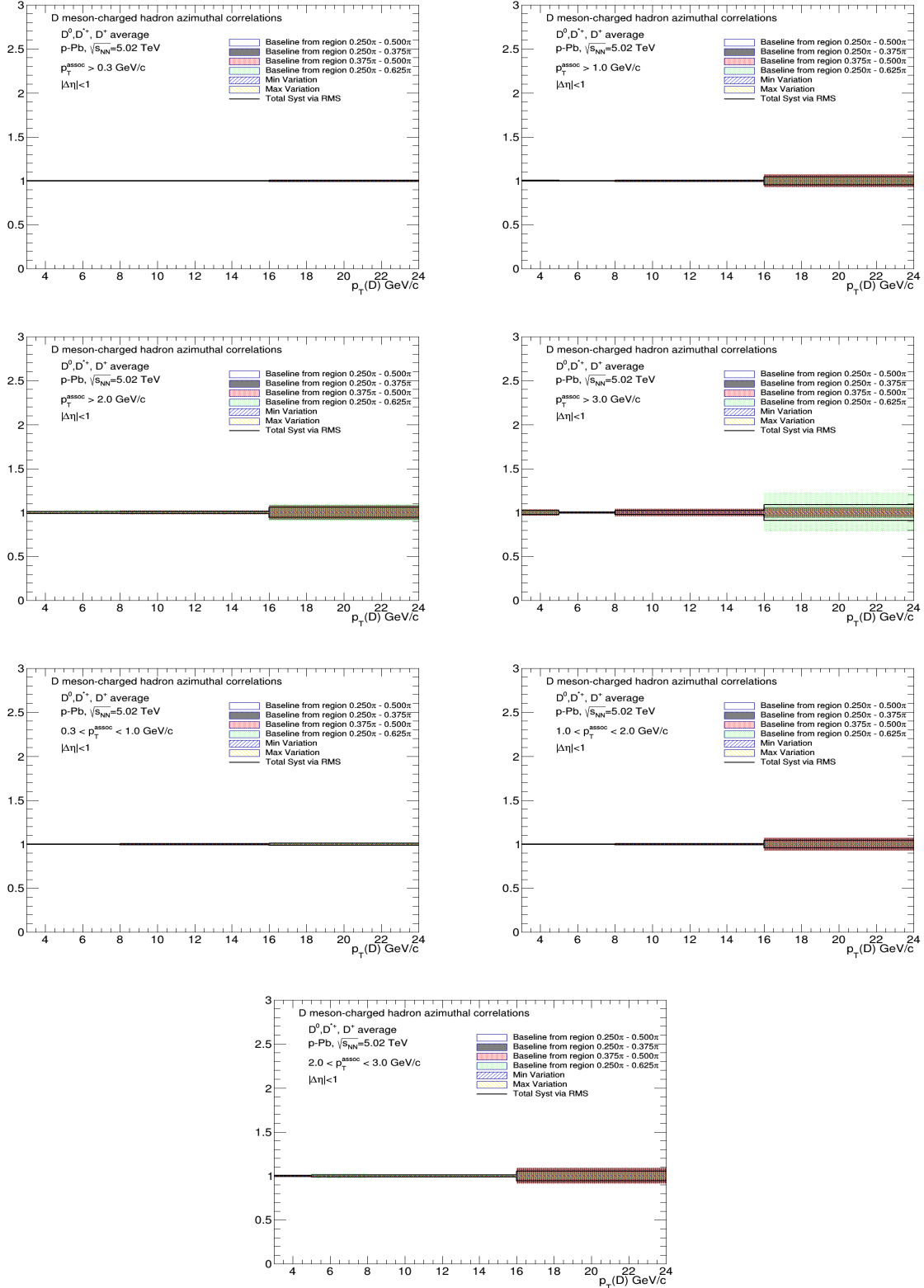


Figure 52: Top panels: baseline height trend for the D-meson average, extracted from fit to the azimuthal correlation distributions, for all the analyzed kinematic ranges of associated track p_T . Bottom panels: for each kinematic region the systematic uncertainties coming from the variation of the fit procedure are shown.

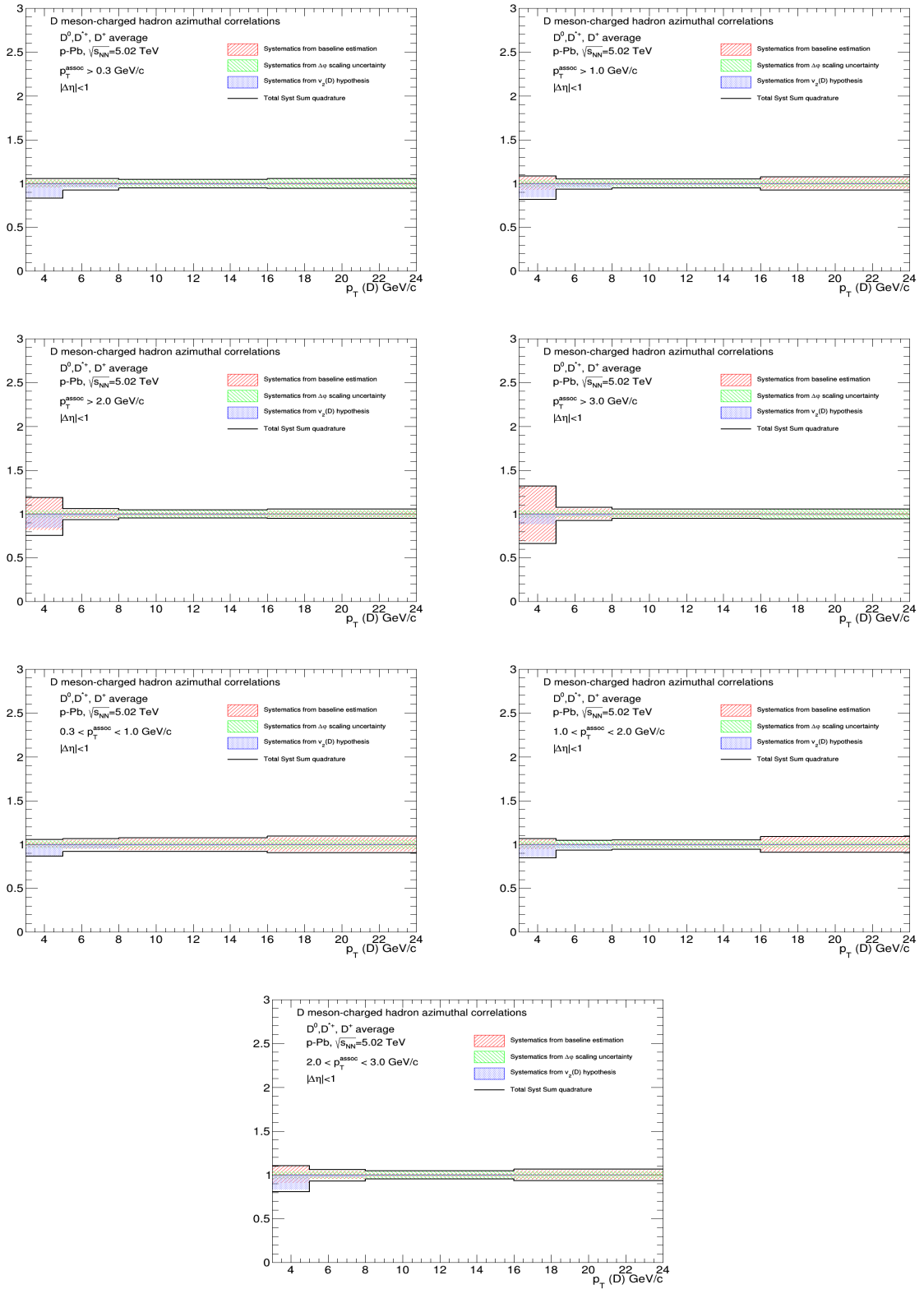


Figure 53: Total systematic uncertainty, and its components, for near-side yields in the different kinematic ranges analyzed

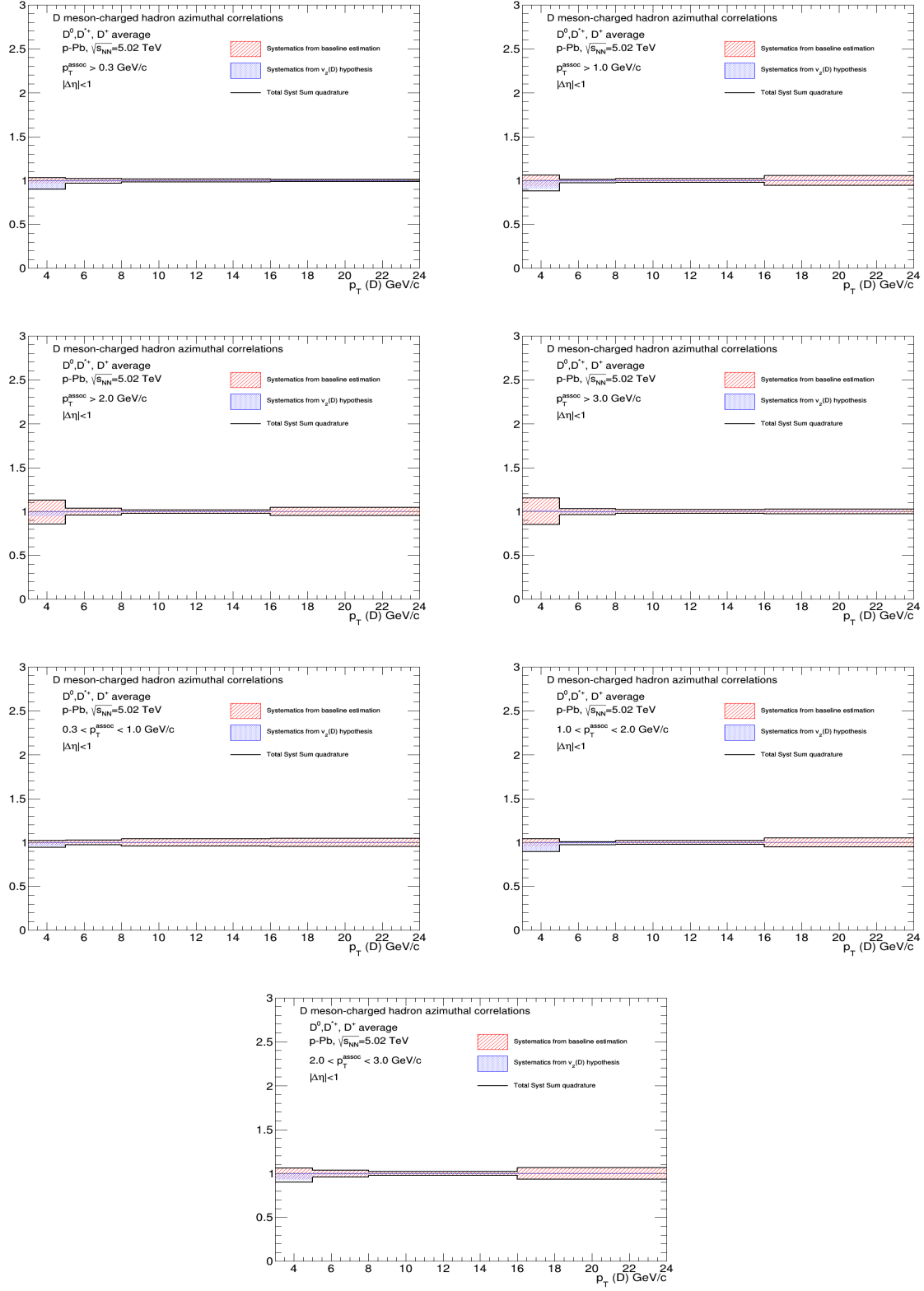


Figure 54: Total systematic uncertainty, and its components, for near-side sigma in the different kinematic ranges analyzed

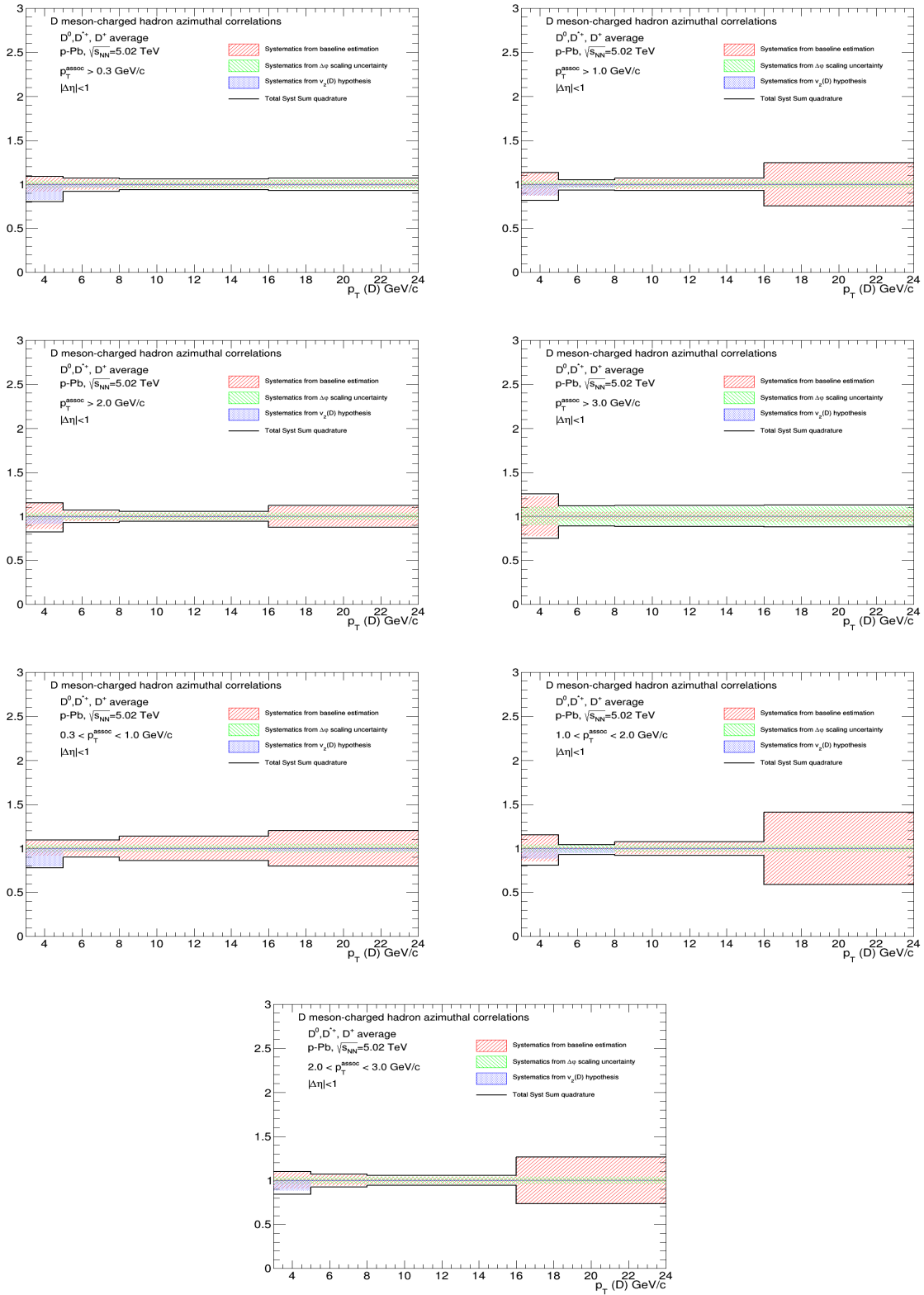


Figure 55: Total systematic uncertainty, and its components, for away-side yields in the different kinematic ranges analyzed

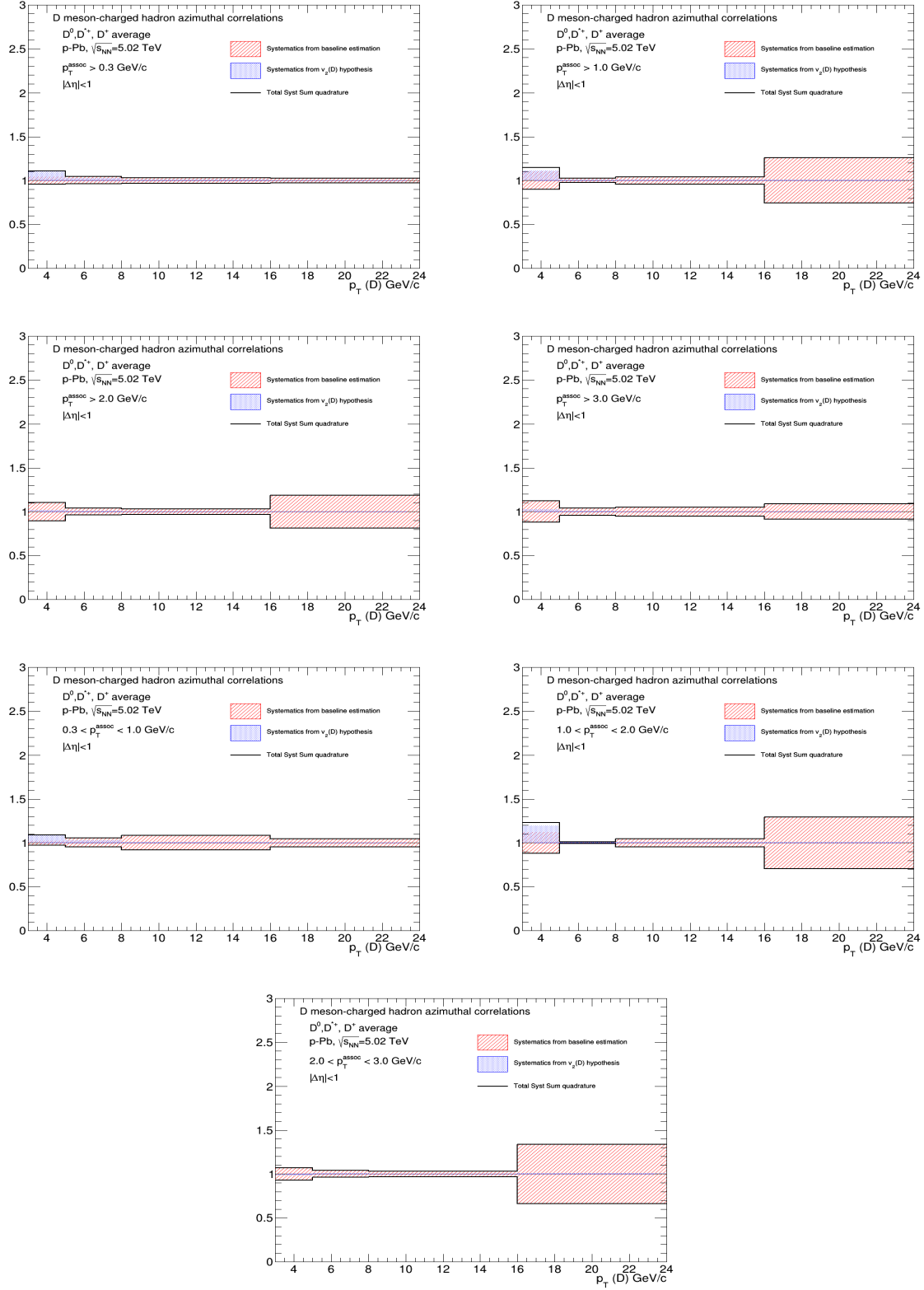


Figure 56: Total systematic uncertainty, and its components, for away-side sigma in the different kinematic ranges analyzed

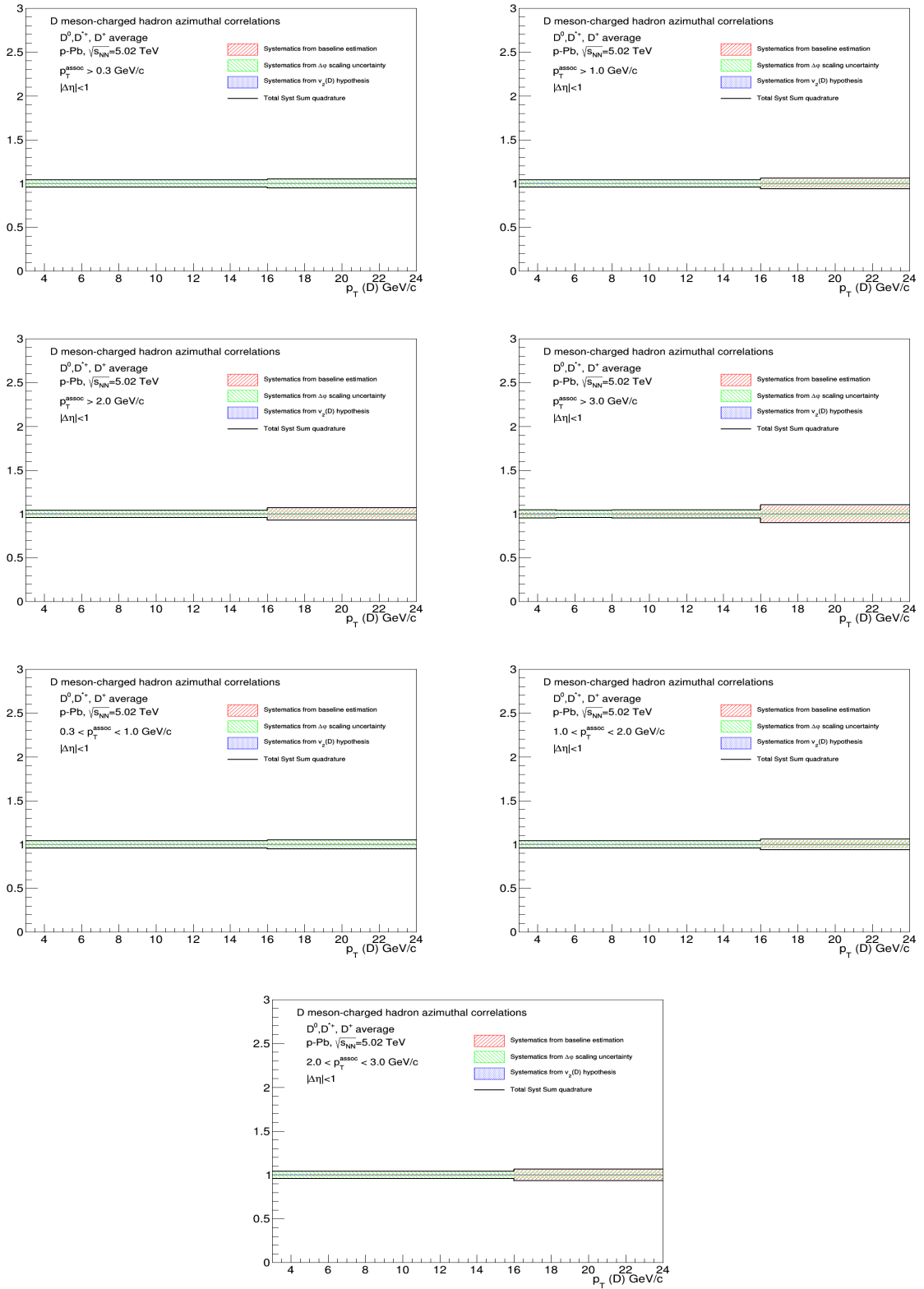


Figure 57: Total systematic uncertainty, and its components, for baseline heights in the different kinematic ranges analyzed.

711 5.4 Comparison of 2016 p-Pb and 2013 p-Pb results

712 In Figure 58, the average correlation distributions from the published analysis in p-Pb 2013 sample
 713 (black points) and the new p-Pb 2016 sample (red points), both at 5 TeV, are compared. As it's evident,
 714 the statistical and systematic uncertainties are largely reduced in the new data sample. The feature of
 715 the correlation distributions are the same in both systems, and an overall compatibility of the points is
 716 observed. Only in the near-side region, the 2016 data points have a tendency of being slightly below the
 717 2013 data points. In part, this can be partially explained with the different procedure for assessing the
 718 B to D decay topology bias (2016 data corrected, with a slight downward shift for the first two points,
 719 while for 2013 data only a downward systematic uncertainty was applied.

720 Figure 59 shows the same comparison for the fit observables. Also in this case the uncertainties are
 721 largely reduced for the 2016 analysis. While the away side features are compatible (but with large
 722 uncertainties) and the near-side widths are on top of each other, for the near-side yields a slight decrease
 723 of the 2016 results is observed (though well within the uncertainty). This is a direct consequence of
 724 the feature just observed in the comparison of the near-side peak point of the azimuthal correlation
 725 distributions (i.e. that the 2016 data points are slightly lower than the 2013 ones).

726 5.5 Comparison of 2016 p-Pb and 2010 pp results

727 Figure 60 shows the comparison of the average D-h correlation distributions in pp 2010 data sample at
 728 $\sqrt{s} = 7$ TeV (published in [2]) and in the new p-Pb 2016 sample at $\sqrt{s_{\text{NN}}} = 5.02$ TeV. The results are
 729 shown after the subtraction of the baseline. The precision of the new p-Pb results is much better than that
 730 of pp results; the correlation distributions show very similar features in the two collision systems.

731 In Figure 61 the comparison is performed for the near-side peak observables, again in the common
 732 kinematic ranges, where the same consideration about the uncertainties holds. The similarity of the
 733 correlation distributions is reflected also in the near-side yield and width values, which do not seem to
 734 differ within the uncertainties, pointing to the absence of strong effects from cold-nuclear matter effects
 735 on the correlation distributions.

736 It has to be said that, on the base of a study performed with Pythia6-Perugia2011 simulations, a scaling
 737 factor of about 0.93 is expected when passing from a center-of-mass energy of $\sqrt{s} = 7$ TeV to $\sqrt{s} = 5$
 738 TeV, difficult to be appreciated with the current uncertainties, especially the pp ones.

739 5.6 Comparison of 2016 p-Pb and model expectations

740 A comparison of the average D-h correlation distributions on the new p-Pb data samples with expec-
 741 tations from Monte Carlo simulations (currently Pythia6-Perugia2011, Pythia6-Perugia2010, Pythia6-
 742 Perugia0, PYTHIA8; POWHEG+PYTHIA and EPOS 3 will be added if they come in time) is shown in
 743 Figure 62, after the baseline subtraction (which differs strongly between data and simulations, due to he
 744 very different underlying event). The simulations, though being for pp, include the boost of the center-
 745 of-mass along the beam axis present in p-Pb collisions and nuclear PDF. The shape of the correlation
 746 distributions is well reproduced by all the models, together with their p_T trend and with the evolution of
 747 the correlation peaks.

748 Figures 63 and 64 show the same comparison for the fit observables (peak yields and widths for near-side
 749 and away-side, respectively), for all the addressed p_T ranges.

750 5.7 Planned results for SQM approvals

751 We are planning to approve the following results, all shown in the previous figures (the final graphical
 752 style of the plots is still to be finalized):

- 753 – Average D-h correlation distributions, in exemplary p_T range

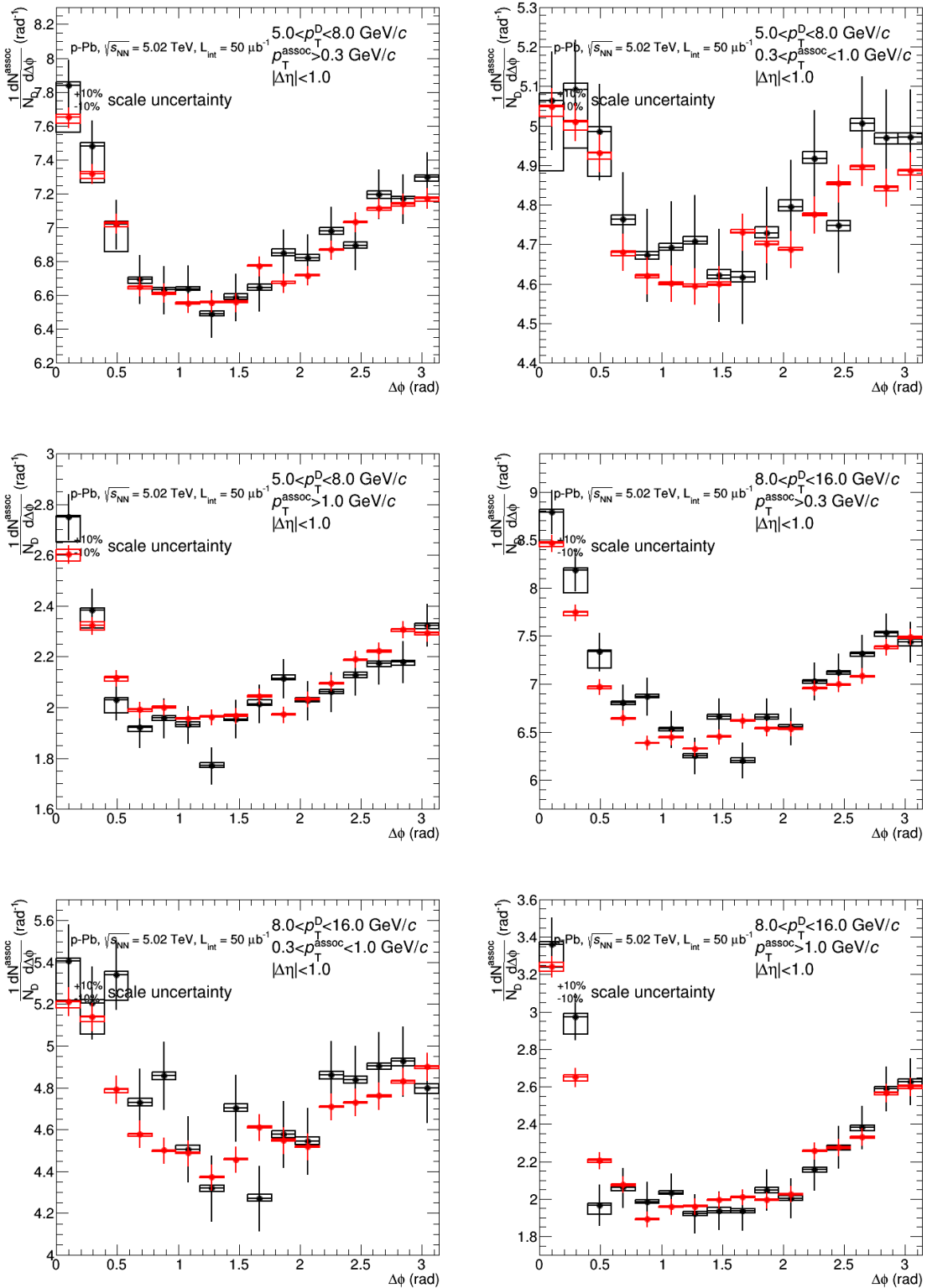


Figure 58: Comparison of 2016 (red) and 2013 (black) results for azimuthal correlation distributions, for the common p_T ranges.

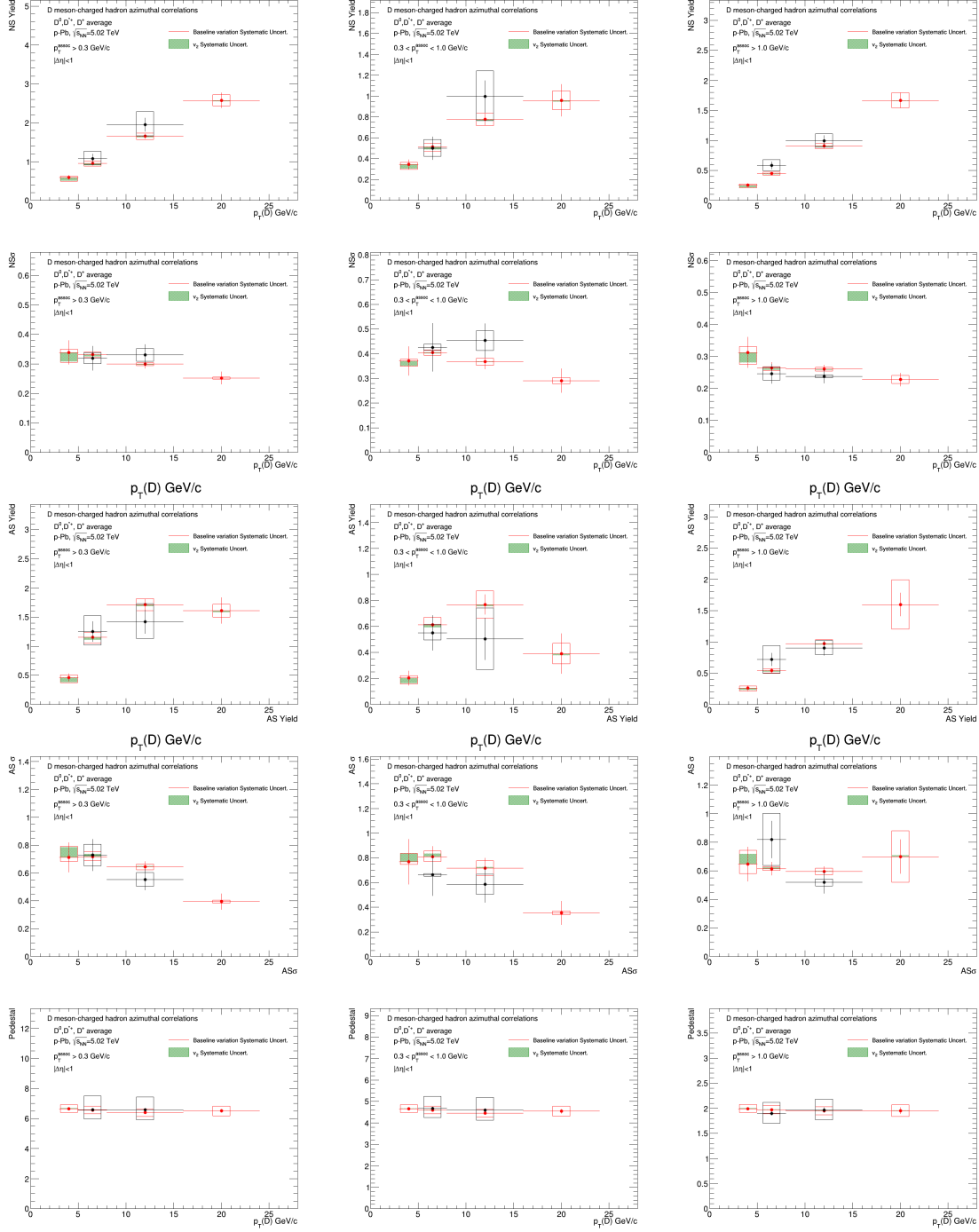


Figure 59: Comparison of the average D-h azimuthal correlation properties between 2016 p-Pb (red) and 2013 p-Pb (black) data analysis, for the common p_T ranges of D meson and associated particles.

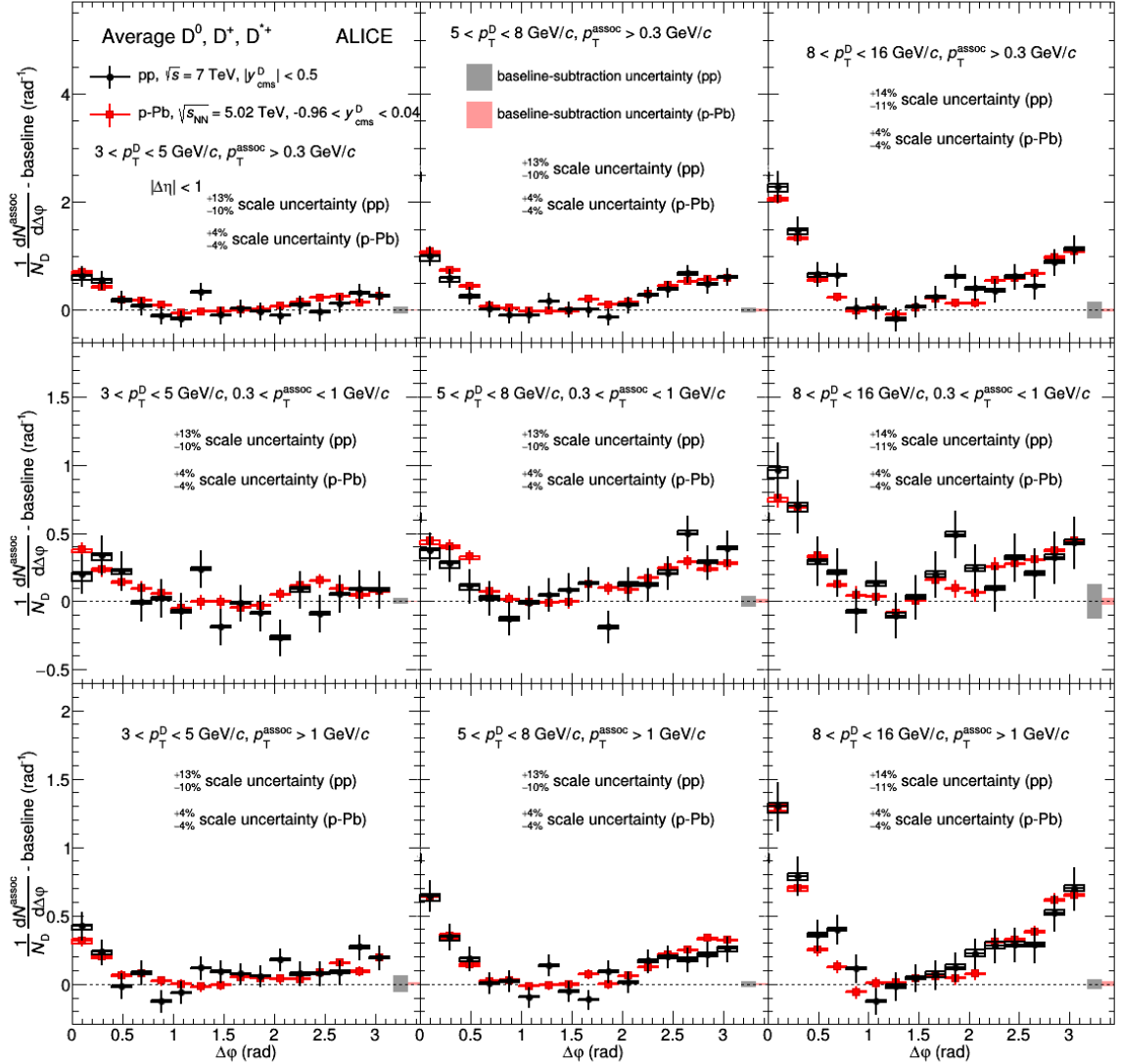


Figure 60: Comparison of pp 2010 (black) and p-Pb 2016 (red) average D-h azimuthal correlation distributions, for the common p_T ranges.

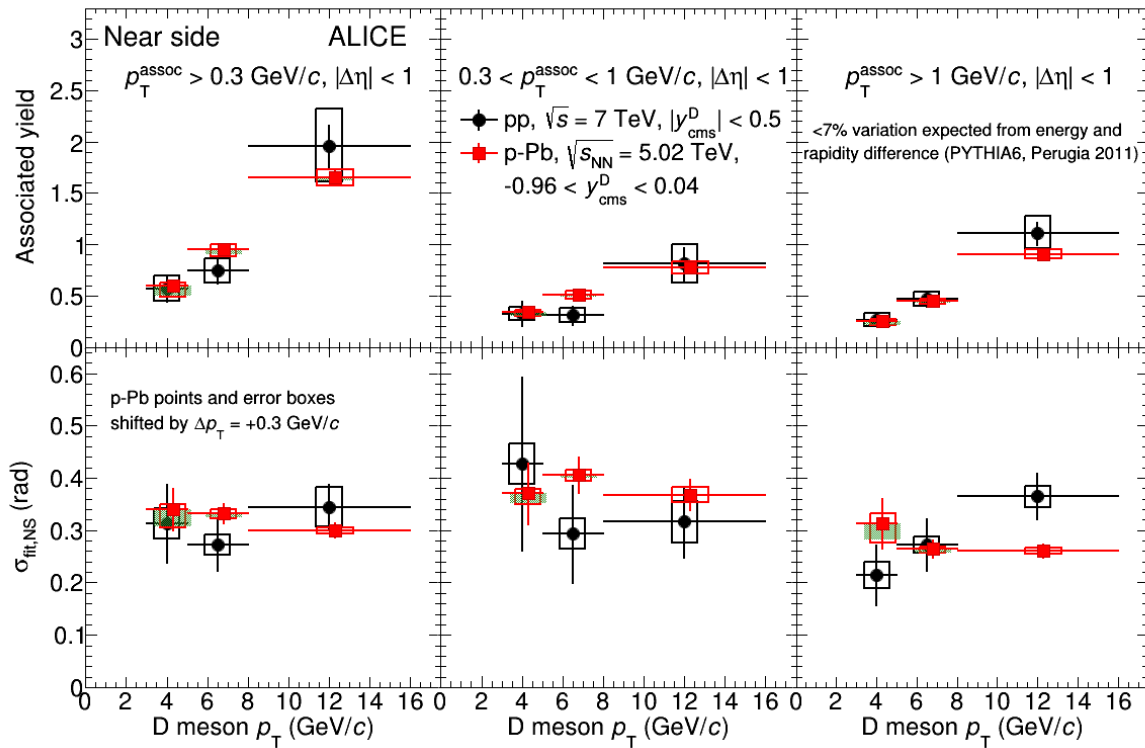
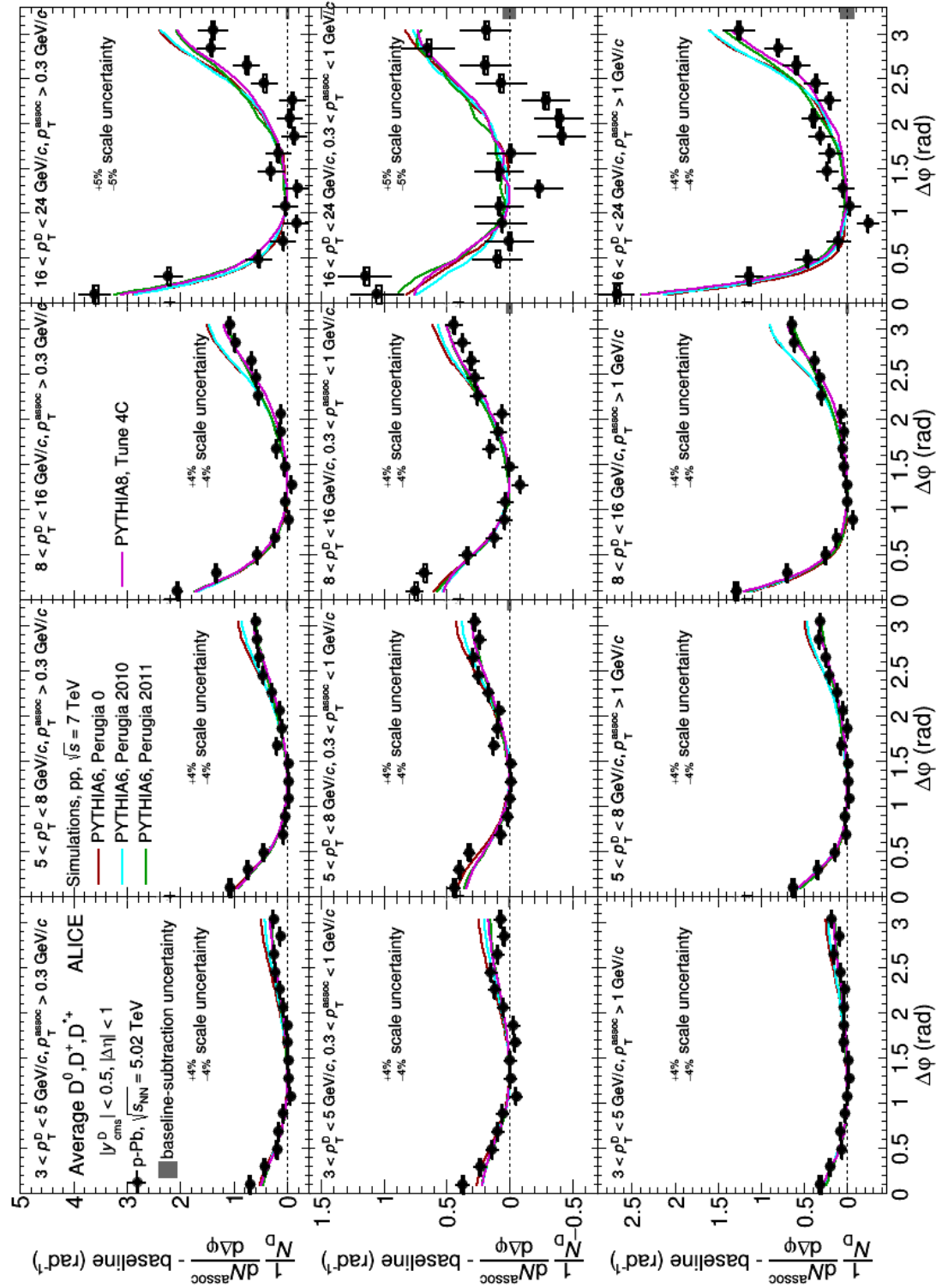


Figure 61: Comparison of pp 2010 (black) and p-Pb 2016 (red) near-side peak yields and widths, for the common p_T ranges.

- 754 – Fit of D-h correlation distributions, in exemplary p_T range
- 755 – $p_T(D)$, $p_T(\text{assoc})$ trend of NS yield, NS width, AS yield, AS sigma
- 756 – Comparison of correlation distributions with expectations from models (PYTHIA6, PYTHIA8, if
757 in time POWHEG, EPOS)
- 758 – Comparison of fit observables with expectations from models (PYTHIA6, PYTHIA8, if in time
759 POWHEG, EPOS)
- 760 – Comparison of correlation distributions with pp 2010 results
- 761 – Comparison of fit observables with pp 2010 results



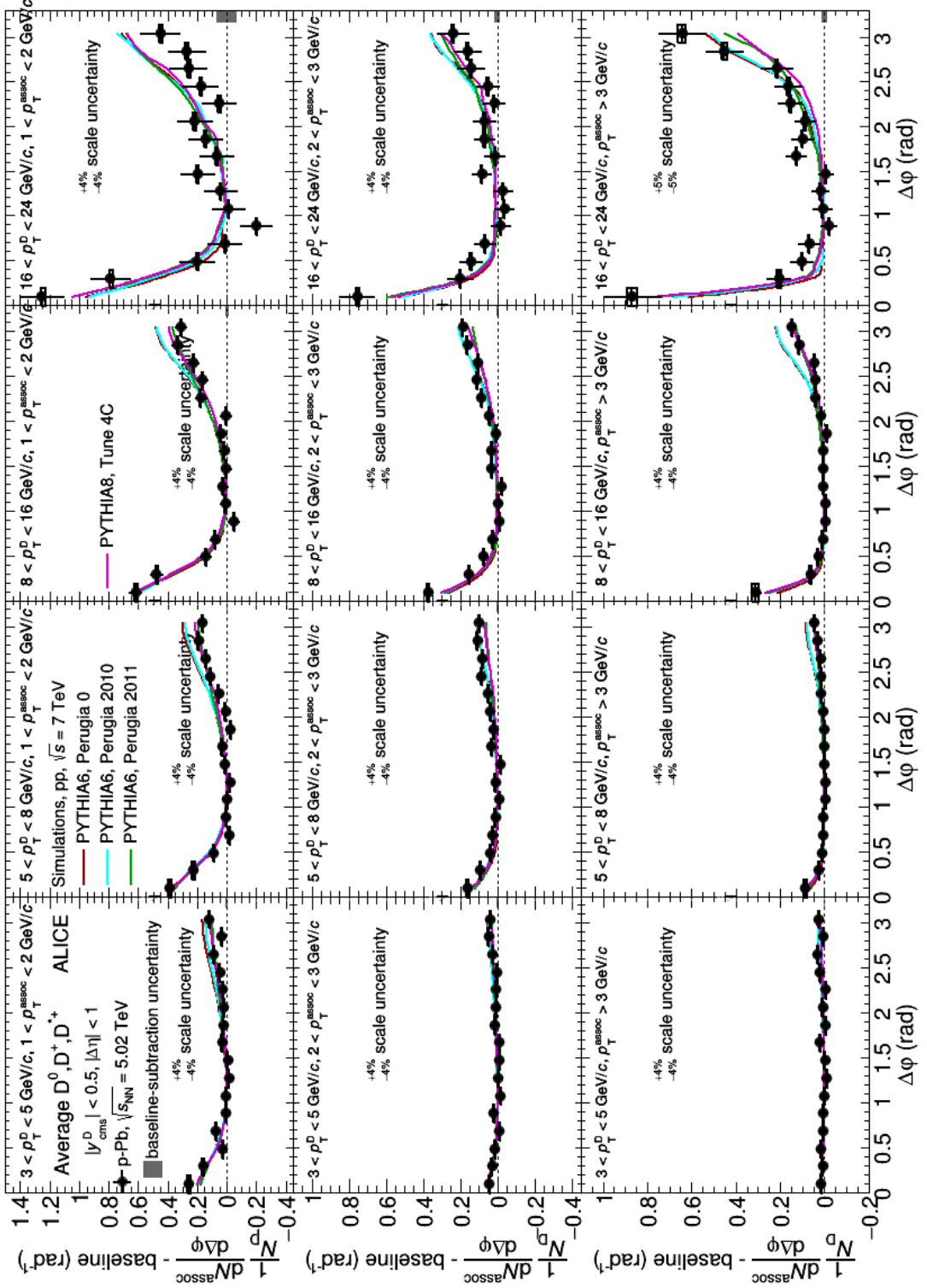
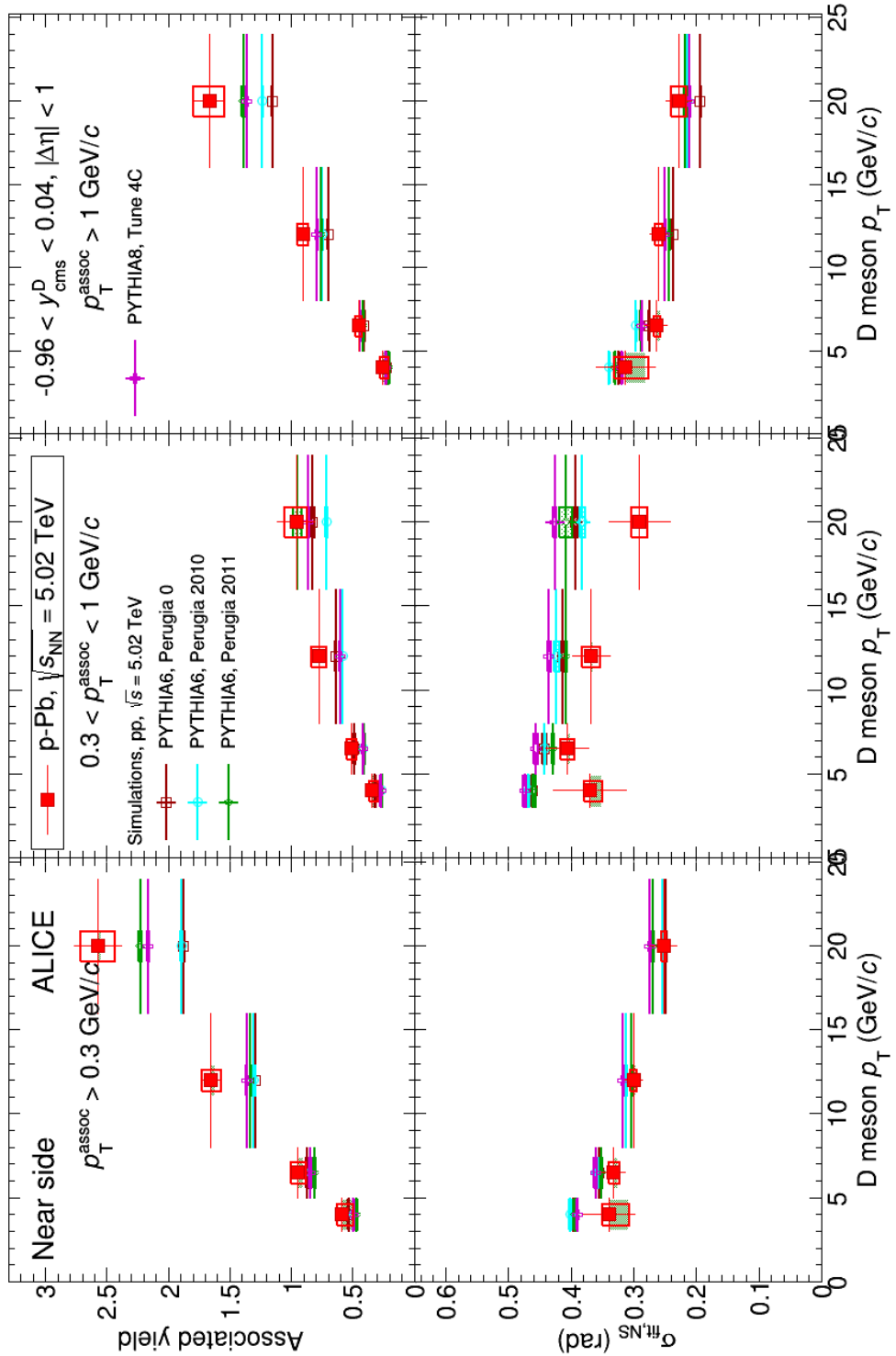


Figure 62: Comparison of p-Pb 2016 average D-h correlation distributions and model expectations, for all the studied kinematic ranges.



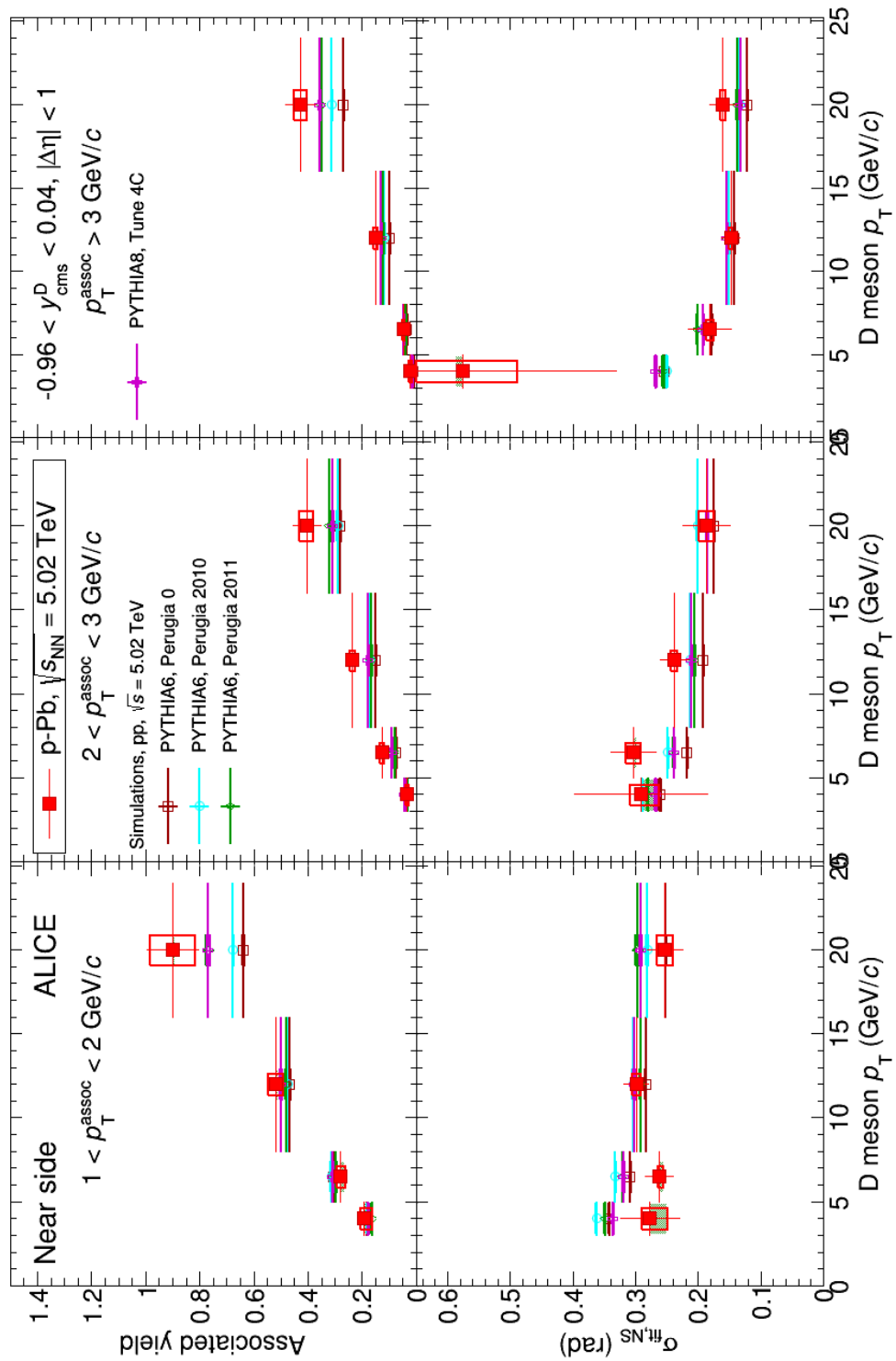
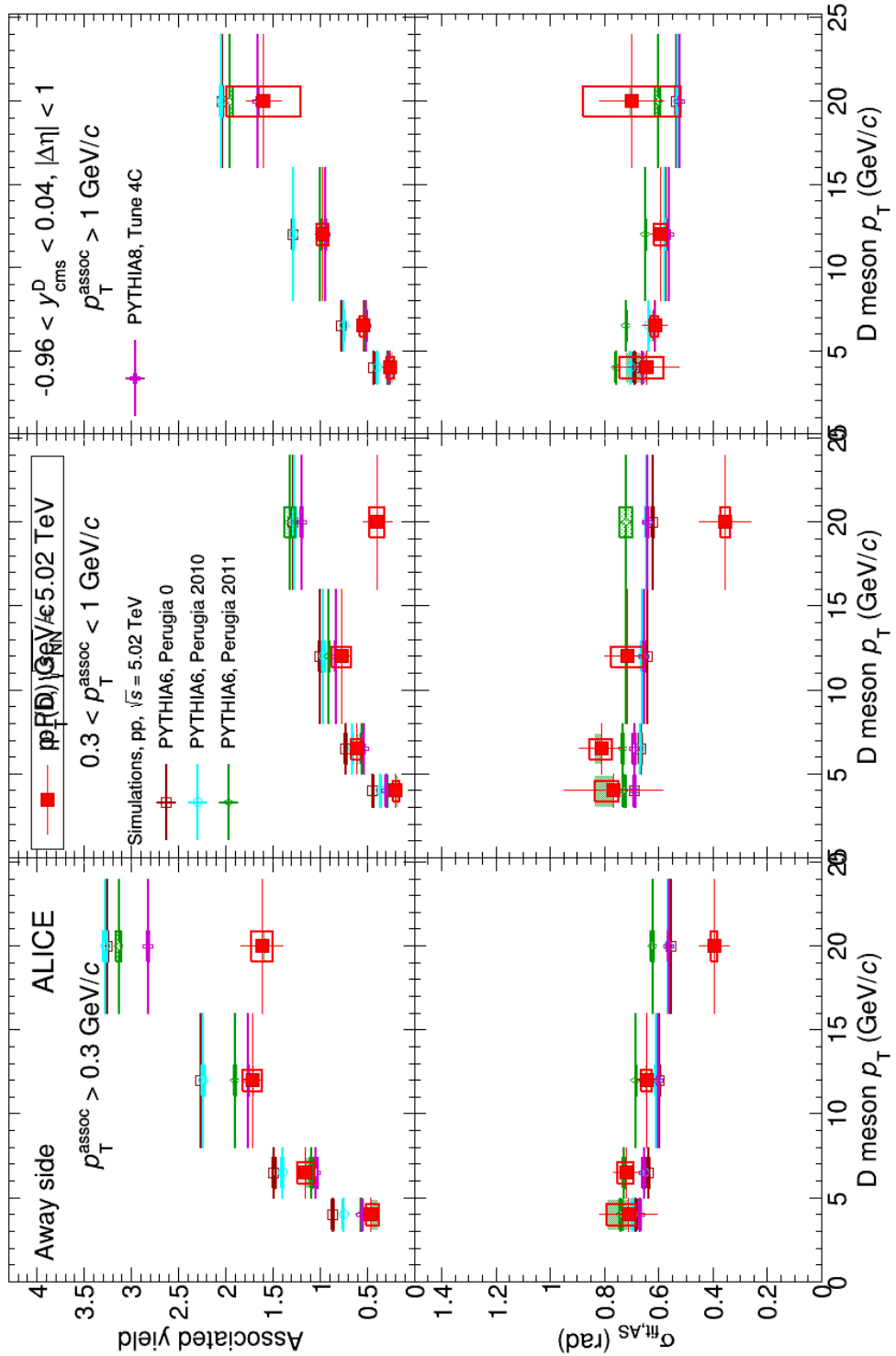
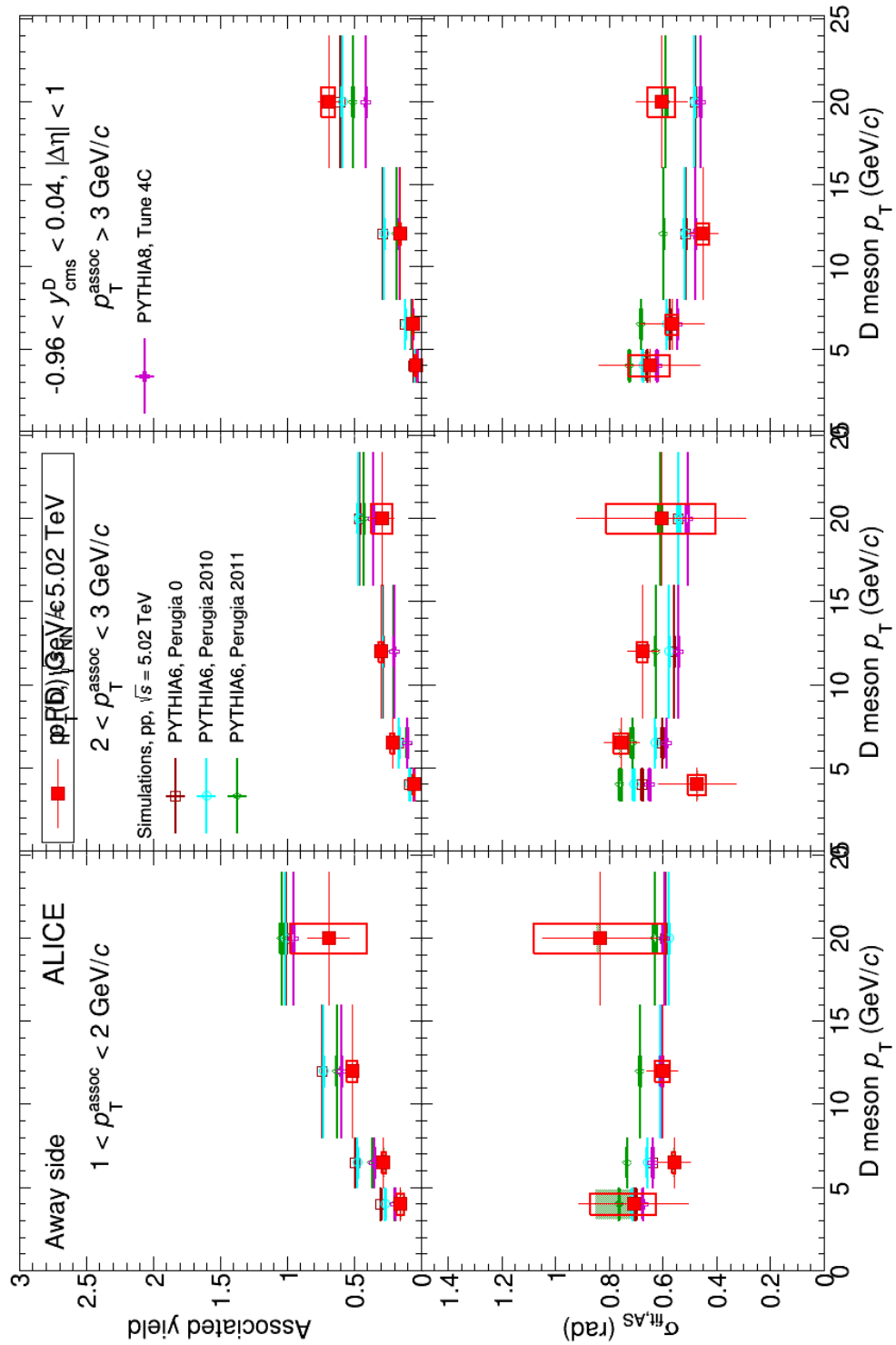


Figure 63: Comparison of near-side peak yields and widths from p-Pb 2016 results and model expectations, for all the studied kinematic ranges.





762 **6 Bibliography**

763 **References**

- 764 [1] B. Abelev et al. [ALICE Collaboration], JHEP **01** (2012) 128
765 [2] B. Abelev et al. [ALICE Collaboration], Eur. Phys. J. C (2017) 77:245
766 [3] B. Abelev et al. [ALICE Collaboration], Phys.Lett. B719 (2013) 29-41
767 [4] B. Abelev et al. [ALICE Collaboration], Phys.Lett. B726 (2013) 164-177
768 [5] <https://aliceinfo.cern.ch/Notes/node/300>
769 [6] <https://aliceinfo.cern.ch/Notes/node/238>
770 [7] <https://aliceinfo.cern.ch/Notes/node/201>